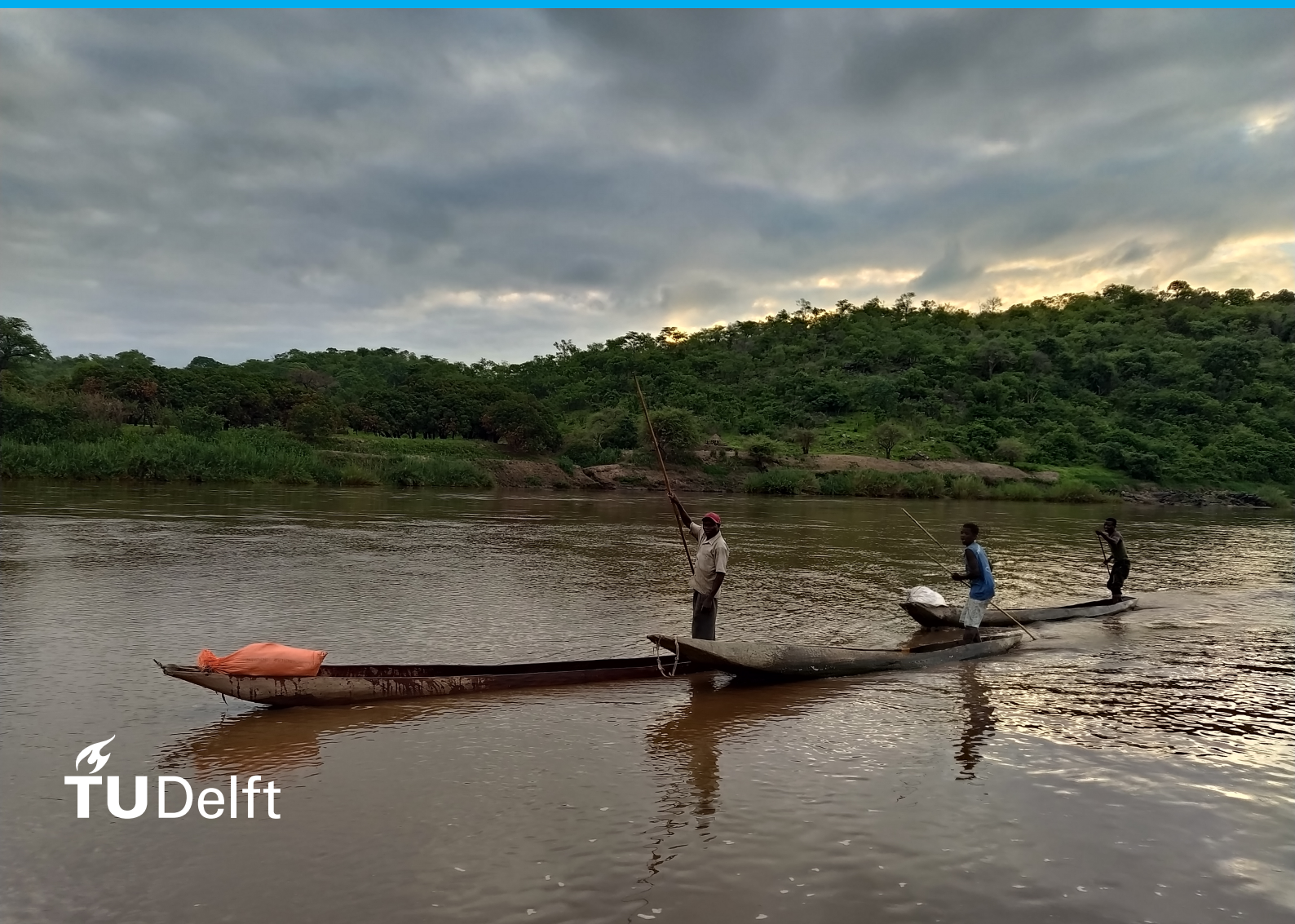


River discharge modelling based on surface flow velocity estimations

A combination of Large-Scale Particle Image Velocimetry and three dimensional discharge modelling

S. Schurer



River discharge modelling based on surface flow velocity estimations

A combination of Large-Scale Particle Image Velocimetry and three dimensional discharge modelling

by

S. Schurer

to obtain the degree of Master of Science
at the Delft University of Technology,
to be defended publicly on Friday August 14, 2020

Student number: 4759613
Project duration: September 1, 2019 – Augustus 14, 2020
Thesis committee: Dr. ir. H.C. Winsemius, TU Delft
Ir. W.M.J. Luxemburg, TU Delft
Prof. dr. ir. M. Kok, TU Delft

An electronic version of this thesis is available at <http://repository.tudelft.nl/>.

Preface

This report about river discharge modelling including surface flow velocities is the master thesis of Sten Schurer. The thesis is written as part of the master program Water Management, track of Civil Engineering at the TU Delft. During the course of this research I got the chance to meet and work with some great people while gaining insights in river discharge measuring and modelling on a practical level during fieldwork in Zambia, as well as a theoretical level during the data processing afterwards.

I would like to thank Hessel Winsemius for giving me the opportunity to work on this very interesting topic, for the second set of RTK equipment he sent to Kenya where I could pick it up, for all the times he offered me his desk and computer so I could keep on working and of course for the general guidance during the whole process. I would also like to thank Willem Luxemburg and Matthijs Kok for their time, guidance and input during our meetings and for the discussions about my research.

I would like to thank Hubert Samboko with whom together I collected the dataset this research is based on. Thanks for your hospitality Hubert, I am looking forward to welcome you in Holland. The fieldwork would not have been a success without you. Furthermore, I would like to thank the University of Zambia and especially Dr. Kawawa Banda for letting me use all measurement equipment I needed for the research. Also I would like to thank the people of WARMA for letting me join their training sessions which brought me quickly up to speed in Zambia.

During the first month of my fieldwork period I did face some 'minor' difficulties with the equipment but there was help from Toni 'RTK' Zeravica. Thank you Toni for all the nights we worked at the tennis court to figure out RTK GPS, twice. Furthermore, I want to thank Ben Dough for his commitment as my boatman on the Luangwa river. It is a shame that you probably never get to read this report, although I hope that research like this improves your situation at the river.

Finally, I am thankful to the university and especially to the people of the Watermanagement department, for providing me research equipment and a very pleasant working environment to finish this research.

*S. Schurer
Delft, August 2020*

Abstract

Rivers have long since exceeded their natural purpose of discharging excess water, by becoming subject to many practical applications demanded by present-day society [61]. In order to comply with this variety of needs and demands, the necessity for proper water management arises, which in turn requires data and knowledge of hydrological parameters like water levels, water quality and river discharge [50].

This research focuses on the hydrological data demand and specifically on the measurement of river discharge. Discharge is generally estimated with intrusive measurement methods [64], this means that the measurement device is in physical contact with the water which can be difficult in strong current or high discharges and even dangerous during floods. Furthermore, in remote and low-resource settings, collecting discharge data is compromised by accessibility problems and difficulties maintaining and acquiring monitoring equipment. When numerous measurements are performed, it is common practice to establish a stage-discharge relationship [66] to facilitate discharge determination, i.e. by shifting to stage measurements. However, due to the empirical character of the method and the sporadic occurrence of high discharges, the relationship can contain considerable uncertainties for these higher discharges [67].

The aim of this research is to provide a sustainable and low-cost data collection and processing method in order to establish a rating curve based on a three dimensional hydraulic modelling approach. One of the main processing methods is Large-Scale Particle Image Velocimetry (LSPIV). LSPIV is a computer based technique that computes flow velocities at the river surface based on video images. Hence, with the development of such a model a more physically based stage-discharge relationship can be determined based on non-intrusive measurements, meaning that measurements can be taken during safe (low flow) conditions in a restricted amount of time. Furthermore, due to the sole use of relatively simple methods and the limited amount of observations needed, this method is particularly suitable for remote and low resource settings.

The study is based on data collected during a two month field trip at the Luangwa river in Zambia. The dataset consists of point clouds collected with the aid of photogrammetry, sonar and RTK GPS which are used to create a bathymetric chart, videos recorded with a drone for the computation of the surface flow velocities, surface flow velocities measured with a current meter for LSPIV validation and discharges measured with an ADCP. The bathymetric chart is used as bed level for the three dimensional discharge model created with Delf3D D-Flow FM which is calibrated with the surface flow velocities (LSPIV) and ADCP discharge measurements.

The discharge model represents approximately 9.2 kilometres of the Luangwa river in length and can reach a maximum width of about 390 metres. The model is calibrated at a discharge of 191 m³/s by minimising the difference between measured and simulated values of ten surface flow velocities and five water levels. This resulted eventually in a Manning friction coefficient of $n = 0.014 \text{ s/m}^{1/3}$. The calibrated model resembles the actual river in location, depth, width and surface flow velocity. The LSPIV velocities are approached to a mean average deviation of 0.07 m/s (1.1 m/s average) and the water level deviates 0.06 m at the research area (1.3 m average). The model is used to establish a stage-discharge relationship which is subsequently compared to two existing relationships, one based on a similar approach using a 1D model and one based on stage-discharge data measured at a conventional gauging station. The three stage-discharge relationships are in the same order of magnitude although the geometry of the river at all sites is likely to be different. Since a stage-discharge relationship is heavily dependent on the geometry [66] this comparison is only a rough indication of the accuracy. Ideally, the discharge, water level, and surface flow velocity should be measured for different discharges and compared (using the model) to the established relationship. The stage-discharge relationship could, if needed, be adjusted based on the new measurements.

Contents

Preface	iii
Abstract	v
List of Figures	ix
List of Tables	xiii
List of Acronyms	xv
1 Introduction	1
1.1 Discharge Measurements	1
1.2 Scope and Aim of the Research	3
1.3 Outline of the Report	3
2 Theoretical background	5
2.1 Measurement Equipment	5
2.1.1 Unmanned Aerial Vehicle	5
2.1.2 Real Time Kinematic Positioning	5
2.1.3 Acoustic Doppler Current Profiler	6
2.2 Large-Scale Particle Image Velocimetry	7
2.2.1 From Particle to Large-Scale	7
2.2.2 Current State	7
2.3 Mapping River Bathymetry	8
2.4 Hydraulic Modelling	9
3 Methodology	11
3.1 Research Area	11
3.2 Determination of the Surface Flow Velocity	12
3.2.1 Acquiring Flow Velocity Data in the Field	14
3.2.2 Processing Flow Velocity Data	15
3.2.3 Validation of the LSPIV Results	15
3.3 Modelling Bathymetry	17
3.3.1 Dry River Bathymetry	18
3.3.2 Wet River Bathymetry	18
3.3.3 Processing Bathymetric Data	19
3.4 The Discharge Model	21
3.4.1 Model Input	22
3.4.2 Model Calibration	23
3.4.3 Model Output	24
4 Results and discussion	27
4.1 Surface Flow Velocity	27
4.1.1 Input Editing	28
4.1.2 Input Length	28
4.1.3 Signal to Noise Ratio	30
4.1.4 Window Size and Overlap	32
4.1.5 Signal to Noise Threshold	33
4.1.6 Changing Circumstances	36
4.2 Bathymetric Chart	37
4.2.1 Wet River Bathymetry	37
4.2.2 Dry River Bathymetry	38
4.2.3 Final Bathymetric Chart	39

4.3 Discharge Model	40
4.3.1 Calibration	40
4.3.2 Model Results	42
4.4 Considerations, Prospects and Limitations	47
5 Conclusion	49
6 Recommendations	53
6.1 Large-Scale Particle Image Velocimetry.	53
6.2 Bathymetric Chart	53
6.3 Discharge Model	54
Bibliography	55
A Surface Flow Velocity	61
B Bathymetric chart	73
C Discharge model	77

List of Figures

1.1	Logarithmic velocity profile over the width (A) and depth (B) of the river as proposed by Von Karaman.	2
2.1	RTK GPS equipment.	6
2.2	Example of Sigma and Z layering.	10
3.1	A: Outline of Zambia including its largest rivers. B: Catchment of the Luangwa river within Zambia. C: Research area at the Luangwa river.	11
3.2	Schematic overview of Large-Scale Particle Image Velocimetry. Please note that the large grid cell size is for illustration purposes.	13
3.3	The three measurement locations for LSPIV. From top to bottom: Measurement with artificial tracers, measurement after a precipitation event and measurement before the event.	14
3.4	I: A represents the first flight pattern. B represents the slightly rotated second flight pattern (image idea is based on the WebODM tutorial [57]). II: The dotted area between image 1 and 2 is the frontal overlap. The gray area between image 1 and 3 represents the side overlap. III: A shows a drone with a nadir viewing camera. B shows a drone with an off-nadir installed camera, in this case a 80 degrees forward facing angle.	17
3.5	The 17 GCPS are evenly distributed over the floodplain and the RTK base station has a clear line of sight with all GCPS. Placing GCPS on the left-bank was not possible due to the geography.	18
3.6	3102 depth measurements are taken in a zig-zag pattern over the river. Another 651 depth measurements are done along the eastern bank, 515 along the western bank and 898 exactly along the waterline at the western bank.	19
3.7	Dense point cloud produced by WebODM with GCP calibration. The cyan line represents the track followed with a trolley with the RTK GPS rover on top.	20
3.8	The WebODM perspective model point cloud shows a clear bowing effect compared to the RTK GPS track. The Brown Conrady model seems to overcompensate.	20
3.9	Overview of all measurements conducted during fieldwork.	22
3.10	The grid made with RGFGRID for a discharge ranging from 5 - 275 m ³ /s. The cell size is smallest at the observation points in the centre of the grid and increases towards the boundaries.	23
3.11	Velocity observation locations.	24
3.12	Stage and discharge plotted on a logarithmic scale in order to determine the stage-discharge relationship at the downstream boundary condition.	24
3.13	The stage-discharge relationship at the downstream boundary condition with which the water level for 67 discharges is determined.	25
4.1	Vector fields produced with LSPIV based on different video editing methods and video length.	29
4.2	The upper plots show LSPIV measurements plotted against current meter measurements with error bars of one standard deviation based on the computed velocities, between all frames, for the window. The lower plots visualize the horizontal and vertical displacement value of each window computed by LSPIV.	30
4.3	Vector fields showing the results obtained by LSPIV while using different methods to determine the signal to noise ratio.	31

4.4	The upper plots show LSPIV measurements plotted against current meter measurements with error bars of one standard deviation based on . Both plots used a different method to determine the signal to noise ratio. The lower plots show the horizontal and vertical velocity vectors computed by LSPIV for both methods.	31
4.5	Vector fields produced by two LSPIV configurations with different window sizes and overlap.	32
4.6	LSPIV statistics produced by two LSPIV configurations with different window sizes and overlap.	33
4.7	The vector fields are obtained by LSPIV using different signal to noise thresholds. Windows in the 'TH 1.0' vector field without a value are rejected by the standard deviation limit or the 50% hit boundary.	34
4.8	Visualized statistics of LSPIV outcomes based on different thresholds for the signal to noise ratio.	35
4.9	Velocity vector field based on the optimal LSPIV configuration determined in this research.	35
4.10	Point cloud of the 'wet' bathymetry at the time of observation. The point cloud is volumized using CloudCompare.	37
4.11	A: Point cloud of the dry river bathymetry at the time of observation. The point cloud is constructed using WebODM and merged with the wet river point cloud in CloudCompare (B).	38
4.12	Distribution of the heights contained by the wet (river) and dry (floodplain) bathymetric charts.	38
4.13	A: The final bathymetric chart of the fieldwork area made with CloudCompare. B: The chart is cut perpendicular to the flow direction in order to extend the chart.	39
4.14	The bathymetry of the fieldwork area is extended in order to mitigate boundary condition errors used in the three dimensional model.	39
4.15	Height value distribution of the final and extended bathymetric chart.	40
4.16	Vertical velocity profiles for a discharge of 191 m ³ /s with $n = 0.014 \text{ s/m}^{1/3}$. Observation point 2 performs best. Observation points 5 & 6 are in the same grid cell and predict a different velocity but both are nearby the simulated velocity.	41
4.17	Visual representation of the discharge model at a discharge of 191 m ³ /s with $n = 0.014 \text{ s/m}^{1/3}$	42
4.18	Visual representation of six discharges simulated by the model.	43
4.19	Three possible datum corrections for the northern cross section.	44
4.20	Three linear regression lines based on the same stage-discharge dataset while using different datum corrections.	44
4.21	Stage-discharge relationships established with different datum correction values combined with the rating curves established by WARMA and Abas [31]	45
4.22	The final stage-discharge relationship plotted with an uncertainty band based on minimum and maximum roughness coefficients according to [39].	45
4.23	Width-discharge relationships for the northern and centre cross sections with an confidence band based on uncertainties in river width estimation and model grid size.	46
A.1	Real Time Kinematic GPS set. Right: the Base, left: the rover.	61
A.2	Setup of the RTK base. Left the GNSS receiver and on the tripod the SimpleRTK2B board with radio module.	62
A.3	Seeding coarse sawdust as artificial tracers in the Luangwa river.	62
A.4	Measuring the surface flow velocity with a current meter from a canoe.	63
A.5	Velocity vector fields for videos with a different editing method.	64
A.6	Velocity vector fields for videos with a different Length.	64
A.7	Velocity vector fields based on different signal to noise ratio determination methods.	65
A.8	Velocity vector fields based on different signal to noise thresholds.	65
A.9	Velocity vector fields for different window sizes and overlap values specified in OpenPIV.	66
A.10	Velocity vector fields for videos recorded under different circumstances.	66
A.11	LSPIV plotted against current meter measurements with error bars of one standard deviation. The results originate form videos edited with different methods.	67

A.12 LSPIV plotted against current meter measurements with error bars of one standard deviation. The results are based on an OpenPIV configuration with different signal to noise determination methods.	67
A.13 LSPIV plotted against current meter measurements with error bars of one standard deviation. The results are based on videos with different length.	68
A.14 LSPIV plotted against current meter measurements with error bars of one standard deviation. The results are based on an OpenPIV configuration with different window sizes and overlap values.	68
A.15 LSPIV plotted against current meter measurements with error bars of one standard deviation. The results are based on an OpenPIV configuration with different thresholds set for the signal to noise ratio.	69
A.16 Velocity vector components V_x (horizontal) and V_y (vertical) compose together the velocity vector computed by OpenPIV. The results originate from videos edited with different methods.	70
A.17 Velocity vector components V_x (horizontal) and V_y (vertical) compose together the velocity vector computed by OpenPIV. The results are based on videos with different length.	70
A.18 Velocity vector components V_x (horizontal) and V_y (vertical) compose together the velocity vector computed by OpenPIV. The results are based on an OpenPIV configuration with different signal to noise determination methods	71
A.19 Velocity vector components V_x (horizontal) and V_y (vertical) compose together the velocity vector computed by OpenPIV. The results are based on an OpenPIV configuration with different window sizes and overlap values.	71
A.20 Velocity vector components V_x (horizontal) and V_y (vertical) compose together the velocity vector computed by OpenPIV. The results are based on an OpenPIV configuration with different thresholds set for the signal to noise ratio.	72
B.1 The ADCP connected to the canoe with the GNSS receiver mounted on top of the sonar.	73
B.2 Cart with the RTK GPS rover on top in order to measure the floodplain and exact waterline.	74
B.3 The slope of the river is 0.0002298, measured over 439 metres with 898 measurements.	74
B.4 The WebODM default model (Perspective) creates a concave shape instead of the desired slope of the RTK GPS track. The Brown Conrady model overcompensates for this deformation and creates a convex shape. Combinations between Perspective and Brown Conrady also do not yield a satisfactory result.	74
B.5 Polynomial curves fit through the point cloud waterlines of different camera calibration models. The polynomials are used to determine the error for each section along the latitudinal axis.	75
B.6 The point cloud made with the ADCP and RTK GPS is transformed to a volumized point cloud in CloudCompare.	76
B.7 The floodplain point cloud is merged with the river point cloud.	76
B.8 A: The point cloud is cut at the up- and downstream boundaries, perpendicular to the direction of flow. B: the extension point clouds stretch approximately 4km to the north and south and are merged with the centre part point cloud. C: the point cloud is volumized.	76
C.1 Cross section as depicted by the Winriver II software.	77
C.2 Delft3D curvilinear grids for different discharges.	77
C.3 The cyan line shows the stage-discharge relationships established over 66 rating points as determined in this research. The three other relationships are established over 16, 11 and 6 of these 66 rating points respectively.	78
C.4 Observation cross sections of the bathymetric chart.	78
C.5 Vertical velocity profiles at all ten velocity observation points in the Delft3D discharge model for a discharge of $191 \text{ m}^3/\text{s}$ with $n = 0.014 \text{ s/m}^{1/3}$. The plots also indicate the surface flow velocity and the depth.	79

List of Tables

4.1	Statistics of LSPIV results based on different video editing methods.	28
4.2	Statistics of LSPIV results based on video length.	28
4.3	Statistics of LSPIV results based on different signal to noise cross-correlation functions.	30
4.4	Statistics of LSPIV results based on different window sizes and overlap.	32
4.5	Statistics of LSPIV results based on configurations with different signal to noise thresholds.	33
4.6	Statistics of LSPIV results based on videos made under different circumstances.	36
4.7	Mean Average Deviation between the simulated and measured values for surface flow velocity and water level.	41
4.8	The stage-discharge relationship constants a and b are strongly dependent on the chosen datum correction.	44
B.1	Absolute errors of the polynomial fitted through the RTK GPS track and the polynomials fitted through the different WebODM calibration models. Please note that the absolute error of the RTK GPS track is the error between the measured line and the polynomial.	75

List of Acronyms

ADCP	Acoustic Doppler Current Profiler
CM	Current Meter
D-Flow FM	Delft3D D-flow Flexible Mesh
DGPS	Differential Global Positioning System
GCPS	Ground Control Points
GIS	Geographical Information System
GNSS	Global Navigation Satellite System
GPS	Global Positioning System
LR	Long Range
LSPIV	Large-Scale Particle Image Velocimetry
MAD	Mean Average Deviation
OS	Original Stabilized
OSG	Original Stabilized Grayscale
OSGG	Original Stabilized Grayscale Gamma
OSGGC	Original Stabilized Grayscale Gamma Contrast
PIV	Particle Image Velocimetry
PTV	Particle Tracking Velocimetry
RTCM	Radio Technical Commission for Maritime
RTK	Real Time Kinematic
RTK GPS	Real Time Kinematic Global Positioning System
SI-LSPIV	Stereo Imaging based LSPIV
SMA	SubMiniature version A
SNR	Signal to Noise Ratio
STDV	Standard Deviation
TH	threshold
UAV	Unmanned Aerial Vehicle
V _x	horizontal velocity vector
V _y	vertical velocity vector
WARMA	Water Resource Management Authority of Zambia

Introduction

Rivers are used for a wide range of practical applications like shipping routes, power source, source of irrigation water, industry cooling water or for recreational purposes. This high level of demand enhances the necessity but also complexity of assessing and managing river water as a resource [61]. In order to meet the challenge, hydrological data like water levels, water quality and river discharge are essential [50]. Discharge measurements facilitate, amongst others, management of irrigation, industry and drinking water uptake and can predict downstream flooding or possible droughts. Furthermore, measuring discharge can help with the understanding of hydrological processes, the design of hydraulic structures and efficient water allocation.

1.1. Discharge Measurements

The necessity of monitoring rivers in both water quality and quantity is highlighted especially during periods of drought or flooding. For example, the evacuation of 'het Rivierenland' (the Netherlands, 1995) when 250.000 individuals were evacuated during extremely high water levels in the rivers Meuse and Rhine [28]. Without accurate discharge measurements the evacuation would likely not have been summoned with possible disastrous consequences. This need for river monitoring culminates in a continuous search for innovative measurement techniques that are cheaper and easier to use with even better accuracy than their predecessors [47] [46].

Nowadays there are various ways to determine river discharge, for instance by using a float, the moving boat method, a weir, a flume or a current meter [83]. Which technique is best will be determined by the river characteristics, available budget and desired accuracy. Perhaps the simplest discharge measurement technique is a float. The technique makes use of a floating object of which the time is recorded that it takes to cover a certain distance when thrown in the water. The object can be, e.g., a bottle partly filled with water or a tree trunk already floating in the water during high water levels. The flow velocity is preferably determined several times distributed over the river width, then translated in vertical averaged velocity and subsequently multiplied with the corresponding cross sectional area to obtain the estimated discharge. This is known as the velocity-area method. Using a float can be useful to quickly get a rough idea about the discharge but with minimal accuracy [64].

Discharge measurements at gauging stations have generally been performed with more sophisticated devices like current meters, structures or (more recently) Acoustic Doppler (Current) Profilers [52]. These measurement techniques generally achieve a higher accuracy [64] but also have their limitations. For example, most methods only work in a certain range of discharges, can be costly, time consuming or require an expert. Furthermore, many measurement methods are intrusive [64], which means they have to be in physical contact with the water in order to measure. Using intrusive methods can be difficult with strong current or high discharges and even dangerous during floods. Moreover, in remote and low-resource settings, collecting discharge data is compromised by accessibility problems and difficulties maintaining and acquiring monitoring equipment.

Although most discharge measurement techniques are intrusive, there are exceptions. These non-intrusive techniques are generally based on radar, images or remote sensed data [64] and, like most intrusive methods, indirect measurements. The image based techniques do possess certain advantages as they are relatively inexpensive, suited for a broad range of discharges, have no moving parts, and can provide continuous data [14]. Furthermore, these techniques are used to measure river discharge since the mid-1990s [33] but still developing due to continuous technological improvements of, e.g., cameras and drones. One of these techniques is Large-Scale Particle Image Velocimetry (LSPIV). LSPIV is based on video analysis and visualizes the surface flow by following objects (tracers) floating on the river. The video is analysed frame by frame in which tracer patterns are recognized through which the direction and speed of the surface flow is determined. Provided that there are sufficient tracers in the river and other conditions are met, LSPIV results in surface flow velocity over time.

The most widely used method to compute discharge from the surface flow velocity is the velocity-area method (similarly used in the float method) [14] [3] [25]. The velocity-area method links the surface flow velocity directly to the discharge by using a logarithmic velocity profile (Figure 1.1 B) [14] or by multiplying the surface flow velocity with an index velocity value (between 0 and 1) and the cross sectional area [52].

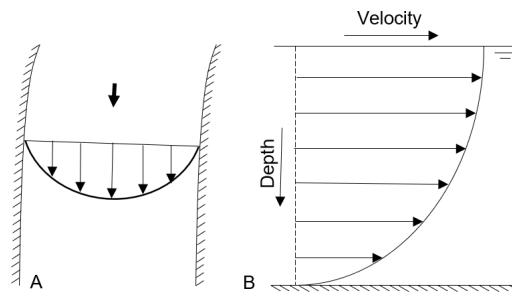


Figure 1.1: Logarithmic velocity profile over the width (A) and depth (B) of the river as proposed by Von Karaman.

The logarithmic vertical velocity profile is proposed by Von Karaman [78] and stated as: the average velocity of a turbulent flow at a certain point is proportional to the logarithm of the distance from that point to the river bed or bank (Figure 1.1). However, due to the complexity of natural river beds and river cross sections, measured vertical velocity profiles frequently show mixed characteristics of parabola lines, power or logarithmic distribution lines [76]. The general practice would be measuring the velocity at several depths to construct the profile. With LSPIV however, the only velocity available is the surface flow velocity where, according to Song [76], the highest estimated error in predicting the vertical velocity profile appears. Furthermore, the vertical velocity profile is not static over time but fluctuates with the discharge and possible shifting riverbed. Considering the above, linking the surface velocity directly to the discharge seems to produce, perhaps unnecessary, high uncertainty.

When discharge is measured, it can be linked to the local water depth at the time of measuring. If this link is made several times, for varying discharges at a fixed location, it is possible to construct a relationship between the discharge and the water level (provided that the hydraulic geometry is stable over time). This is known as a stage-discharge relationship or rating curve. Developing such a relationship requires a significant amount of water levels with corresponding discharges called 'rating points' [8]. The stage-discharge relationship is then established by fitting a curve through the rating points. Rating curves may be simply linear with a single segment or may be complex with several segments, loops and inflections [67]. Since this relation is based on solely empirical data, there should be a significant amount of rating points for a fit through the lower and medium stages, however, higher stages occur less frequent and will therefore manifest as more uncertain in the fitted curve [67]. Regarding the sporadic nature of high discharges and the associated difficulties with measuring, it is in most cases necessary to resort to extrapolation, resulting in larger uncertainties under high flow circumstances.

1.2. Scope and Aim of the Research

Regarding the difficulties associated with intrusive techniques and rating curves during high water levels, a non-intrusive physically based measurement technique seems the way forward. A non-intrusive technique would resolve the dangers concerning measurements in strong currents or during floods, whereas a physically based technique would be less dependent on the occurrence of peak discharges. Furthermore, the measurement technique should especially be suited for application in low-resource settings and therefore be easy to use while employing only relatively low-cost equipment. With all this taken into account, the aim of this research is to provide a sustainable and low-cost data collection and processing method in order to establish a rating curve based on a three dimensional hydraulic modelling approach. The river discharge model will be dependent on surface flow velocities measured with Large-Scale Particle Image Velocimetry (LSPIV). Simulating discharge based on LSPIV input makes for a non-intrusive method while the model, based on the shallow water equations [16], provides the physical base. Furthermore, the model excludes the velocity-area method and therewith part of the uncertainty in LSPIV discharge estimates.

In order to establish a three dimensional discharge model in which surface flow velocities are used for calibration, a bathymetric chart of the research site is required, the method to obtain this chart represents a significant part of this thesis. The bathymetry will serve as the 'base' of the model over which the water flow can be simulated. Furthermore, the discharge at the time of the surface flow velocity observations needs to be known for calibration purposes as well as the exact locations of all acquired measurements [16]. Therefore this study makes use of sonar, photogrammetry and a Real Time Kinematic Global Positioning System (RTK GPS). The goal of this research is to examine whether or not LSPIV can help in establishing a three dimensional hydraulic river model. This leads to the main research question:

How can optical surface flow velocity estimations, sonar and photogrammetry be used to establish a discharge model of medium-sized rivers?

In order to answer the main question the following research questions are formulated:

- I How to utilize Large-Scale Particle Image Velocimetry to obtain surface flow velocity estimations intended for the use in a 3D discharge model?**
- II How can a bathymetric chart of a river be established based on photogrammetry and sonar data?**
- III How can surface flow velocity estimations be implemented in a 3D discharge model?**
- IV How does the model perform compared to conventional measurements?**

The research questions will be answered using data obtained during fieldwork at the Luangwa river in Zambia. After formulating the research objective and the above mentioned research questions the data is collected during a nine week field trip to Zambia. The gathered data is afterwards processed to obtain answers to the research questions.

1.3. Outline of the Report

The research is set forth in 5 chapters that together compose this report. The content of each chapter is divided in three parts. Part one concerns LSPIV and therewith the first research question, the second part involves the bathymetry regarding the second research question, Part 3 combines research question three and four by describing the model, which uses the results of LSPIV and Bathymetry as input.

Chapter 1, gives an introduction to the subject as well as the motivation, objective and scope of the research. The main question is presented and subdivided in four research questions.

Chapter 2, describes the most important measurement devices used during the fieldwork. Thereafter a concise theoretical background is provided.

Chapter 3, provides a description of the research area followed by an explanation of the methods used during the fieldwork as well as the data processing. Each part starts with a general explanation of the methods followed by a more detailed description of how these methods are utilized.

Chapter 4, the results are set forth and discussed.

Chapter 5, presents the main conclusions drawn from the results and answers the main question.

2

Theoretical background

The following chapter provides general background information to the main topics of this research. The information can be consulted for a broader understanding of a particular aspect or for a clearer overview of the research as a whole. The chapter is divided in four sections: section one explains the set-up and functioning of measurement equipment used during the fieldwork, section two gives a concise background on LSPIV as a discharge measurement technique, section three covers different methods used to establish a bathymetric chart and section four provides the basics of hydraulic modelling.

2.1. Measurement Equipment

Fieldwork for technical research purposes generally entails gathering data and understanding site specific features. The data is often collected with measurement equipment purposely developed for the measurement of specific features. However the outcome of a fieldwork depends on the suitability of the equipment, it must be noted that it depends, at least as much, on the skills of the researcher employing it. In this section the most important equipment used during the fieldwork of this research is described.

2.1.1. Unmanned Aerial Vehicle

An Unmanned Aerial Vehicle (UAV) is the collective term for all autonomously flying air-crafts. In this research the term refers to a drone and is often described as such. The drone is equipped with a camera and deployed for photogrammetry on the floodplain and recording videos of the river surface. The drone is a DJI Phantom 4 with a standard camera able to record in 4K resolution. Furthermore, the drone is equipped with a 64GB U3 SD card in order to have enough storage space and writing speed to record high quality videos at high frequency. The flight planning software is Pix4DCapture and is used on an Android phone.

2.1.2. Real Time Kinematic Positioning

In order to log specific measurement locations during fieldwork an accurate Global Positioning System (GPS) is required. Most common single-frequency GPS devices (e.g. smartphones) have an average accuracy varying between five to ten metres due to various sources of possible errors [70], which is not accurate enough for many research objectives. More accurate is a Differential Global Positioning System (DGPS). This special type of GPS makes use of a fixed ground station (base) that sends corrections to a GPS receiver used for the actual measuring (rover), this allows a DGPS to have an accuracy of several decimeters depending on the circumstances [30]. An even more accurate measurement, in the order of centimeters (or even millimeters with long-term measurements), can be achieved with Real Time Kinematic (RTK) GPS [80]. Like DGPS, RTK makes use of a base station, a rover and the Global Navigation Satellite System (GNSS). Unlike DGPS, Real Time Kinematic uses phase differences of the satellite signals to correct the position instantly (both base and rover) [30]. The time between starting the base station and measuring with the rover determines in part the absolute accuracy of the measurements since the base will be able to determine its location more accurate over a longer time span. Other factors are the distance between the rover and base, meteorological conditions, the line of sight between the receivers and the use of single or multi-band frequency.

This research used two SimpleRTK2B boards with u-blox-ZED9P modules (Figure 2.1 A and C) in order to create an RTK GPS. These boards are able to convert multi-band signals with a centimetre level precision [9]. The first board is configured as base station using U-center (related software, version 19.10) with the standard configuration file provided by u-blox. The second board is configured with the standard rover configuration file. The used GNSS receivers are u-blox Multi-band ANN MB-00 supporting GPS, GLONASS, Galileo, and BeiDou, they are connected to the SubMiniature version A (SMA) connection on the boards (Figure 2.1 D). The connection between the base and the rover can be made with a 4G network connection or with long range radio modules.

When making use of the 4G network, the base is connected via the USB port to a Raspberry Pi Zero W while the UART2 port is short-circuited. The Raspberry Pi is connected to the 4G network via a smartphone hotspot connection and sends so called Radio Technical Commission for Maritime (RTCM) messages (correction messages) to the SNIP NTRIP caster (Networked Transport of RTCM via Internet Protocol). The rover is connected with another Raspberry Pi Zero W. This Raspberry Pi retrieves the RTCM messages from the NTRIP server and sends them to the rover's SimpleRTK2B board where the u-blox module (Figure 2.1 C) uses them to correct the location obtained by its own GNSS antenna.

If the internet connection at a research site is unstable or non-existent, it is possible to send the RTCM messages with radio modules produced by XBEE (Figure 2.1 E). The so called XBEE shields are, just like the SimpleRTK2B boards, configured with standard configuration files for base and rover with the XCTU application [18]. The shields are connected to the UART-2 connection on the boards and to a Long Range (LR) radio antenna (Figure 2.1 B). The antennas can communicate to a maximum distance of 10 to 14 kilometres depending on the location [10].

The rover is in both setups, via the USB port, connected to a smartphone running the application SWMaps. SWMaps is a Geographical Information System (GIS) application for collecting, presenting and sharing geographic information [49]. SW Maps can log the location of the GNSS antenna of the rover (corrected with the RTCM messages) manually or automatically with a certain time interval.

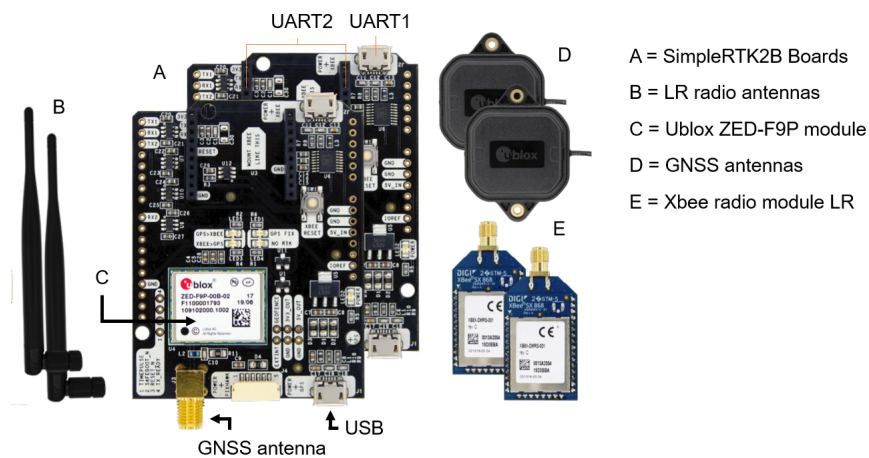


Figure 2.1: RTK GPS equipment.

2.1.3. Acoustic Doppler Current Profiler

An Acoustic Doppler Current Profiler (ADCP) is a hydro-acoustic current meter often mounted on a small boat that uses acoustic pulses to measure flow velocity over the depth of a water column (Figure B.1). When an ADCP measures continuously while moving across a river (perpendicular to the flow) it results in a cross section showing the depth and flow velocity in 2D (Figure C.1). Subsequently the ADCP can determine the discharge using the velocity-area method. An ADCP is in general a user-friendly and fairly accurate discharge measurement technique [72]. However, in turbid water the device can have difficulties penetrating towards the bottom and an ADCP cannot measure the velocity close to the bottom and at the sides of a transect, therefore it has to extrapolate. In this research the Teledyne RiverRay ADCP is used with a velocity profiling range up to 60 metres [36] in combination with the accompanying software WinRiver II (version 2.16).

2.2. Large-Scale Particle Image Velocimetry

Large-Scale Particle Image Velocimetry (LSPIV) is an image based measurement technique used to visualize and quantify flow velocities at the free surface of a water body [52]. LSPIV originates from Particle Image Velocimetry (PIV), a technique that observes small scale displacement in a fluid based on recognizable features, so called 'tracers'. The distinctive properties of LSPIV are the focus on a larger observational area (e.g. a river surface) and exclusive focus on surface velocity whereas PIV can also be used to reconstruct three dimensional velocity fields in experimental setups [55]. LSPIV determines the displacement between two or more consecutive images using a cross correlation function that can identify patterns of tracers within the images [35]. First, each image is divided in several smaller areas called windows, hereafter the cross correlation function searches for tracer patterns in each window. Within the consecutive image the same tracer patterns are located resulting in a displacement value for each window (due to the river flow). When the displacement is determined it is divided by the time interval between the two images resulting in a velocity vector for each window. The vector field of surface flow velocities can subsequently be used to estimate river discharge by e.g. using the velocity-area method [53] (See 3.2 for a more elaborate explanation of LSPIV and how it is used in this research).

2.2.1. From Particle to Large-Scale

The first relation between LSPIV and river discharge is made in 1994 by Fujita and Komura ([32] as mentioned in [35]), although observation, quantification and measurement of fluid in motion was already widespread at the time in many study areas. In 1968, Goodman published a comprehensive book explaining optical data processing and imaging techniques [82] and Van Dyke visualized fluid motion in an impressive album in 1982 [56]. Early studies with respect to flow visualization focused on experimental setups where fluid motion is analysed in a controlled environment on a small scale (i.e. square centimetres, PIV) [84] [37]. In 1991, different PIV techniques for fluid velocity measurements are described in an extensive paper by Adrain [38] and a year later the status and trends of PIV are described by Buchhave [63]. Both conclude that PIV has several promising advantages over conventional measurement techniques but that a number of technical challenges must be overcome to be truly useful in the field of fluid mechanics. An interesting bottleneck both papers highlight is the required computational time, due to the available computational power at that time only a few images could be processed in a day [63]. This is scarcely believable knowing that the software in this research processes 16 images per minute, with 1600 windows per image. Furthermore, Buchhave describes the transition in terminology as the technique was originally referred to as Particle Image Displacement Velocimetry, PIDV. The leap towards large-scale observations is presented in 1971 by Leese [6] who used recordings to track the motion of clouds based on cross-correlation. Subsequently other fields of study adopted the large-scale application in order to visualize the motion of, e.g., sea-ice [54] [58] or the sea-surface [81] based on satellite data. As of the first proposed relation between LSPIV and river discharge [32] numerous studies are conducted in which the performance of the method, in different capacities, is tested [41] [91] or in which more practical adjustments are proposed [26]. Besides the need for adjustments from conventional PIV methods, scaling-up the observation area also implied a transition from controlled lab experiments towards field observations.

2.2.2. Current State

In recent years numerous studies stretched the possibilities of LSPIV as a discharge measurement technique. For instance, three-dimensional water surface reconstruction is combined with surface velocity measurements by using Stereo Imaging based LSPIV (SI-LSPIV) systems [86] or automated LSPIV systems for continuous measurements using a Raspberry Pi [65]. Other studies stand out by originality, like post-flood determination of discharges based on Youtube videos [69] or a study where images are collected by use of a helicopter [34]. Perhaps the use of a helicopter seems somewhat excessive but it comes forth from a basic requirement of LSPIV: the necessity of recording images from a high standpoint in order to cover the entire width of the river. Several solutions for a high standpoint are applied, e.g., a hydraulic mast [25], a bridge [23] or an Unmanned Aerial Vehicle (referred to as drone) [74] [85]. When using a helicopter or a drone the technique is specified as aerial LSPIV [34].

Nowadays the application of drones seems to be the most widely adopted technique [71] [85] [74] since it provides the possibility to record from a viewpoint orthogonal to the river surface (at nadir), i.e.,

not in an angle with the river surface. However recording off-nadir is possible, it requires an extra processing step called orthorectification which still poses a major hurdle in LSPIV [22]. Orthorectification adjusts the image from an off-nadir towards a nadir point of view based on recognizable features in the image of which the exact position is known (GCP'S) [53] [22].

Over the years, two imaging techniques seem to be used most frequently in LSPIV, namely Particle Image Velocimetry (PIV) and Particle Tracking Velocimetry (PTV) [23]. PIV tracks certain tracer patterns where PTV tracks single tracers between consecutive images [23]. Nowadays, both PIV and PTV are utilized in different LSPIV software packages. For example, the user-friendly software package Fudaa LSPIV uses PIV [51] whereas other packages that can be imported in, e.g., Python or Matlab use PIV, PTV or a combination of both [45] [88]

LSPIV is now regarded as a reliable and broadly used technology to measure river surface flow velocity [24] [77] [69]. However, LSPIV has still several limitations. The following selection of limitations is applicable to this research.

- Measuring surface flow velocities of large rivers (i.e. large width) is complicated due to the present day camera resolution.
- Tracers are often not available.
- Reflection on the water surface makes tracking difficult.
- Generally the surface velocity is directly linked to discharge with a velocity index or a log-function, this link often entails high uncertainty.

The first limitation is rather practical, natural tracers are generally too small to detect in a large area using 4K resolution and seeding significant amounts of large tracers on a wide river is at least inconvenient. The second and third limitations are dependent on the river characteristics and meteorological conditions and can therefore be overcome by proper location choice, seeding artificial tracers and recording at suitable moments. The final limitation, and perhaps the most interesting, can be overcome by substituting the velocity-area method with a method that does not link the velocity directly to the discharge like a three dimensional discharge model.

2.3. Mapping River Bathymetry

Mapping the bathymetry of a river and therewith creating a bathymetric chart can be done in several different ways, for example by using a sonar, remote sensed data or simply wading through the river and doing manual point measurements [21] [42] [60]. Which way is best will mainly depend on river characteristics like turbidity and size, but also on the required accuracy and precision of the chart. These requirements are, in turn, dependent on the application of the bathymetric chart.

Bathymetric charts of river beds are often used in hydraulic models for simulating flow dynamics, flood forecasting, sediment transport or morphological changes [21]. Before 1990 the majority of these numerical hydraulic models were one dimensional [27], i.e. cross sectional, however, with the emergence of computers and the rapid development of their computational power the numerical models started to gain complexity and shifted often to two dimensions [48]. These two dimensional models allowed for a spatial representation of the river by solving the shallow water equations for a mesh of grid cells for which a (detailed) bathymetric chart was required [48].

Nowadays, both two and three dimensional hydraulic models require accurate bathymetric charts of river beds and floodplains [21]. Establishing such a bathymetric chart requires both mapping of dry ground (the floodplain) and a submerged area (the river). Mapping the floodplains can be done using airborne or space-borne methods [20], whereas this is not directly possible for the submerged part of the area. According to Bandini [21] this complexity in measuring the topography of the submerged river caused a global deficiency of bathymetric measurements for inland waters.

The main advantage of remote sensed analysis of a river bathymetry over manual surveys is the ability to effectively obtain quantitative spatially distributed data over large areas [7] [43]. Therefore

many studies research the possibility of using remote sensed data in order to map the submerged area of a river. Most studies are focused on remote sensing imagery that uses visible wavelengths since these waves have the smallest attenuation in water [21]. Although this attenuation is smaller for visible light, the penetration depth is strongly dependent on the turbidity of the water, and is generally not more than approximately one Secchi depth [21]. In practice this means that only shallow rivers containing very clear water can be mapped under the right atmospheric conditions [44] [21].

In order to mitigate the depth issue, research has moved to LiDAR data, more specifically to the green wavelength of LiDAR data [43] [42]. LiDAR, short for Light Detection And Ranging, is a remote sensing technique that uses laser light to create elevation models and from which the green wavelength has the smallest attenuation in water. However, LiDAR data is also constrained by the turbidity of the water. According to Guenther [11], LiDAR data can penetrate the water to approximately 2-3 times the Secchi depth.

Since both aerial and satellite imagery are nowadays not able to penetrate turbid water to the often required depth, bathymetric charts are generally established with field surveys using floating sonars [21]. These sonars are usually carried by a boat or floating vessel (like an ADCP) while sending sound beams towards the bottom. Sonars come in the single- and multibeam variant where the multibeam sends multiple soundwaves in a wide array towards the bottom thereby creating a more detailed representation of the river bed [40].

2.4. Hydraulic Modelling

In this section some fundamental aspects of hydraulic modelling are discussed in order to better understand the three dimensional discharge model presented in this research. Hence, the theory in this section is confined for that which is relevant to free surface river flow and specifically concentrates on Delft3D D-Flow Flexible Mesh models. When working with software like Delft3D FM it is of importance to know the physical basics underlying the software and understand the limitations of the assumptions made during model development in order to employ the software effectively [59].

Two or three dimensional numerical hydraulic models generally solve the non-linear shallow water equations [59]. These equations can be derived from the three dimensional Navier-Stokes equations for incompressible fluid [16] [59], which are, in turn, based on two basic principles, the conservation of mass and the conservation of momentum. In hydraulic models (including Delft3D D-flow), the shallow water equations, which are a set of partial differential equations, are generally complemented with initial and boundary conditions.

The shallow water equations are derived from the Navier-Stokes equations under the assumption that the depth is much smaller than the horizontal length scale [59]. This means that the vertical momentum equation is reduced to the hydrostatic pressure relation [16]. This assumption, accompanied by many more assumptions and approximations, therefore applies to all models constructed with Delft3D D-Flow. The most relevant assumptions in Delft3D D-Flow FM for the discharge model presented in this research are:

- The flux of water through the river bed (infiltration) is always zero
- The exchange of water with the free surface is zero
- In 3D models the vertical velocities are computed from the continuity equation
- The effect of variable density is only taken into account in the pressure term
- The effect of the earth curvature is not taken into account and the Coriolis parameter is assumed uniform

With these assumptions and a set of initial and boundary conditions, the shallow water equations can be solved on an (un)structured grid [16]. This grid can consist of just one or several layers in the vertical, i.e. resulting in a 2 or 3 dimensional model respectively. Within Delft3D two different layering methods are provided for 3D models, the sigma σ method and the Z-method. The Z-method is based on the Cartesian Z-coordinate system resulting in straight horizontal coordinate lines nearly parallel with the density interfaces [16]. The sigma layers, on the contrary, follow the bed topography and, hence, they differ spatially in thickness (Figure 2.2).

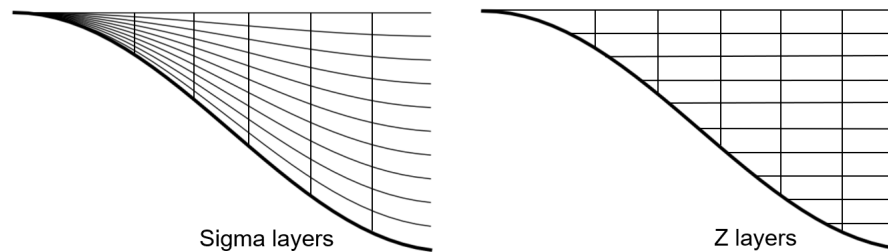


Figure 2.2: Example of Sigma and Z layering.

A hydraulic model consisting of a bed level, a grid structure, mathematical formulations describing the physical processes and corresponding necessary assumptions and approximations does need boundary conditions in order to simulate the desired hydraulic processes. In case of a river model these boundary conditions do often comprise an inflow and outflow of water implied by a discharge, velocity or water level. In Delft3D D-Flow models these boundary conditions can be imposed as a timeseries or as a harmonic signal [16],

Besides the boundary conditions, there are initial conditions and physical parameter values to be assigned to the model, for example initial water levels, the water temperature and a uniform friction coefficient. This friction coefficient influences the maximum velocity of the water at the river bed and therewith effects the discharge capacity and water level in the simulation [1] [16]. The roughness can be described by different formulations like Chézy, Manning or White-Colebrook which all contain a certain roughness coefficient that needs to be specified [16].

In hydraulic modelling it is common practice to use this roughness coefficient for model calibration [87]. Calibration with this coefficient provides the opportunity to fit the model accurately to the test data and therewith encapsulating most of the uncertainty in the roughness coefficient. When the coefficient lies within reasonable boundaries it is easily accepted but the accuracy of the coefficient remains unknown. Therefore, it is advisable to estimate the roughness coefficient, or a range of coefficients, in advance of the modelling process based on site specific features. This restricts the model to get an accurate fit at the expense of the roughness coefficient accuracy [87].

3

Methodology

The methodology chapter is divided in four sections each dealing with a defined part of this research. The first section describes the research area and its characteristics. The second and third section describe all steps followed during the surface flow velocity measurements and the construction of the bathymetric chart respectively. In the fourth and final section the bathymetric chart converges with all measurements into a discharge model. The model setup is set forth, parameter values are dealt with and finally a stage-discharge relationship is constructed. The methodology is written to facilitate both reproduction and continuation of this research, all used scripts can be found in a GitHub repository [75].

3.1. Research Area

The research area is located at the Luangwa river in Zambia (Figure 3.1A). The Luangwa river flows from the Mafinga Hills in the north towards the confluence with the Zambezi river in the south. The Luangwa has a length of 850 kilometres and comprises the third largest catchment within Zambia covering approximately 145,690 km² (Figure 3.1B) [89]. The Water Resource Management Authority of Zambia (WARMA) describes the main stem of the Luangwa as unregulated and pristine [89]. The research area is located 2 kilometres south of the Luangwa Bridge and 80 kilometres north of the confluence with the Zambezi river (Figure 3.1B).

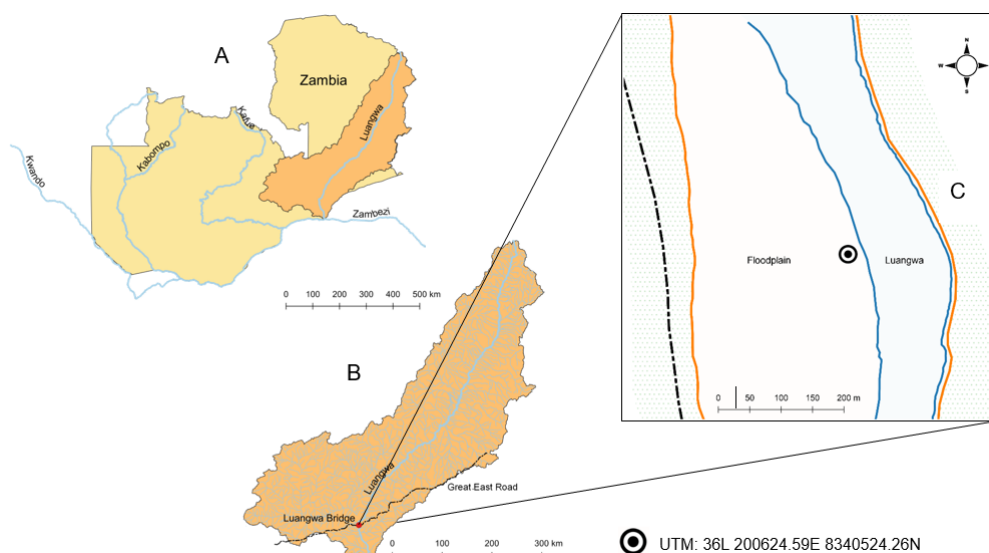


Figure 3.1: A: Outline of Zambia including its largest rivers. B: Catchment of the Luangwa river within Zambia. C: Research area at the Luangwa river.

Zambia generally knows a dry (April-November) and a wet season (October - May), however, this rainfall pattern is variable and seems to shift due climate change [15]. The Fieldwork is conducted in the second and third week of December 2019. Although December is situated in the rainy season, the seasonal rains had not started yet. The average river width at the research site during time of observation was 120 metres with a maximum depth of 3.50 metres and a mean surface flow velocity of 1 m/s. The floodplain width was approximately 200 metres (Figure 3.1C).

3.2. Determination of the Surface Flow Velocity

The following section describes the methodology regarding the determination of river surface flow velocities. These velocities are computed with a technique called Large-Scale Particle Image Velocimetry (LSPIV). The technique requires videos of the river surface which are made during fieldwork. The general LSPIV workflow is modified in this research since the acquired velocities are used for calibration purposes only. This section discusses all modifications that eventually lead to an optimal utilization of LSPIV regarding a three dimensional discharge model and therewith formulates an answer to the first research question:

I How to utilize Large-Scale Particle Image Velocimetry to obtain surface flow velocity estimations intended for the use in a 3D discharge model?

As stated, the surface flow velocity of the Luangwa river is measured with the use of Large-Scale Particle Image Velocimetry. LSPIV is a computer based technique that uses cross-correlation functions to obtain flow velocities based on video images [23], as explained in section 2.2. There are different options for LSPIV algorithms, most are software packages that need additional programs (e.g. Matlab or Python) like OpenPIV, PIVlab or MatPIV, however, there are stand-alone software packages available with user-friendly front ends like Fudaa-LSPIV. For this research OpenPIV is used. OpenPIV is an open source PIV package available for Matlab, C++ and Python. This research uses the Python package on the Anaconda platform since this combination provides the possibility to modify the process.

OpenPIV computes the surface flow velocity as follows. The video is cut in single images, these images are subsequently divided in grid cells, also called windows (Figure 3.2A). Within these windows OpenPIV searches for recognizable features floating on the river surface, these features are referred to as tracers (Figure 3.2B). In the consecutive image the same tracers or pattern of tracers are searched for. A match within the search area results generally in both a horizontal and vertical displacement due to the flow velocity. In order to speed up the process the software is only searching in a specified area called the search area, this area is located downstream of the window (Figure 3.2C). The size of the search area has to be chosen carefully, the area should be big enough to contain the tracers but as small as possible to ensure a reasonable processing time. For computing the velocity, the distance between tracers and the time step between images are required. Since the traveled distance of the tracers is expressed in pixels, the pixels per metre ratio has to be calculated. Measuring the distance in meters is done with Ground Control Points (GCPS) (Figure 3.2D). In Figure 3.2E six GCPS can be seen of which the exact location is recorded. Dividing the number of pixels between the GCPS with the exact distance in metres returns the pixel per metre ratio. The time step stems from the frame rate of the video. With the displacement, pixel/metre ratio and time step the velocity and direction of the tracers within the window can be determined. OpenPIV computes this velocity vector for all windows and all images, resulting in a vector field.

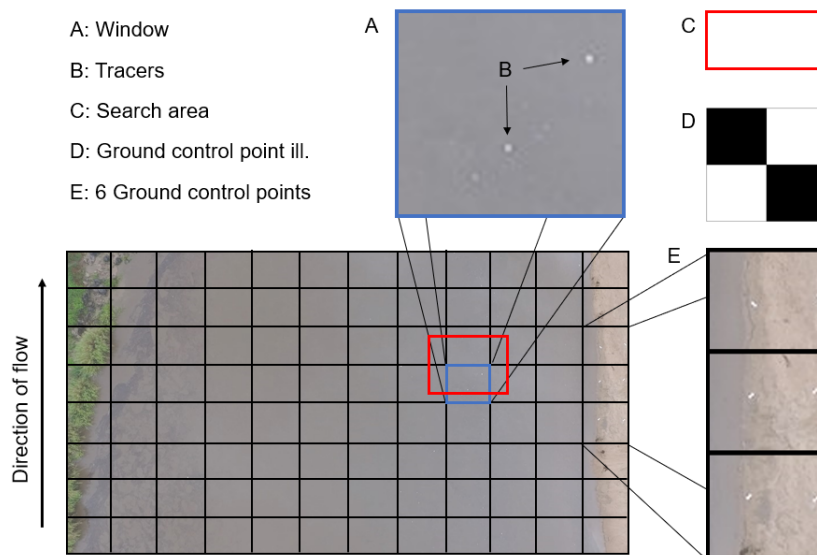


Figure 3.2: Schematic overview of Large-Scale Particle Image Velocimetry. Please note that the large grid cell size is for illustration purposes.

For LSPIV, fieldwork consists of making a video of the river surface and collecting GCP locations. This makes LSPIV a non-intrusive measurement technique, which incorporates certain advantages as mentioned in section 1.1. Evidently, each video should comply with certain requirements for LSPIV to be applicable.

Most important is the presence of tracers, preferably tracers that move with similar speed as the water itself. The tracers can be natural or artificial. Examples of natural tracers are leaves and branches (washed in the water by overland flow) or foam (created by e.g. rapids). If there are not sufficient natural tracers it is possible to seed artificial tracers like wood chips or sawdust.

Another requirement is the minimisation of specular reflection. Specular reflection is the mirror like reflection of smooth surfaces [5]. Specular reflection on rivers occurs when the surface is smooth (i.e. without ripples or waves) in combination with sufficient sunlight and little cloud cover. For videos with strong reflection it is unlikely for LSPIV software to detect tracers ([4] as mentioned in [53]). Therefore, the videos were shot during cloud cover or just before sunrise.

Within the video there should be several marker points, or GCPS, of which the exact location is known. The GCPS should be placed with some distance from each other in order to minimize the influence of measurement errors.

Other requirements are associated with the camera and its settings. The camera needs to be at a fixed and stable position. If the position is at an angle with the river surface (other than 90 degrees), the video needs an extra step in the editing process called orthorectification. Additionally, the pixel/surface ratio becomes smaller with an increasing distance and a decreasing angle. Therefore, the minimum required angle is dependent on the river width. Furthermore, a high resolution is desirable in order to detect small tracers while the frequency, or frame rate, is of less concern since this can be compensated for with the search area size.

3.2.1. Acquiring Flow Velocity Data in the Field

The free surface flow velocity data of the Luangwa river is acquired at three different moments under varying conditions (Figure 3.3). On the 13th of December videos are shot before (at 07AM) and just after (at 10AM) a precipitation event. The event lasted for about an hour but did not affect the river flow at the research site given the local character of the event and the size of the river. However, the amount of tracers increased significantly, likely as a result of overland flow. The third moment was at December the 18th at 6AM, before sunrise to overcome the influence of specular reflection. For this video coarse sawdust (pieces of $\pm 1\text{cm}^2$) is seeded as artificial tracer. The seeding is done with the help of three canoes (Figure A.3).

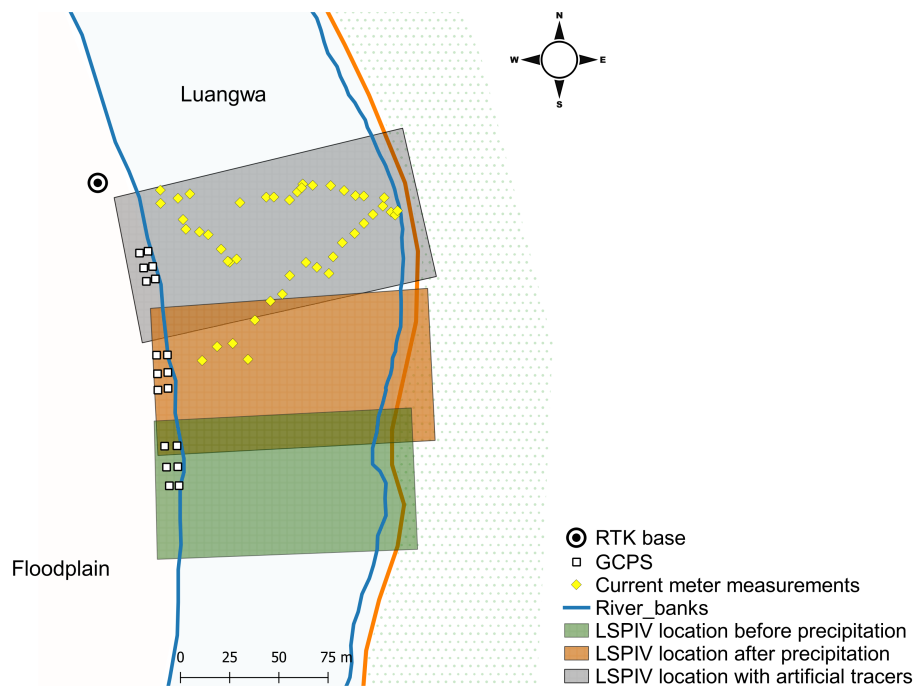


Figure 3.3: The three measurement locations for LSPiV. From top to bottom: Measurement with artificial tracers, measurement after a precipitation event and measurement before the event.

All videos are shot orthogonal with the water surface. For this a drone is used (DJI Phantom 4) with a standard camera containing 12.4M effective pixels [19], as explained in section 2.1.1. The videos are shot at a frame rate of 24 or 30 images per second and vary between 10 and 60 seconds in length.

All videos contain six GCPs. The exact location of each GCP is determined with Real Time Kinematic GPS (see Chapter 2 for a detailed description of RTK GPS). The SimpleRTK2B board with radio module of the base station is placed on a tripod with a height of approximately 2.5 metres above the floodplain in order to have a clear line of sight with the rover (Figure A.2). Regarding the accuracy, the base was up for at least one hour before the location measurements.

For validation of the LSPiV results, the surface flow velocity is measured with a current meter (see Chapter 2). The flow velocity is measured 50 times (Figure 3.3) while going from bank to bank in a canoe. During each measurement the propeller of the current meter is placed just below the water surface alongside the canoe which is held as steady as possible in the current by the boatman (Figure A.4).

3.2.2. Processing Flow Velocity Data

The process of converting a raw video into an average flow velocity field consists of several steps as explained in section 3.2. The following section sets forth the exact method used in this research and elaborates on chosen parameter values in a chronological order. Before using a video as input for LSPIV software it can be beneficial to edit the video [23]. Whereafter the general parameters can be specified and the process initiated.

Since the videos are shot with a drone they often contain vibrations and small movements (e.g. due to wind) therefore, the videos are stabilized. In this research the stabilization function of the python package OpenCV is used (see the GitHub repository for the stabilization script [75]).

Converting the video to gray scale and lowering the gamma value accentuate the generally lighter tracers against the darker background of the river water ([23] as mentioned in [2]). Furthermore, the contrast can be enhanced by adjusting the alpha and beta values in the video. The gray scale, gamma and contrast adjustments are also performed with OpenCV (see the Github repository for the editing script [75]). The edited videos need to be saved as images when used as input for the OpenPIV package.

In OpenPIV the following parameters need to be specified: window size, search area size, overlap of the windows, frame rate, and scaling factor (pixels/metre ratio) (a more detailed description of the parameters can be found in section 3.2). Additionally, OpenPIV uses a Signal to Noise Ratio (SNR) to remove windows with high uncertainties in the predicted velocity [29]. The SNR is described as the ratio of the signal power to the noise power [90]. Within one window and its corresponding search area, each cross correlation function contributes to a correlation plane. The correlation peaks along this correlation plane correspond to correlations between image pairs [90]. The highest peak is assumed to be the true displacement, the 'signal', the other peaks represent the 'noise'. The SNR can be calculated in two ways. The first is taking the ratio between the highest and the secondary correlation peak, OpenPIV refers to this method as 'Peak to Peak'. The second method is taking the ratio between the highest peak and the root mean square, this is referred to as 'Peak to Mean'.

In addition to the SNR, this research removed all 'outliers' in the displacement values, ignored the interpolation function of OpenPIV and included a 'hit' boundary for each window. 'Outliers' are defined as all values outside of a two times standard deviation limit, these values are removed from the calculation. The limit is set at two standard deviations in order to ensure enough data points and simultaneously remove extreme outliers. In order to compute a homogeneous vector field, OpenPIV uses an interpolation function to replace missing values. This homogeneity is desirable when the conventional velocity-area method is used. However, in this research the function is ignored since a homogeneous result is not required and because it generates a higher average uncertainty. The last addition excludes all cells that do not produce a valid displacement value, referred to as a 'hit', for at least half of the images. Although this 50 percent boundary is arbitrary it is included in order to exclude velocities based on limited data. (see the GitHub repository for the complete LSPIV script [75]).

What remains is to specify several input characteristics, operational methods and parameters, i.e. the optimal video editing, video length, window size, overlap, signal to noise method and signal to noise threshold value. Altering these operations and assigned values does result in different configurations, each influencing the outcome and therewith the performance of LSPIV.

3.2.3. Validation of the LSPIV Results

In order to assess the influence and accuracy of the different configurations and inputs, the obtained results are compared to each other and to flow velocity measurements performed with a current meter. Ideally, the different configurations and inputs would be numerous and compared in all possible arrangements until an optimum is found. However, the LSPIV scripts used in this research processes 16 images per minute resulting in an average processing time of 19 minutes per configuration (see Github repository [75]). Since running all possible arrangements in a reasonable time-span would take much (unavailable) computational power, several classifications are made.

The classes are based on the general workflow described above. For each step, or operation, in the workflow several configurations are considered and processed. Afterwards the best performing

configuration for a certain operation is determined and used in the configurations of the consecutive operation. Each configuration is arbitrarily chosen and ran one single time. The parameter set of the configuration should ideally be determined by optimization instead of arbitrarily chosen, however, due to the lack of computational power and time the configurations are chosen manually herewith considering as many aspects as possible. In doing so, the configurations, although not optimized, show the general influence of the adjustment. By knowing the influences an 'optimal' configuration can be established and therewith the first research question can be answered.

Each operation is assessed by the following criteria:

- Number of images (Images)
- Number of windows per image (Cells)
- Percentage of windows containing a at least one determined velocity vector, or 'hit', (With hits [%])
- Average number of determined velocities for all windows with at least one hit (Avg. nr. of hits [%])
- Percentage of cells with a determined velocity vector for more than half of the images [Cells > N/2 [%]]
- Average flow velocity in metres per second (\bar{v})
- Average standard deviation of the velocity (calculated for each window in each image and subsequently averaged) (STDV)
- The Mean Averaged Deviation (MAD) between the Current Meter (CM) measurements and the determined flow velocity in the nearest window (the deviation is determined for each separate CM measurement in every image, afterwards averaged for all images and subsequently averaged for all CM measurements) (MAD)

3.3. Modelling Bathymetry

This section describes the steps undertaken to establish a bathymetric chart by using a combination of different techniques and measurement devices. First, the bathymetry is divided in the 'dry' river bathymetry (i.e. the floodplain) and the 'wet' river bathymetry (i.e. the submerged part of the bathymetry at the time of measuring). The dry river bathymetry is mapped using photogrammetry and the wet river is mapped using an ADCP. Both photogrammetry and the ADCP are combined with RTK GPS for an exact determination of the measurement locations (see Chapter 2 for a detailed description of the measurement devices). The collection and processing of this data is described in this section and therewith providing a workflow focused on answering the second research question:

II How can a bathymetric chart of a river be established based on photogrammetry and sonar data?

Photogrammetry is a technique of extracting three dimensional information from images. These images are collected with a drone while flying over the floodplain. Before collecting, Ground Control Points are distributed over the floodplain. These GCPs are similar to the GCPs used in the river surface videos (Figure 3.2) and the exact centre of the GCPs is likewise measured with RTK GPS. The GCPs are used for calibration purposes, to correct distortions and reference the data to a coordinate system [57]. In order to cover the whole floodplain systematically the drone follows a certain pattern, this pattern is flown twice where the second pattern is slightly rotated (Figure 3.4 I). This rotation is applied to mitigate systematic errors in the processing like the 'bowling effect' [68]. This effect lifts the sides of a map slightly whereas the middle lowers somewhat, hereby creating a concave shape or 'bowl'. The effect is caused by the convex shape of the camera lens and has a positive correlation with the area size. Another method to reduce systematic errors is flying with an off-nadir installed camera [68], this means the camera is not directed straight down but it has a slight tilt (Figure 3.4 III). When flying, the time interval between the images and the speed of the drone determine the overlap of the images. The flight pattern of the drone (Figure 3.4 I) results in image 'strips' along the straight lines. The overlap with the consecutive image in a strip is called frontal overlap and should be around 60 percent [57]. The overlap with the adjacent strip, referred to as side overlap, should be approximately 30 percent [57] (Figure 3.4 II). The overlap is needed in order to merge the images into one map based on recognizable features.

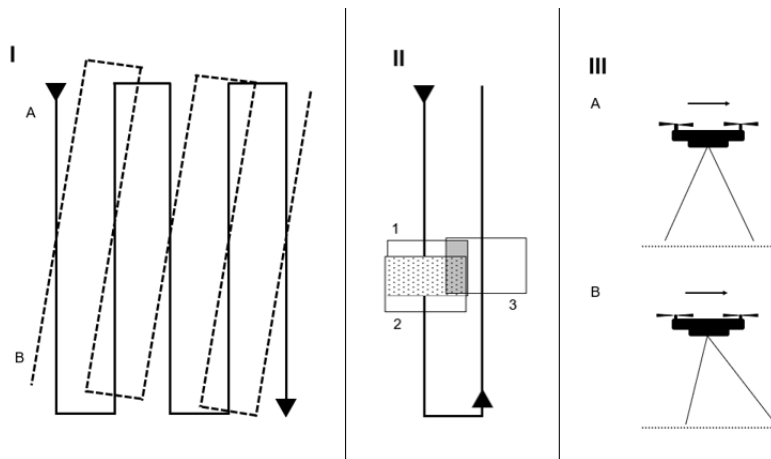


Figure 3.4: I: A represents the first flight pattern. B represents the slightly rotated second flight pattern (image idea is based on the WebODM tutorial [57]). II: The dotted area between image 1 and 2 is the frontal overlap. The gray area between image 1 and 3 represents the side overlap. III: A shows a drone with a nadir viewing camera. B shows a drone with an off-nadir installed camera, in this case a 80 degrees forward facing angle.

The images are processed with WebODM to obtain a dense point cloud of the 'dry' river. WebODM is an open source application for drone image processing provided by Open Drone Map [57]. "It provides a web interface to ODM with visualization, storage and data analysis functionality" [57]. ODM is the underlying image processing software. Ground Control Points have to be included manually in WebODM, the GCPs have to be searched for in various images and linked to that particular image with the pixel number belonging to the centre of the GCP.

The wet river bathymetry is based on Acoustic Doppler Current Meter (ADCP) measurements and RTK positioning (see Chapter 2 for a detailed description of these measurement devices). The ADCP measures water depth and flow velocity over the depth based on transmitting and receiving acoustic pulses. The location of these measurements is recorded with RTK GPS. This results in a point cloud with the attributes latitude, longitude, height and water depth to each point. Extracting the depth from the water level gives the elevation level of the wet river bed. Finally, the wet and dry river bathymetry point clouds are merged in CloudCompare. CloudCompare is a 3D point cloud and mesh processing software and, like WebODM, open source [13].

3.3.1. Dry River Bathymetry

The dry river bathymetry (the floodplain at time of measuring) is mapped with photogrammetry using a drone (DJI Phantom 4) and GCPS. The drone did fly two patterns as depicted in Figure 3.4 I, the dimension of both patterns was 577 metres in length and 504 metres in width. The used flight planning software is Pix4DCapture since it has the ability to change the camera angle. The drone flew at an altitude of 90 metres, just high enough to avoid a hill in the south-east corner of the flight pattern. During each flight the drone took 265 pictures (530 in total). The frontal overlap was 80 percent and the side overlap 72 percent, this is enough to create a dense point cloud [57]. The camera angle during the flight was 80 degrees forward facing (10 degrees off-nadir). 17 Ground Control Points were distributed over the floodplain (Figure 3.5). The GCP positions were measured with RTK GPS, the base was up for two and a half hours before the first GCP location was measured with the rover. There are no GCPS located at the left bank of the river do to the topography, the bank was steep and covered with shrubs.

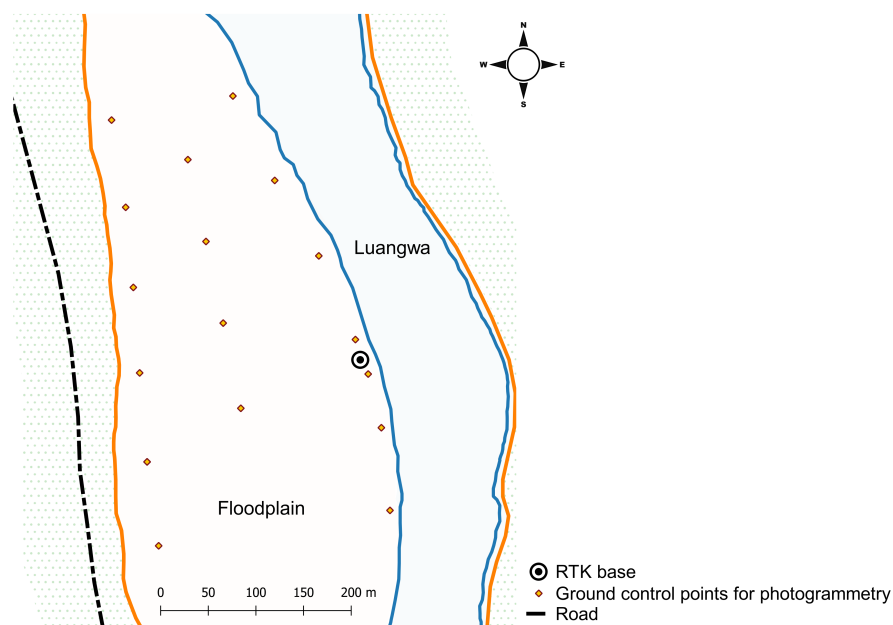


Figure 3.5: The 17 GCPS are evenly distributed over the floodplain and the RTK base station has a clear line of sight with all GCPS. Placing GCPS on the left-bank was not possible due to the geography.

3.3.2. Wet River Bathymetry

The wet river bathymetry (the actual river at time of measuring) is mapped with an ADCP and RTK GPS. The ADCP is used to measure the depth while the RTK GPS records the position. The on board GPS of the ADCP is not used because of the lesser accuracy. The RTK GPS GNSS receiver of the rover is mounted exactly on top of the ADCP (where it sends the vertical beam) while the ADCP is connected to a wooden canoe (Figure B.1). Both the ADCP and the GPS take measurements with a one second interval while the canoe manoeuvres in a zig-zag way over the river (Figure 3.6). The ADCP is connected to a laptop running WinriverII. WinriverII is a real-time discharge data collection program designed for this kind of ADCP. The rover is connected to a smartphone that uses the application SW Maps to log the location points. After every crossing, both the ADCP and the RTK measurements are

stopped, saved and started again. In this way the ADCP measurements can not only be used as depth but also as discharge measurements. Likewise, the GPS required this procedure since SW maps has a limit of measurement points that it can export for each string. The ADCP crossed the river 21 times in which it took 3102 depth measurements. Of the 21 crossings, 12 are more or less perpendicular to the mean flow direction, this is favourable for discharge measurements [73]. Furthermore, the canoe is manoeuvred along both river banks in order to take measurements for interpolation purposes. Since the river was very shallow for several meters from the western bank (especially in the north) the canoe could not exactly follow the river bank (Figure 3.6). In order to mitigate this problem, a cart is pulled along the waterline with the rover on top (Figure B.2). The total amount of measurements taken along the banks, both with the canoe and the car is 2062. This results in a total of 5166 measurement points from which the wet river bathymetry should be constructed.

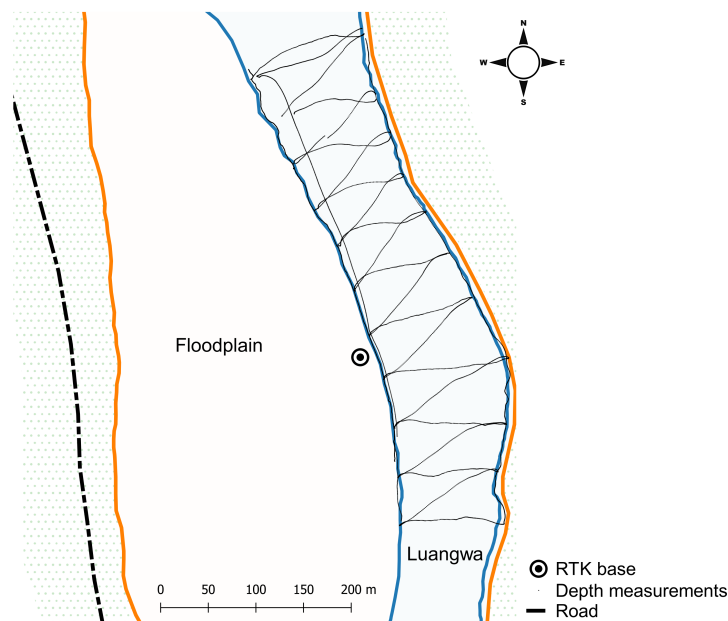


Figure 3.6: 3102 depth measurements are taken in a zig-zag pattern over the river. Another 651 depth measurements are done along the eastern bank, 515 along the western bank and 898 exactly along the waterline at the western bank.

3.3.3. Processing Bathymetric Data

Creating an accurate bathymetric chart from drone images and depth measurements requires several processing steps. First, the images have to be converted to a dense point cloud before they can be merged with the ADCP/RTK point cloud. Second, the depth measurements should be modified in order to get the actual height component. This section deals first with the dry river bathymetry then with the wet river bathymetry and eventually with merging and interpolating the point clouds into a final bathymetric chart.

The images are processed with WebODM as described in section 3.3. After uploading the images each GCP is linked to six pictures that depict the GCP, three of each flight pattern (102 in total). With the GCP list enclosed the process was started with default settings. After the first run WebODM produces, besides a point cloud, a calibration file. This file can be uploaded again for a second run which is more efficient [57]. The dense point cloud produced by WebODM consisted of 53.8×10^6 points (Figure 3.7). To check for the bowling effect, the sample module of the Rasterio library in python is used. The module sampled the closest point to every coordinate in the RTK track along the waterline (Figure 3.7). When the points are plotted against the RTK coordinates a clear 'bowling effect' is apparent (Figure 3.8 Perspective). In order to minimise the effect, WebODM provides the possibility to change the camera model to Brown-Conrady instead of the default perspective model [62]. As can be seen in Figure 3.8 the Brown-Conrady model turns the concave shape of the Perspective model into a convex shape, in other words it overcompensates for the bowling effect. Other calibrations methods are tried but non of them was satisfactory (Figure B.4).

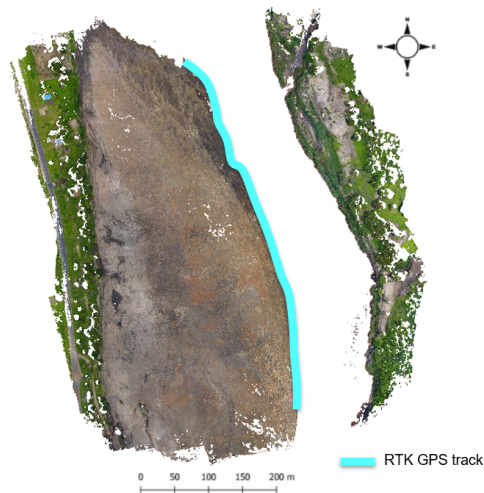


Figure 3.7: Dense point cloud produced by WebODM with GCP calibration. The cyan line represents the track followed with a trolley with the RTK GPS rover on top.

Therefore a somewhat less subtle, however, practical approach is used to 'straighten' the dry river bathymetry point cloud. A first order polynomial is fitted through the RTK GPS track and second order polynomials are fitted through the points sampled with Rasterio from the point clouds calibrated with different methods (i.e. Perspective, Brown-Conrady, Brown-Conrady and Perspective combined and Brown-Conrady without calibration file, Figure B.5). A second order polynomial is used since the convex shape of the point cloud is caused by the shape of the lens, which is a second order polynomial [19]. Subsequently the average absolute error between the first and the second order polynomials is calculated. Table B.1 shows that the Perspective model yields the lowest absolute error, therefore this point cloud is chosen to proceed with. The point cloud is divided over the latitude (north-south direction) in 1500 sections of equal size (0.52 metres per section). All points within one section are considered to have the same deviation from the true height, i.e. the more northern and southern sections have a positive deviation where the centre sections will have a negative deviation. The deviation per section is determined by the difference between the Perspective second order polynomial and the RTK GPS polynomial since this is the only 'true' height available. All points within each section are corrected with this deviation. This 'straightens' the point cloud only in a latitudinal direction. Straightening in the longitudinal direction could be done in a similar way, however, a line in east-west direction is not measured with RTK GPS during the fieldwork and therefore there is no correction data. Nevertheless, the latitudinal direction is most important since it is virtually the direction of flow. The result is a point cloud constructed from images that is corrected for lens distortion.

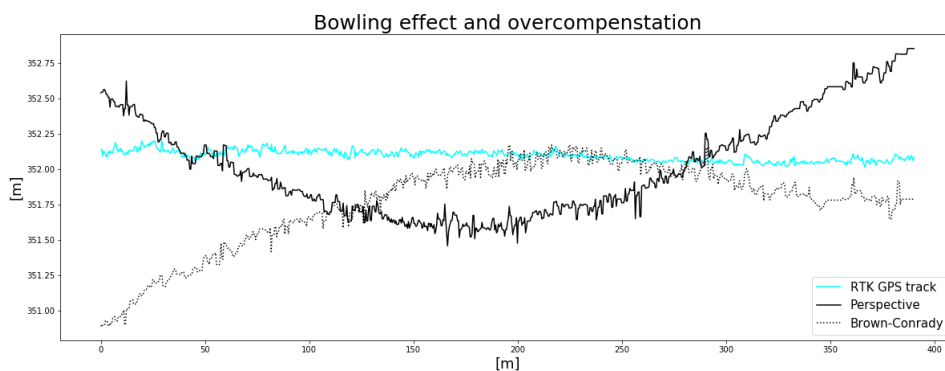


Figure 3.8: The WebODM perspective model point cloud shows a clear bowling effect compared to the RTK GPS track. The Brown Conrady model seems to overcompensate.

The wet river bathymetry point cloud is processed as follows. Each measurement point taken on the river consists of the attributes depth (measured with the ADCP), latitude, longitude and height (measured with the RTK GPS). Since the RTK GPS has the highest uncertainty in the vertical, the height measurements are not considered but the 1500 sections based on the waterline polynomial of the eastern bank (Figure B.3) are used. All points in a certain section get the height as determined by the RTK GPS track polynomial. Since the sections are 0.52 metres wide with a slope of 0.0002298 this approximation seems acceptable. The depth measurement is subtracted from the water height and combined with the longitudinal and latitudinal coordinates. Thereafter, the point cloud is volumized using CloudCompare without the waterline, east bank and west bank tracks (Figure B.6 A). Including these points would result in gradually decreasing depth along the waterlines since CloudCompare interpolation linearly. The three tracks were added afterwards and volumized subsequently (Figure B.6 B and C).

When both point clouds are constructed and corrected accordingly they are merged (Figure B.7 A) whereafter another linear interpolated 2.5D volume is computed (Figure B.7 B). In the north east corner of the point cloud there is a small tributary which was dry during the time of measurement. To make sure there is no water flowing out of the model at higher discharges, the tributary is closed by cutting it out of the point cloud and volumizing it again (Figure B.7C). In order to use the point cloud in a model, the area should be extended both downstream and upstream. The extensions mitigate uncertainties in the assigned boundary conditions. First the northern and southern sides (upstream and downstream) are cut perpendicular to the flow direction (Figure B.8 A). Then a small selection of 1200 coordinates over the complete width on each side is taken. This small stretch is reproduced every 36.85 metres in the direction of flow (or opposite for the extension to the north), this means the longitudinal and latitudinal values are shifted slightly and the height is subtracted or added with the corresponding slope (Figure B.8 B). The point cloud is both upstream and downstream extended with 118 stretches, corresponding to 4348 metres, which is significantly more than half of the adaptation length (2.1 kilometres, Equation B.4). Ideally the point cloud should be extended with the full adaptation length of the river (8.0 kilometres, Equation B.1) both upstream and downstream but a point cloud of this size would slow down the model significantly. After volumizing the model for the last time the final result is a point cloud containing 4.76×10^6 coordinates representing approximately 9.2 kilometres of the Luangwa river.

By establishing this bathymetric chart based on photogrammetry and sonar data an answer is given to the second research question, however, without any validation of the charts accuracy. Assessing this accuracy is possible against similar bathymetric charts of this area at the time of measurement but, unfortunately, these charts do simply not exist. However, the precision of the longitudinal and latitudinal coordinates can be assessed by visually checking the chart which will indicate outliers. The precision of the height component can be assessed by plotting its distribution which will again indicate outliers and discrepancies in the data. Furthermore, the accuracy will influence the ability of the discharge model to simulate the river discharge correctly and therefore it is probable that the point cloud is merely accurate when the discharge model performs well.

3.4. The Discharge Model

In this fourth and final section of the chapter, the methodology regarding the creation of the 3D discharge model is described. The bathymetric chart is merged with all other measurements to create the model and therefore all previously presented measurements, methods and corresponding outcomes can be regarded as direct or indirect input in this final model. In short, this section describes the model input with the corresponding requirements, the calibration steps and the expected model output and therewith describing a workflow able to answer the following two research questions:

III How can surface flow velocity estimations be implemented in a 3D discharge model?

IIII How does the model perform compared to conventional measurements?

The used model is Delft3D D-flow Flexible Mesh (D-Flow FM) version 2020.03 (beta version) created by Deltares. D-Flow FM is a hydrodynamic simulation program and part of the Delft3D Flexible Mesh

Suite. The model is chosen for its ability to make 3D river computations using unstructured curvilinear grids with sigma layers in the vertical. Please note that the 3D modelling is a beta functionality at the time of modelling and writing [16]. A basic model needs a bathymetric chart, grid and boundary conditions to run with default settings. Running means that the 3D non-linear shallow water equations are solved between each grid cell. These equations are derived from the three dimensional Navier-Stokes equations for in-compressible free surface flow [16].

3.4.1. Model Input

The external model input is comprised of both the river bathymetry and an unstructured curvilinear grid. The bathymetry is a point cloud created with photogrammetry and depth measurements as described in section 3.3.3 and depicted in Figure B.8. The unstructured grid is constructed with RGFRID based on land boundaries. Land boundaries indicate the outer river banks in between which the grid should be constructed. Land boundaries are drawn in Qgis along the complete bathymetric chart whereafter the land boundaries are imported in RGFRID. RGFRID is a generator for structured and unstructured grids suited for Delft3D FM [17]. Within RGFRID an unstructured curvilinear rectangular grid is constructed (Figure 3.10). The cell width of the base grid is 6.9 metres, however, at the 'wet' part of the model the grid cells are split (Figure C.2) and therefore 3.45 metres wide, smaller is possible but increases the run time significantly. The length of the grid cells is smallest at the observation points, with a length of 7.13 metres, and extends towards the boundaries (Figure 3.10). The complete grid has a length of 9.2 kilometres. Eventually, the bathymetry and the grid are combined with the interpolate set function. The interpolation technique is triangular and based on location. Since the land boundaries are drawn along the bathymetric chart, both the bathymetry and the grid have the same coordinate system, WGS84/UTM36S, and therefore the same location. All measurements done to gather the right input data are schematically depicted in Figure 3.9.

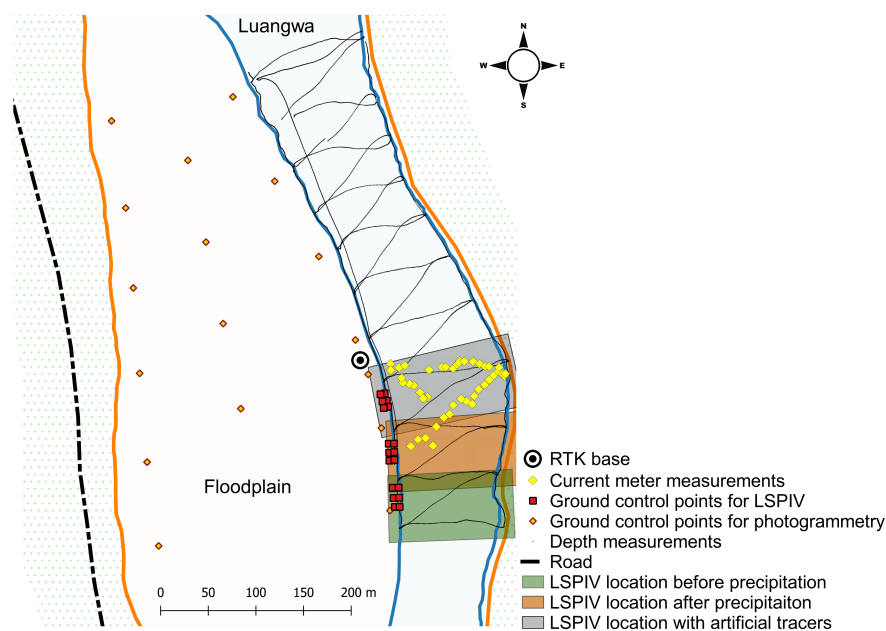


Figure 3.9: Overview of all measurements conducted during fieldwork.

The upstream boundary condition is defined by discharge. The discharge is, for each simulation, continuous over time and ranges from 5 to 3000 m³/s. The maximum discharge of 3000 m³/s is based on a WARMA discharge dataset collected several kilometres upstream of the research area as presented in [31]. The downstream boundary condition is defined by the water level. Each discharge has a corresponding water level which is determined with reference to the backwater curve. For each discharge the downstream water level is determined by iteration until the backwater curve did not exceed 3cm centimetres in total. Regarding the distance between the downstream boundary and the observation points of 4400 metres, this seems acceptable.

The majority of the model settings are kept on default except for the following. The model is transformed to 3D by dividing the single vertical layer into 10 sigma layers. Sigma layers represent a certain percentage of the depth and can therefore vary in thickness at different locations (see section 2.4). The Sigma layers in the model all represent 10 percent of the depth. The coordinate system is set to WGS84/UTM36S. The total run time is set at 12 hours, this proved to be sufficient to reach a practically steady state. The time interval for external forcing updates is set at 5 minutes, however the external forcings are fixed over time. The initial computational time step is set at 1 second with a maximum of 30 seconds. The exact duration of each time step is automatically computed by the computational kernel regarding the maximum tolerable Courant number [16]. The maximum Courant number is set at 0.7 (default), this is advised since D-Flow FM uses an explicit advection scheme regarding the time step size from the Courant criterium [16]. Furthermore, three observational cross sections and 20 observation points are included in order to monitor the output. Five points are placed strategically to observe water level, five to observe the width of the river and ten to compare the modelled with the measured surface flow velocity (Figure 3.10).

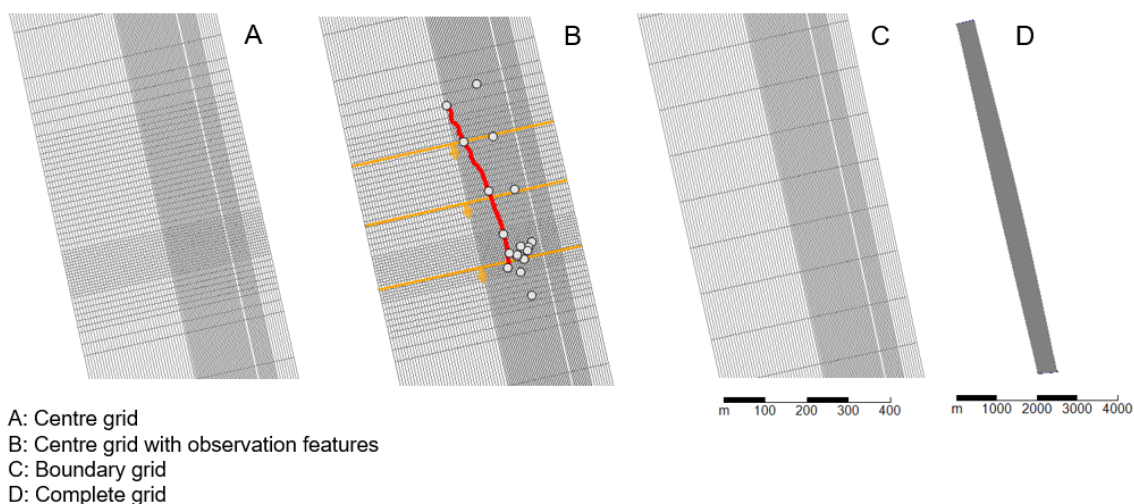


Figure 3.10: The grid made with RGFGRID for a discharge ranging from 5 - 275 m³/s. The cell size is smallest at the observation points in the centre of the grid and increases towards the boundaries.

3.4.2. Model Calibration

Since measuring the exact bed roughness of the research area independent from the model is a difficult task, the bed roughness is acquired by calibration. Through adjusting the bed roughness, represented by Manning's friction coefficient, differences between model results and measured values are minimised. Since the discharge was constant during the fieldwork, the roughness is calibrated with only one discharge with corresponding water levels and surface flow velocities. The Discharge is measured with an ADCP as explained in section 3.3.2 and depicted in Figure 3.9. The 21 discharge measurements yield an average of 191 m³/s with a standard deviation of 7.45 m³/s. Figure C.1 shows a cross section as depicted in the Winriver II software. The water level at the research area is defined by the RTK waterline track polynomial (Figure B.3). The surface flow velocities used for the calibration are determined using both LSPIV, as described in section 3.2.2 and depicted in Figure 4.9, and current meter velocity measurements. Due to limited computational power, the grid cells in the model are larger than the windows used by LSPIV. Therefore, a selection of windows is made. Five windows where both LSPIV and the current meter recorded a velocity are used as well as four windows furthest advanced in the four cardinal directions plus the window of which the velocity is based on the highest number of displacement values calculated by OpenPIV. As a consequence there are only two observation points located in the same grid cell (Figure 3.11). This method of using the LSPIV velocities of certain windows for calibration purposes in combination with the corresponding results provides an answer to the third research question. The downstream boundary condition is set, after several iterations, at 350.98 metres above mean sea level, representing a water depth of 2.05 metres and a backwater curve of less than one centimetre.

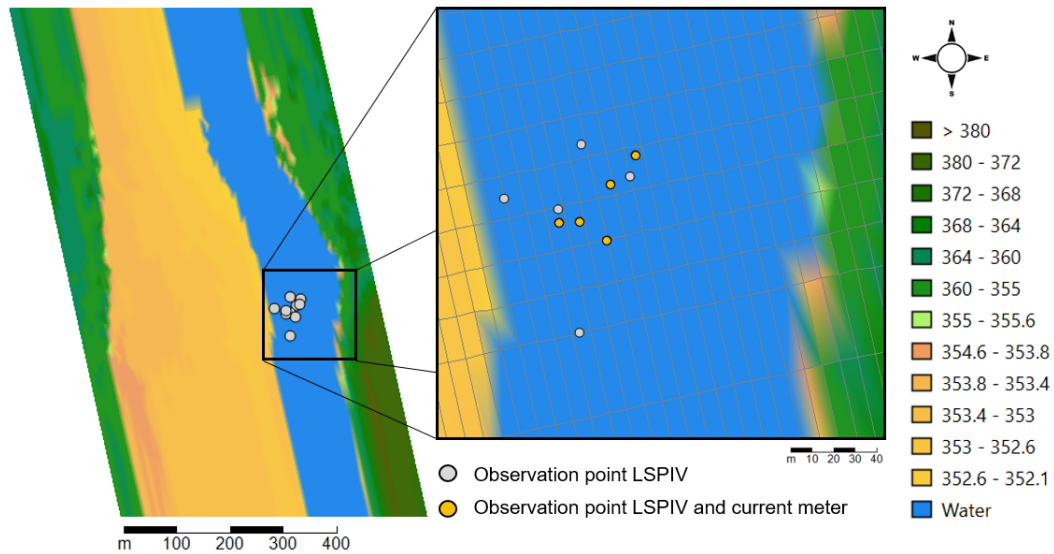


Figure 3.11: Velocity observation locations.

3.4.3. Model Output

When the optimal roughness is established all parameters are defined and an 'optimal' model is created. However, this is only the case for one discharge and does not guarantee any predictive power.

Unfortunately, in this research there is only data collected during a constant river discharge of 191 m³/s. Therefore, the predictive power of the model cannot be validated with other discharges. However, running the model with different discharges yields a stage-discharge relationship which can be compared to two already created stage-discharge relationships, one by I. Abas as part of his master thesis [31] and one by WARMA. Both relationships are established for a cross section only several kilometres upstream of the research area but the cross-sections of I. Abas and the WARMA gauging station are likely to be different from the arbitrary cross section chosen in the model. However, the order of magnitude should be similar and therefore this comparison can (partly) answer the fourth research question. Besides a stage-discharge relationship a width-discharge relationship is constructed.

In order to construct these relationships, both boundary conditions need to be adjusted for each simulation. The discharge is ranging from 5 to 3000 m³/s with steps of 25 or 100 m³/s but the downstream corresponding water levels are not known yet. This is determined by minimizing the backwater curve through iteration for 20 discharges. The water levels are plotted against the discharges at logarithmic scales (Figure 3.12).

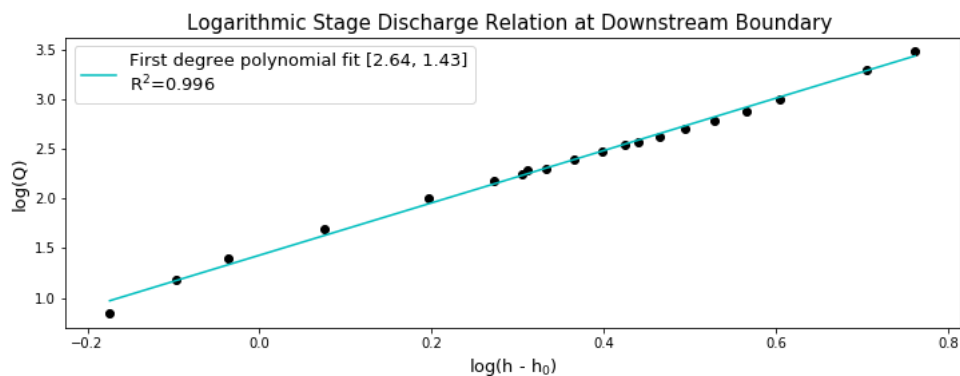


Figure 3.12: Stage and discharge plotted on a logarithmic scale in order to determine the stage-discharge relationship at the downstream boundary condition.

According to Herschy [66] the downstream stage-discharge relation can be described by the general form of the equation:

$$Q = a(h - h_0)^b \quad (3.1)$$

Where a and b are empirically determined coefficients that are determined by the slope, roughness and flow [8]. A first degree regression line gives: $a = 26.9$ and $b = 2.64$. Where $h - h_0$ ranges from 0 to 8 metres. Figure 3.13 shows the stage-discharge relationship at the downstream boundary. Eventually the model has been ran, with the calibrated bed roughness coefficient, for 67 discharges with corresponding downstream boundary water levels based on the stage-discharge relation (Figure 3.13 resulting in a stage-discharge relationship at the research area.

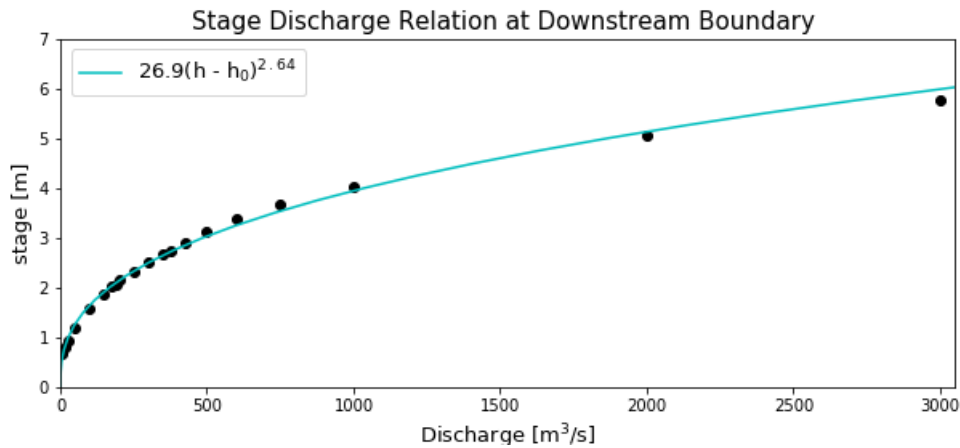
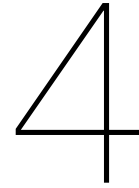


Figure 3.13: The stage-discharge relationship at the downstream boundary condition with which the water level for 67 discharges is determined.



Results and discussion

In the following chapter, the results of this research will be presented and discussed. All results are introduced in the same order as Chapter 3, i.e., starting with surface flow velocities computed with LSPIV then the bathymetric chart and finally the model results. The results presented in each section follow the order of the workflow and will be used to answer the corresponding research questions.

4.1. Surface Flow Velocity

The results in this section originate from the workflow as described in section 3.2.2 and regard LSPIV as a surface flow velocity measurement technique for medium-sized rivers. All results are obtained with OpenPIV. Based on the presented results an answer will be formulated to the following research question:

I How to utilize Large-Scale Particle Image Velocimetry to obtain surface flow velocity estimations intended for the use in a 3D discharge model?

Since the acquired results regarding LSPIV are numerous, only a selection is presented in this chapter. The selection is based on the explanatory power of the results with respect to the research question or remarkable character of the results. All remaining results can be found in Appendix A.

As the research question suggests, LSPIV can be utilized in various ways. This difference in utilization stems from alterations made in the operations that together compose LSPIV. To better understand these alterations, the term LSPIV should not be interpreted as a measurement technique consisting of one sole operation but as an umbrella term for several consecutive operations that together compose LSPIV. So in essence the utilization is similar but the process is altered. The different modifications are mentioned in section 3.2.3 together with the validation methods and criteria the different configurations are assessed on.

As mentioned in section 3.2.1, videos are recorded under three different circumstances, i.e., before precipitation, after precipitation and while seeding artificial tracers. For only one of the three videos an optimal configuration is determined, the performance of this configuration is afterwards assessed through the remaining videos. During pre-processing, the video recorded after the precipitation event appeared to be most promising, likely due to the higher tracer density, therefore this video is selected for the assessment. The video has a total length of 31 seconds, is recorded at 30 frames per second with a resolution of 2704 x 1520 pixels and a pixel per metre ratio of 21.62.

The average velocity measured by the current meter is 1.04 m/s with a standard deviation of 0.34 m/s based on 50 measurements (see section 3.2.1). However, only eight measurements are located in the observation area of the selected video (Figure 3.3). Therefore the MAD score is based on eight deviations per image. The average velocity of the eight CM measurements is 1.06 m/s with a standard deviation of 0.35 m/s. Please note that the CM measurements are conducted from a wooden canoe kept as steady as possible in the current, therefore the CM measurements should be interpreted as

indicative instead of being treated as ground truth velocities.

4.1.1. Input Editing

The statistical assessment of different video editing methods is provided in Table 4.1. OS refers to the Original and Stabilized video. Afterwards the video is gradually edited by converting it to Gray-scale (OSG), adjusting the Gamma value (OSGG, gamma = 0.5) and changing the Contrast values (OSGGC, gamma = 0.7, alpha1 = 3.0, alpha2 = 0.0, beta = -150, where alpha controls the brightness and beta the contrast). The gamma value of the OSGGC video is brought back from 0.5 to 0.7 since the video became too darkened due to the higher alpha1 value. All videos have a length of 5 seconds (150 images, except assessment 2) and contain 1537 windows (except assessment 4).

Edit	Images	Cells	With hits [%]	Avg. nr. of hits [%]	Cells > N/2 [%]	\bar{v}	$\overline{\text{STDV}}$	MAD
OS	150	1537	53	40	20	0.71	0.238	0.337
OSG	150	1537	52	42	22	0.69	0.247	0.336
OSGG	150	1537	54	44	23	0.71	0.256	0.326
OSGGC	150	1537	54	42	22	0.70	0.245	0.313

Table 4.1: Statistics of LSPIV results based on different video editing methods.

All editing methods result in an estimated velocity in 50%plus of the windows with a systematically underestimated average velocity of 0.7 m/s instead of 1.06 m/s (Table 4.1). In general, Table 4.1 illustrates that editing this particular video does not result in significant improvements in LSPIV performance. This does not necessarily mean that video editing can be excluded from the LSPIV process since the table only shows results of four modified parameters in one particular video. Please note that the effect of the stabilization function is not shown here since all four videos are stabilized. However, the five seconds are selected from the original video (31s) with regard to vibrations and the amount of tracers. Since the most rigorously edited video (OSGGC) results in the lowest average Standard Deviation (STDV) and Mean Average Deviation (MAD), this video is continued with.

4.1.2. Input Length

Table 4.2 shows the statistics of videos with a length varying from 5 to 20 seconds. It should be taken into account that the total processing time changes significantly between the videos due to the constant processing rate of 16 images per minute.

Length	Images	Cells	With hits [%]	Avg. nr. of hits [%]	Cells > N/2 [%]	\bar{v}	$\overline{\text{STDV}}$	MAD
5	150	1537	54	42	22	0.70	0.245	0.313
10	300	1537	64	36	22	0.72	0.248	0.300
15	450	1537	70	34	21	0.71	0.251	0.350
20	600	1537	74	32	19	0.73	0.265	0.347

Table 4.2: Statistics of LSPIV results based on video length.

Table 4.2 shows a positive correlation between the percentage of cells with at least one hit (With hits [%]) and the length of the video. This is to be expected as each extra image can only add to the amount of windows with a determined velocity. The average number of hits shows an opposite correlation, this is likely caused by the selected start time of each video (i.e. the start time is manually picked based on the amount of tracers and vibrations in the video). In other words, it is most likely to have more vibrations and less tracers in some parts of the 20 second video than in the 5 second video. Since Table 4.2 presents the result as percentage of the total, the score of the shorter videos suggests a better performance. The videos with a length of 5 and 10 seconds have very similar results but, even though the 5 second video has a shorter processing time, it is decided to proceed with the 10 second video since the performance is better on the MAD score, the average velocity is slightly higher and the results are based on more data.

Figure 4.1 visualizes the vector fields produced by LSPIV for the 'best' performing configurations regarding the editing and length of the videos. It shows that, besides the statistics, also the spatial distribution of the velocities is very similar. Furthermore, the influence of ignoring the interpolation function is clearly visible as both plots show an incomplete and unevenly distributed vector field. Please note that the OSGGC vector field is also the 5 second vector field (see Appendix A for vector fields of all other configurations).

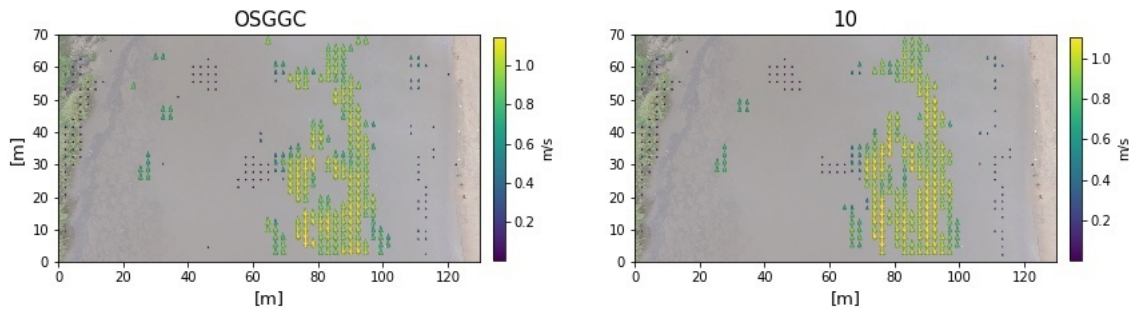


Figure 4.1: Vector fields produced with LSPIV based on different video editing methods and video length.

The only marginal effect due to editing and video length is also apparent in Figure 4.2. The upper plots in the figure visualize the Mean Average Deviation between the surface flow velocities determined by LSPIV and the current meter. All velocities include an error bar representing one standard deviation based on the computed velocities, between all frames, for the window and a number defining the amount of computed velocities the average is based on. Through the velocities a regression line is plotted represented by the red line. For a perfect accordance between both measurement techniques the regression line should follow the 1:1 (grey dotted) line. It must be noted that drawing conclusions based on a regression line which is fitted through only eight measurement points is not the aim, however, the regression line gives an quick visual indication of the relation between the two measurement techniques. The two lower plots visualize the horizontal (V_x) and vertical (V_y) displacement values that together determine the direction and velocity (the velocity vector) within each window.

Comparing the two upper plots in Figure 4.2 indicates a slightly better accordance between LSPIV and the current meter for the 10 second video, this is also indicated by Table 4.2. Furthermore, both plots clearly show the velocity underestimation and indicate one outlier with an LSPIV velocity close to zero. Since none of the eight measurements are located close to the bank (resulting in a lower velocity) it is likely that the outlier is caused by OpenPIV. Please note that the outlier is based on the smallest number of computed velocities (15 and 23 respectively).

Both of the lower plots indicate a velocity distribution ranging between 0.0 m/s and 1.2 m/s in the downstream direction (V_y) with a slight deflection to the left (V_x). This is in accordance with the interpretations and measurements done during the fieldwork, with a lower velocity at the banks and a higher velocity in the centre of the river. The velocities can largely be divided in two clouds, surrounding $V_y = 1.0$ m/s and $V_y = 0.0$ m/s. This corresponds with the vector fields in Figure 4.1 where the division between yellow and black vectors is apparent. The low flow velocities (black dots) are mostly located at the right bank where the river is quite shallow, however, there are several low flow velocities computed in the middle of the river. These low velocities in the middle of the stream appear to be errors within LSPIV since the water was flowing fastest in the centre section of the river according to the current meter measurements and visual observations during fieldwork. In general the distribution of the point cloud is in accordance with the measured and observed velocities, however, with a small discrepancy in the velocities close to 0.0 m/s.

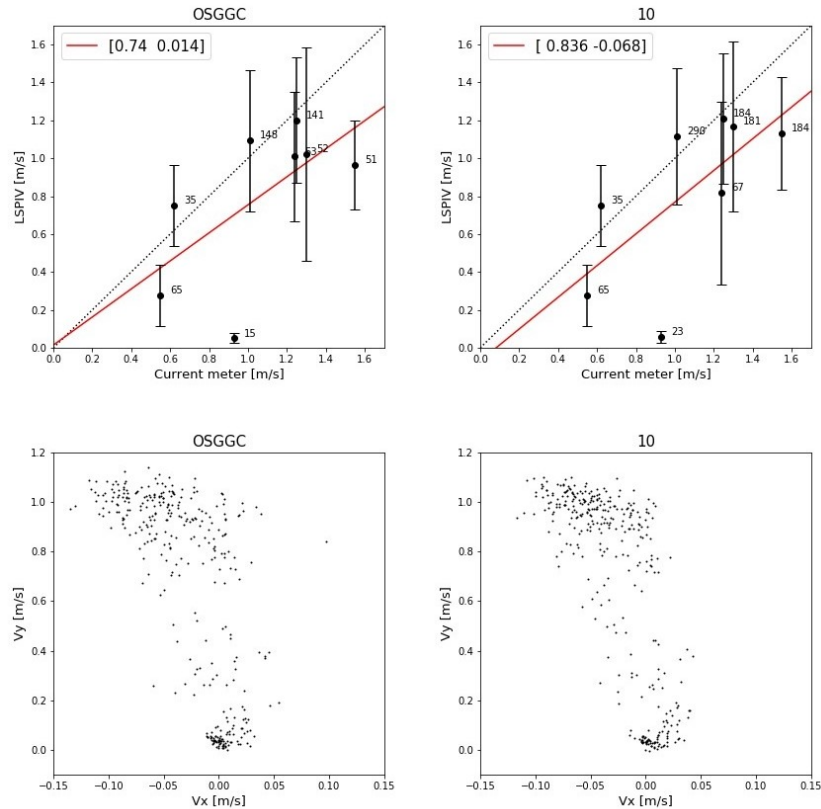


Figure 4.2: The upper plots show LSPIV measurements plotted against current meter measurements with error bars of one standard deviation based on the computed velocities, between all frames, for the window. The lower plots visualize the horizontal and vertical displacement value of each window computed by LSPIV.

4.1.3. Signal to Noise Ratio

The next step in LSPIV is determining the signal to noise ratio per window. OpenPIV provides two different cross-correlation functions for the task, i.e., P2P and P2M where P2P refers to the 'Peak to Peak' method and P2M to the 'Peak to Mean' method (section 3.2.2, Table 4.3). The Peak to Peak method is used in the prior assessments.

S2N	Images	Cells	With hits [%]	Avg. nr. of hits [%]	Cells > N/2 [%]	\bar{v}	$\overline{\text{STDV}}$	MAD
P2P	300	1537	64	36	22	0.72	0.248	0.300
P2M	300	1537	100	37	22	0.23	0.268	0.511

Table 4.3: Statistics of LSPIV results based on different signal to noise cross-correlation functions.

The Peak to Mean method seems to accept much more displacements (100% of the windows do have at least one determined velocity vector) compared to the Peak to Peak method, although the average number of hits is almost equal. The acceptance of more displacements seems to result in a much lower average velocity of 0.23 m/s which in turn leads to a higher MAD score. However, most interesting is the difference in spatial distribution of the velocities computed by both methods (Figure 4.3). The higher, and therefore more likely, velocities produced by P2M concentrate at the left bank whereas P2P computes most velocities on the right-hand side of the river. Although the P2P method is in general functioning better for this video, is not able to determine any flow velocities at the left bank while many tracers can be spotted there (visible in Figure 4.3 where the tracers form a black pattern). It seems as though a combination of both methods could possibly result in an improved outcome. Keep in mind that the vector field does only show the windows with a 50%plus hit score, therefore the vector field of the 'Peak to Mean' method is not 100% filled.

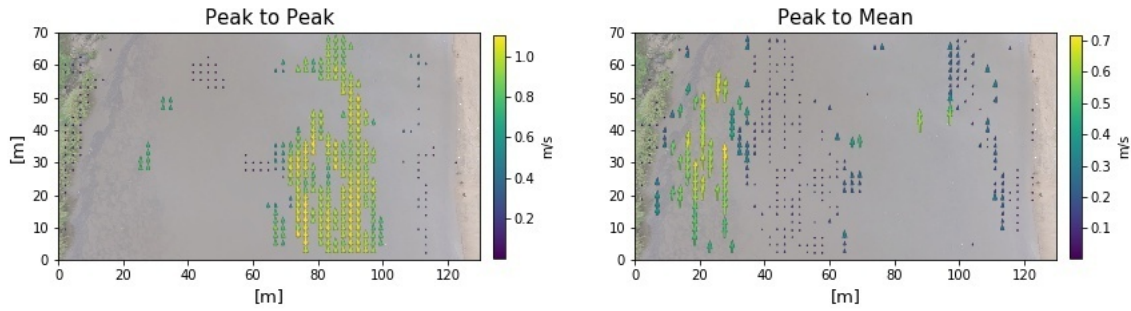


Figure 4.3: Vector fields showing the results obtained by LSPIV while using different methods to determine the signal to noise ratio.

The acceptance of lower values in the Peak to Mean method is also evident in both plots in Figure 4.4. Furthermore, the point cloud of the Peak to Mean method suggest an slight deflection to the right whereas the Peak to Peak method suggest the opposite. This is likely caused by the spatial distribution of the computed velocities. Since the geometry of the river tapers at the observed location (Figure 3.3) the flow direction at the river banks appears to be inwards creating an opposite deflection on each side. The Peak to Peak method is considered favourable for this video and is therefore used in the subsequent steps in the workflow.

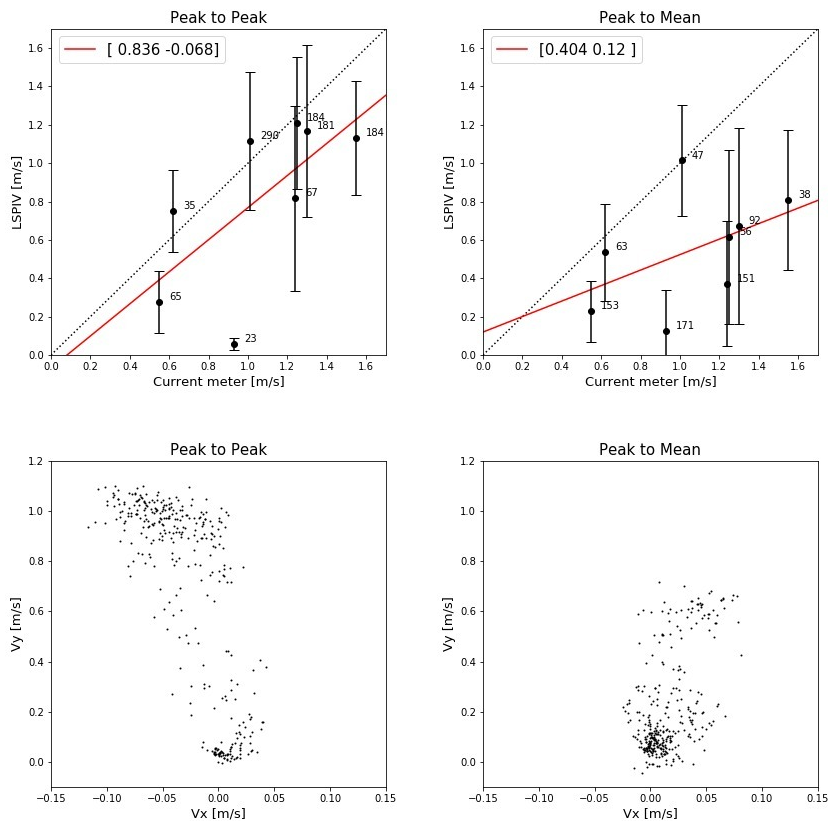


Figure 4.4: The upper plots show LSPIV measurements plotted against current meter measurements with error bars of one standard deviation based on . Both plots used a different method to determine the signal to noise ratio. The lower plots show the horizontal and vertical velocity vectors computed by LSPIV for both methods.

4.1.4. Window Size and Overlap

The next step is determining the window size and overlap. As mentioned in section 3.2.2, the window size should be chosen carefully regarding the velocity of the tracers, the density of the vector field and the processing time. The window size in the previous assessments was 100 x 100 pixels with an overlap of 50 pixels on each side producing 1537 windows per image (resolution: 2704 x 1520). For the assessment of the window size, the 100/50 configuration is changed to 50/25, 100/75 and 200/100 (Table 4.4), please note that the pixel per metre ratio is still 21.62.

W/O	Images	Cells	With hits [%]	Avg. nr. of hits [%]	Cells > N/2 [%]	\bar{v}	STDV	MAD
50/25	300	6313	93	39	29	0.17	0.235	0.639
100/50	300	1537	64	36	22	0.72	0.248	0.300
100/75	300	5985	64	36	22	0.72	0.245	0.276
200/100	300	364	26	51	13	1.09	0.285	0.236

Table 4.4: Statistics of LSPIV results based on different window sizes and overlap.

Decreasing the window size towards 50/25 results in a more dense vector field with a similar spatial distribution but with much more results in the centre of the river (Figure 4.5). These computed velocities are low, hence resulting in an average flow velocity of only 0.17 m/s (Table 4.4). The low flow velocities do not correspond to the measured and observed velocities and are therefore likely to be errors in LSPIV. Also, the centre part of the river contained far less tracers, so no predicted flow velocities are expected. Furthermore, downsizing to 50/25 results in 6313 windows per image and therefore a much longer processing time (about 4 times). Taken all of the above into account, decreasing the window size is rejected for this video. Up-scaling towards 200/100 leads to a shorter processing time and good results on both the average velocity and the MAD score, however, the statistics are only based on 47 windows (13% of 364) instead of 338 for the 100/50 ratio (22% of 1537) therefore the 200/100 ratio is rejected. Increasing the overlap towards 75 pixels does show very similar results compared to the 50 pixels overlap but requires a significantly longer processing time and therefore the 100/50 configuration is regarded to perform best.

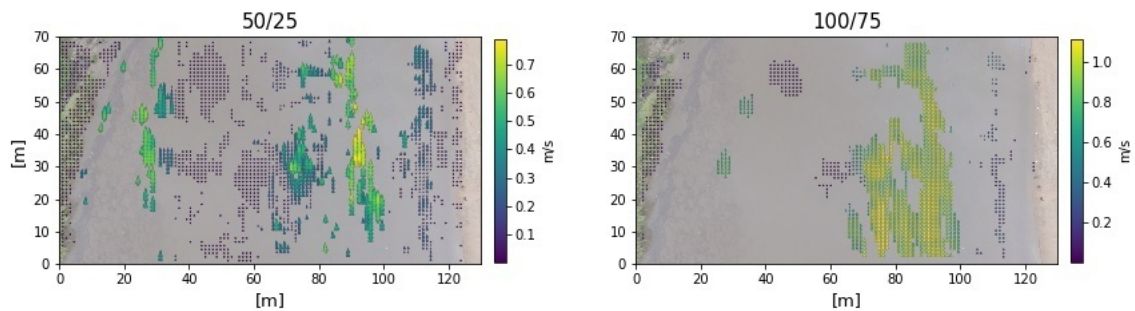


Figure 4.5: Vector fields produced by two LSPIV configurations with different window sizes and overlap.

Both 50/25 plots in Figure 4.6 show the underestimation of the flow velocities due to the down-scaled windows, based on both plots the reason for rejection is apparent. The 100/75 subplot containing the V_y and V_x velocities shows an even more obvious subdivision in two point clouds (i.e. $V_y = 1.0$ m/s and $V_y = 0.0$ m/s) due to the larger amount of windows.

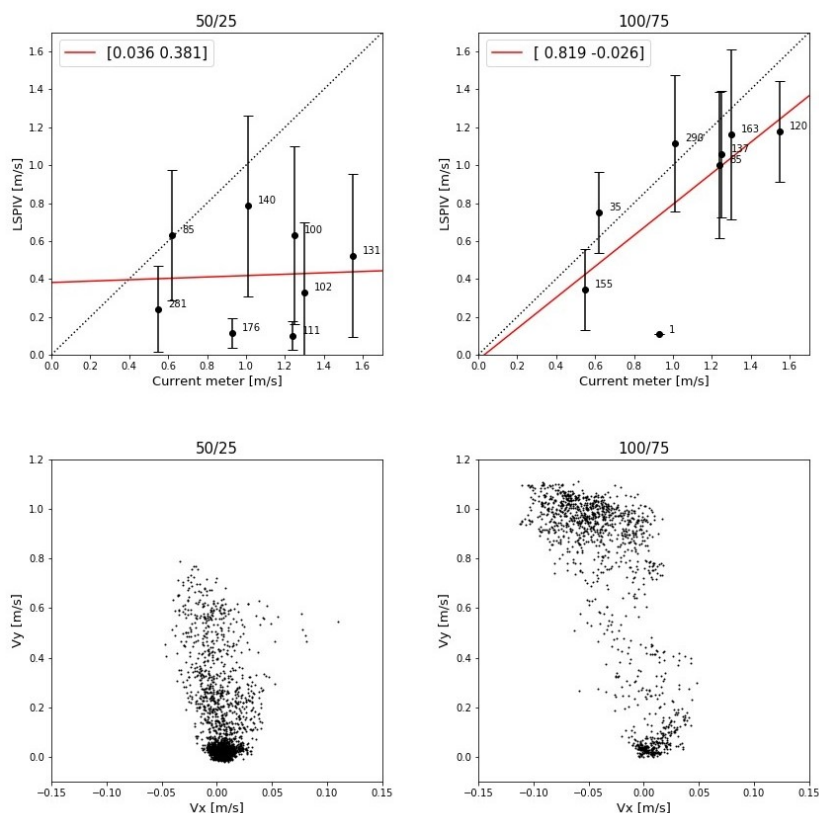


Figure 4.6: LSPIV statistics produced by two LSPIV configurations with different window sizes and overlap.

4.1.5. Signal to Noise Threshold

As determined from Table 4.3, the Peak to Peak cross-correlation function is the best method to determine the signal to noise ratio for this particular video. However, the method contains an arbitrary threshold (TH) for the maximum accepted noise which can influence the result drastically (see section 3.2.2). As stated in section 3.2.2, the Peak to Peak method uses the ratio between the highest peak and the second highest peak along the correlation plane. The highest peak is assumed to be the true displacement, the 'signal' whereas the other peaks represent the 'noise'. Therefore a threshold of 1.0 means that all velocities are accepted whereas a threshold of 2.0 means that the highest peak has to be, at least, twice the size of the second largest peak. In other words, for each window the velocity should be repeatedly computed with little deviation to be tolerated. If the computed values do deviate more than allowed by the threshold, the window will not get a value assigned. In the third assessment both thresholds were set at 1.5.

TH	Images	Cells	With hits [%]	Avg. nr. of hits [%]	Cells > N/2 [%]	\bar{v}	STD \bar{v}	MAD
1.0	300	1537	100	86	94	0.30	0.269	0.522
1.3	300	1537	87	53	49	0.43	0.251	0.399
1.5	300	1537	64	36	22	0.72	0.248	0.300
1.8	300	1537	35	31	9	1.08	0.276	0.175
2.0	300	1537	26	33	7	1.10	0.292	0.143

Table 4.5: Statistics of LSPIV results based on configurations with different signal to noise thresholds.

From Table 4.5, Figure 4.7, Figure 4.8 and Figure A.8 it becomes apparent that the threshold can have a large influence on the outcome and therewith performance of LSPIV. A threshold of 1.0 tolerates all computed velocities which is problematic at locations where tracers are lacking, like in the middle of the river as is the case in Figure 4.7 (TH 1.0). However, the threshold of 1.0 shows velocities at the left bank which do seem to correspond to the measured and observed velocities but do not overcome a higher threshold. A threshold of 1.3 has, although to a lesser extent, the same problems with computing and accepting low flow velocities. Increasing the threshold to 1.8 or even 2.0 does reduce the acceptance of low velocities drastically (Figure 4.8) and therewith increases the average velocity and reduces the MAD score (Table 4.5). In contrast, the average standard deviation rises slightly and the number of windows used decreases to 138 and 108 respectively. The average velocity measured by the current meter was 1.06 m/s, this is very close to the predicted average velocities when using a threshold of 1.8 and 2.0. Eventually the best performing threshold is indicated at 1.8 based on the amount of data and average flow velocity value (Table 4.5).

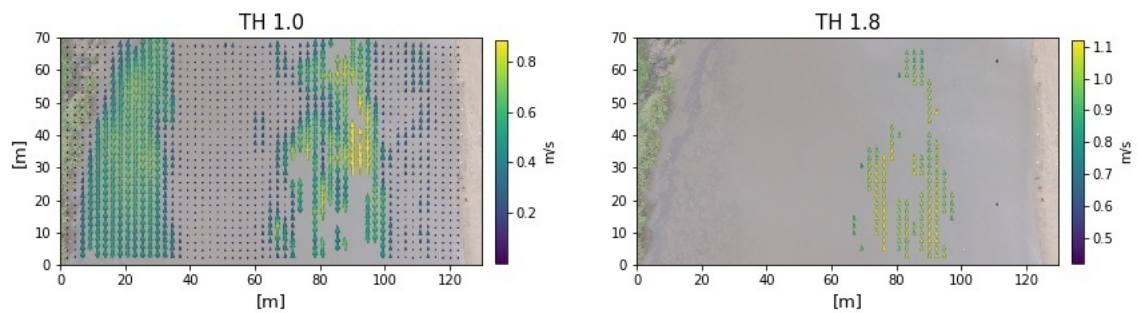


Figure 4.7: The vector fields are obtained by LSPIV using different signal to noise thresholds. Windows in the 'TH 1.0' vector field without a value are rejected by the standard deviation limit or the 50% hit boundary.

The subplots in Figure 4.8 regarding a threshold of 1.0 do show relatively high standard deviations and many low flow velocities. On the contrary, a threshold of 1.8 results in less velocities with a lower standard deviation value and all flow velocities in the flow direction (V_y) of 0.0 m/s are cancelled out. The computed velocities when using a threshold of 1.8 do appear to be much more in accordance with the current meter measurements and the regression line runs almost parallel to the 1:1 line, however, LSPIV is still underestimating with respect to the current meter measurements.

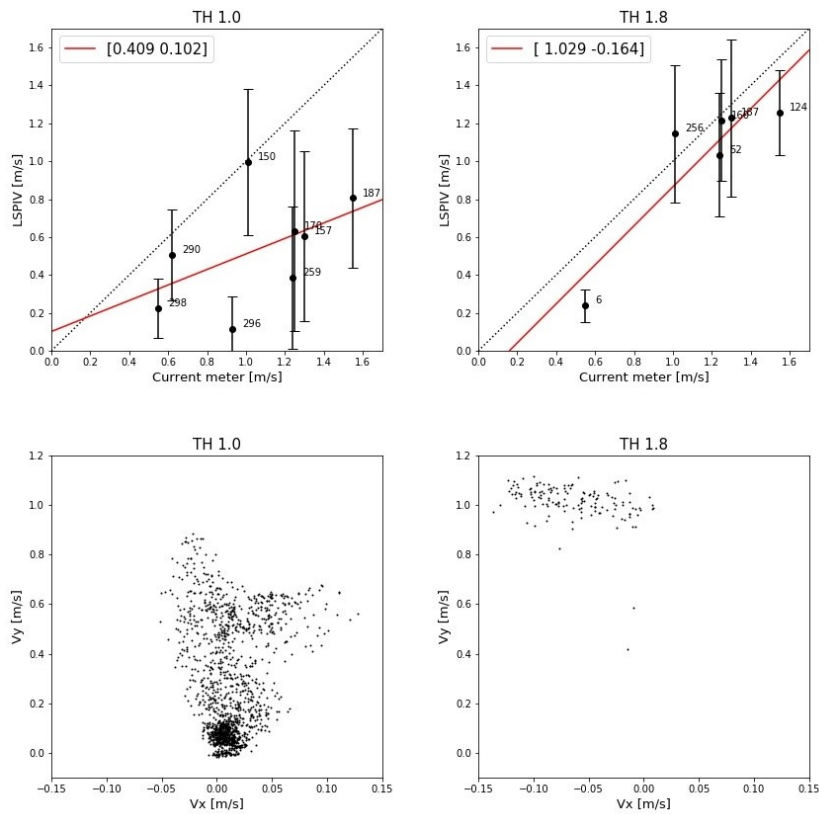


Figure 4.8: Visualized statistics of LSPIV outcomes based on different thresholds for the signal to noise ratio.

All five assessments eventually resulted in a 'optimal' performing configuration for this particular video in OpenPIV. The configuration consists of an edited video of 10 seconds with a window size of 100x100 pixels and an overlap of 50 pixels. Furthermore, the signal to noise ratio is determined with the Peak to Peak method and the threshold is set at 1.8. The velocities obtained with this configuration are eventually used to calibrate the three dimensional discharge model. The final vector field is depicted in Figure 4.9.

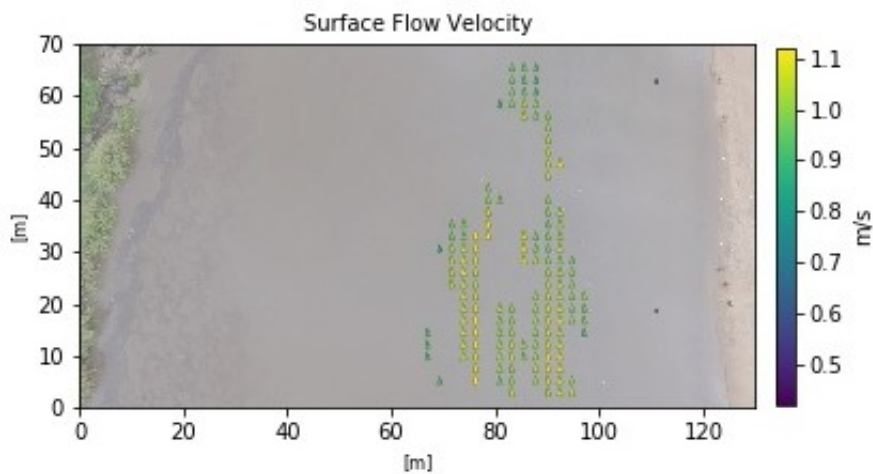


Figure 4.9: Velocity vector field based on the optimal LSPIV configuration determined in this research.

4.1.6. Changing Circumstances

The 'optimal' configuration is afterwards applied on the two videos made under different circumstances (Table 4.6 and Figure A.10). Both videos result in many computed velocities that comply with the signal to noise threshold, the two times standard deviation boundary and the 50% 'hit' limit. However, in general both videos do not show any reasonable results since all computed flow velocities are very low. The reason for this becomes apparent when observing the videos, in both of the circumstances there seems to be a lack of tracers, even though artificial tracers are seeded in one video. The seeded tracers are barely visible due to the size of the tracers compared to the size of the river. The fact that OpenPIV starts predicting low flow values in sparsely seeded areas could already be seen in assessment four and five. If different configurations or perhaps other LSPIV software (that for instance uses PTV which is claimed to produce better results for sparsely seeded rivers [23]) would result in better estimates of these videos if up for debate.

SIT	Images	Cells	With hits [%]	Avg. nr. of hits [%]	Cells > N/2 [%]	\bar{v}	\overline{STDV}
A.R.	300	1537	64	36	22	0.72	0.248
B.R.	300	1537	77	56	47	0.02	0.481
T.	300	1540	67	48	36	0.09	0.824

Table 4.6: Statistics of LSPIV results based on videos made under different circumstances.

4.2. Bathymetric Chart

The following section presents and discusses the results of this study regarding the bathymetric chart. All results originate from the method described in section 3.3. Although several intermediate results are already presented in section 3.3, the most relevant are presented and discussed once more in order to establish a proper fundament for answering the following research question:

II How can a bathymetric chart of a river be established based on photogrammetry and sonar data?

As the research question implies, different datasets are collected using various measurement equipment (section 3.3). More specifically, the fieldwork resulted in two different datasets, i.e. the 'wet' and 'dry' river bathymetry. Both datasets are point clouds containing the attributes latitude, longitude and height (x,y,z). In this section the main characteristics of the wet and dry river datasets are discussed, followed by the final bathymetric chart composed of both datasets. The bathymetric chart will eventually be used in the three dimensional discharge model.

4.2.1. Wet River Bathymetry

The wet river point cloud, shown in Figure 4.10 (A), covers 555 metres of the river length and consists of 5,164 points. The latitude and longitude originate from RTK GPS measurements whereas the height component is determined using both RTK GPS and an ADCP as described in section 3.3. The maximum and minimum height of the point cloud are 352.2 and 348.4 metres respectively.

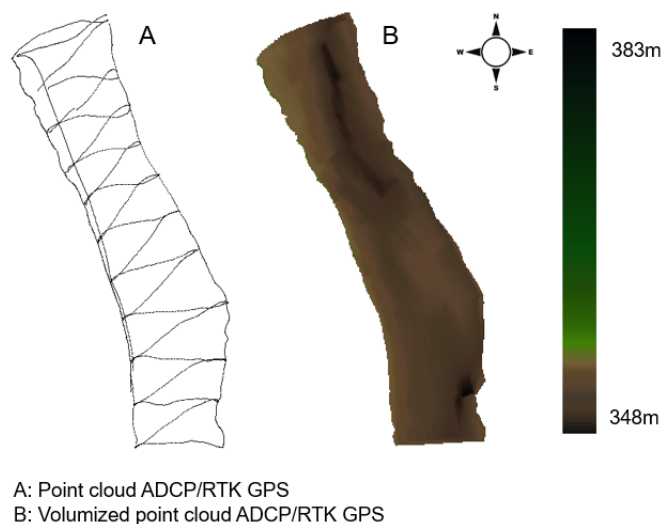


Figure 4.10: Point cloud of the 'wet' bathymetry at the time of observation. The point cloud is volumized using CloudCompare.

Figure 4.10 (B) is the volumized point cloud of Figure 4.10 (A) consisting of 62,777 points and represents the final wet river bathymetry. Assessing its accuracy against similar bathymetric charts of this area at the time of measurement is not possible since these charts simply do not exist. However, the precision of the point cloud can be determined by checking for outliers and by plotting the distribution of the height component. Visual inspection of Figure 4.10 (B) shows no discrepancies in the latitudinal and longitudinal values and Figure 4.12 shows an expected distribution of the height, ranging between 352.2 and 348.4 metres and showing no clear outliers.

4.2.2. Dry River Bathymetry

The dry river bathymetry, presented in Figure 4.11 (A), is constructed using photogrammetry and RTK GPS (section 3.3). The point cloud represents an area of 679 x 551 metres and consists of 54,265,351 points. Like the wet river, each point contains a latitude, longitude and height component with a maximum and minimum height of 383.4 (hill in the south east corner) and 350.2 metres respectively.

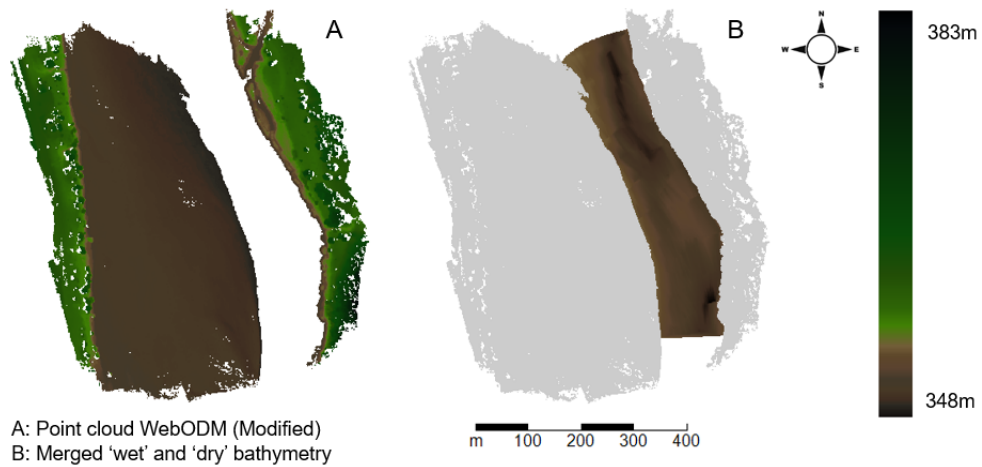


Figure 4.11: A: Point cloud of the dry river bathymetry at the time of observation. The point cloud is constructed using WebODM and merged with the wet river point cloud in CloudCompare (B).

The dry river bathymetry of Figure 4.11 (A) shows no noticeable longitudinal or latitudinal outliers based on visual observation. Likewise, no real outliers are apparent in the distribution of the height component (Figure 4.12). In general the height seems logically distributed with a large peak at 353 metres representing the almost flat floodplain. Due to this homogeneous floodplain and the hill in the southeast corner the plot does seem somewhat skewed, however, this is explained by Figure 4.11 (A) where the higher grounds in the east are clearly visible. Furthermore, the distribution plot shows several values below 352 metres which is the lowest point measured along the waterline (Figure 3.7). After extracting these values from the dataset and plotting them in CloudCompare they appeared to be located directly along the waterline on both sides of the river. In general the height of the wet river seems to correspond with the the dry river point cloud and the location of the wet river within the river banks of the dry river point cloud seems to fit rather well (Figure 4.11).

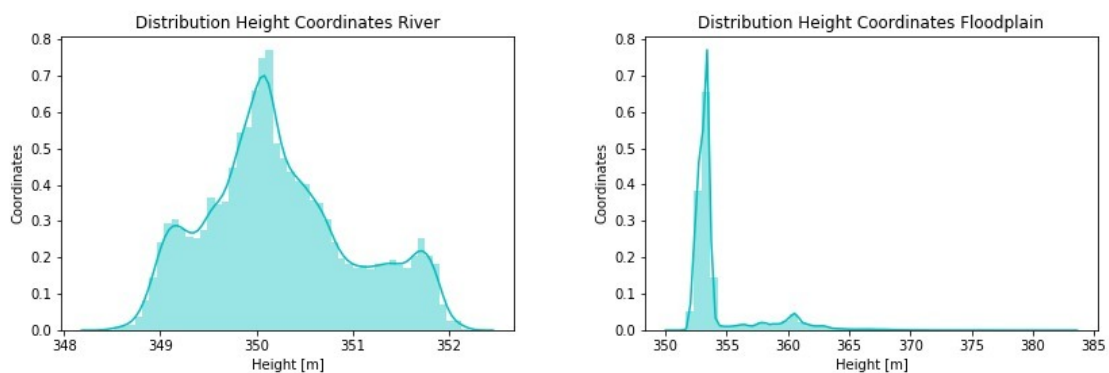


Figure 4.12: Distribution of the heights contained by the wet (river) and dry (floodplain) bathymetric charts.

4.2.3. Final Bathymetric Chart

In order to establish a complete and applicable chart, the dry and wet river point clouds are merged and volumized. The volumization process is included to generate a seamless chart and to overcome the difference in point cloud density. The final result is a homogeneous spatial distribution of the coordinates and a 'lighter' point cloud containing only 341,801 points (Figure 4.13 (A)). Afterwards the point cloud is cut perpendicular to the flow direction on both sides in order to extend the point cloud (Figure 4.13 (B)), see section 3.3 for the extension method).

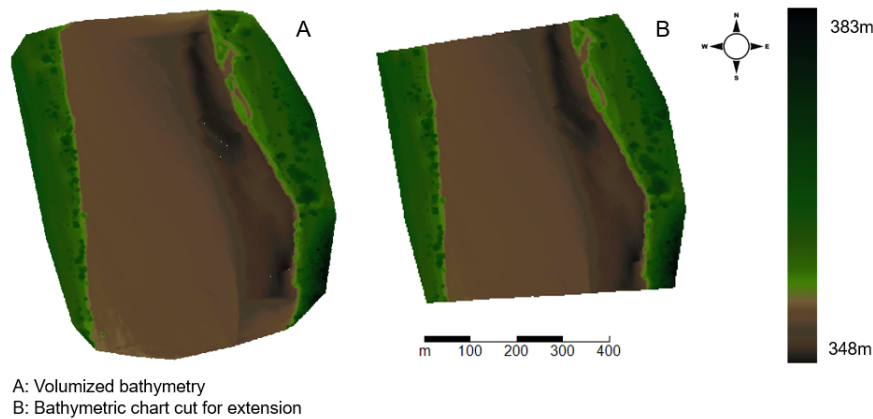


Figure 4.13: A: The final bathymetric chart of the fieldwork area made with CloudCompare. B: The chart is cut perpendicular to the flow direction in order to extend the chart.

Figure 4.14 (B) presents the final extended bathymetric chart with a length of 9209 m and a width of 539 m. The bathymetric chart contains 4,762,052 points, this proved to be just applicable in Delft3D.

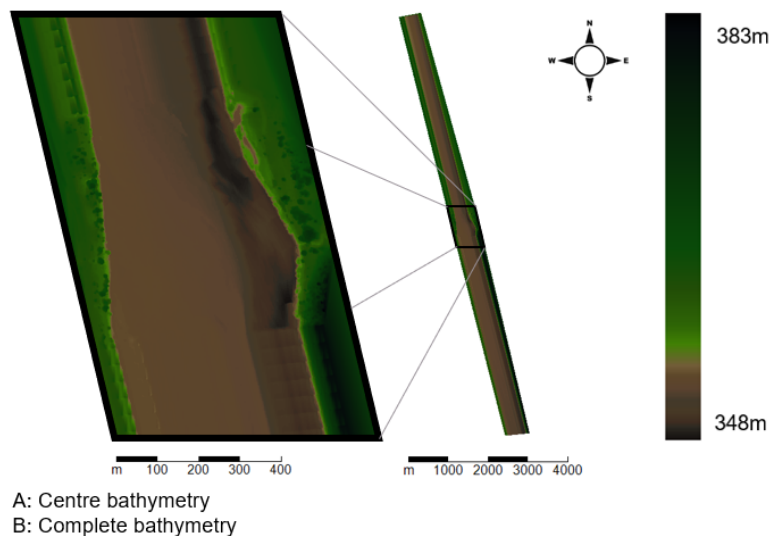


Figure 4.14: The bathymetry of the fieldwork area is extended in order to mitigate boundary condition errors used in the three dimensional model.

The distribution of the height in the extended bathymetric chart (Figure 4.15) is roughly the sum of the single wet and dry river distributions, however, a bit broadened due to the river slope. The precision of the chart seems acceptable since no clear outliers are apparent and the chart visually resembles the river as observed during fieldwork. The accuracy is due to a lack of comparable data hard to determine, however, the accuracy will influence the ability of the discharge model to simulate the river discharge correctly and therefore it is probable that the point cloud is merely accurate when the discharge model performs well. The chart shown in Figure 4.14 is the final bathymetric product and imported Delft 3D representing the bed level.

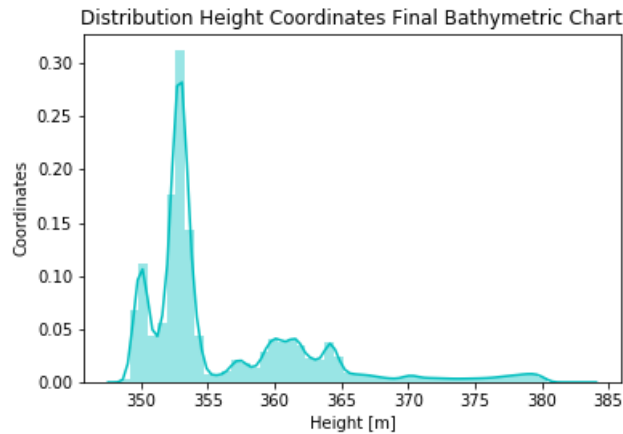


Figure 4.15: Height value distribution of the final and extended bathymetric chart.

4.3. Discharge Model

The third and final section of this chapter presents the results obtained with the discharge model. The model is based on the LSPIV surface flow velocities, ADCP measurements and the bathymetric chart as presented in previous sections. Based on the obtained results an answer will be formulated to both of the following research questions:

III How can surface flow velocity estimations be implemented in a 3D discharge model?

IIII How does the model perform compared to conventional measurements?

The model setup is presented in section 3.4.2 and consists basically of the bathymetric chart with a curvilinear grid on top containing ten layers in the vertical. The model is calibrated on the bed roughness for one known discharge with corresponding water level and surface flow velocities. The bed roughness is represented by Manning's friction coefficient and adjusted until differences between model results and measured values are minimised. The surface flow velocities are point measurements originating from both the Current Meter (CM) and the LSPIV results whereas the water level is measured with the RTK GPS (Figure B.3). The calibration is performed with 5 CM and 10 LSPIV point measurements (section 3.4.2) and 5 water levels. The model is calibrated on only one discharge ($191 \text{ m}^3/\text{s}$) since the river discharge was constant during the fieldwork period. This also implies no validation data. The calibrated model is afterwards used to simulate discharges ranging from 5 to $3000 \text{ m}^3/\text{s}$ in order to establish a stage-discharge and a width-discharge relationship for the observation area.

4.3.1. Calibration

The start value for Manning's friction coefficient is set at $0.018 \text{ s/m}^{1/3}$ since the n value (Manning) for sandy straight uniform channels ranges from 0.012 to $0.026 \text{ s/m}^{1/3}$ according to the extensive USGS guide for selecting Manning's roughness coefficients [39]. The simulated velocities for the different n values are compared to the CM and LSPIV measurements using the Mean Average Deviation (MAD). Note that this score is based on 5 measurements for the current meter and 10 for LSPIV. The simulated water level is similarly assessed with a MAD score based on 5 observation points located in the centre of the bathymetric chart (Figure 4.17). Table 4.7 provides the MAD scores of both the velocities and the water level for each applied Manning coefficient (n).

Manning [s/m ^{1/3}]	MAD CM [m/s]	[%]	MAD LSPIV [m/s]	[%]	MAD Water Level [m]
0.012	0.104	8.2	0.097	9.2	0.095
0.013	0.11	8.7	0.077	7.3	0.067
0.014	0.124	9.8	0.069	6.7	0.063
0.015	0.144	11.3	0.067	6.4	0.075
0.016	0.162	12.8	0.071	6.8	0.099
0.017	0.176	13.9	0.075	7.1	0.145
0.018	0.196	15.4	0.085	8.1	0.193
0.025	0.312	24.6	0.157	14.9	0.487

Table 4.7: Mean Average Deviation between the simulated and measured values for surface flow velocity and water level.

The first model simulation with a Manning coefficient of 0.018 s/m^{1/3} showed a slight underestimation of the surface flow velocity and an overestimation of the water level by 19 centimetres. This resulted in a substantial widening of the river due to the uniform 'flat' floodplain. Both the velocity and the water level indicate a better performance with a lower roughness value since less resistance means faster flowing water and a lower water level with equal discharge.

Lowering the n value shows better results up to $n = 0.014$ s/m^{1/3}, lower values start to systematically overestimate the flow velocities and underestimate the water level. The results in Table 4.7 point unambiguously towards 0.014 s/m^{1/3} as the best performing Manning value for the bed roughness. With $n = 0.014$ s/m^{1/3} the surface flow velocities deviate on average 6.7 percent from the LSPIV velocities without under- or overestimation compared to LSPIV (5/5), meanwhile the water level is only overestimated by 6.3 centimetres on average. The current meter measured systematically higher velocities than LSPIV as discussed in section 4.1, this is also apparent in Table 4.7 where the velocities computed by LSPIV correspond better to the simulated velocities. The n value of 0.025 s/m^{1/3} is an indication of the sensitivity of the model to the bed roughness, which is substantial as the performance decreases rapidly with drastic underestimation of the surface flow velocity and overestimation of the water level by 0.49 metres.

Figure 4.16 shows the vertical velocity profiles of three observation points (point 2, 5 and 6) simulated by the discharge model with $n = 0.014$ s/m^{1/3}. The simulated velocity at observation point two was 1.22 m/s while LSPIV and the CM computed 1.23 m/s and 1.30 m/s respectively. Observation points 5 and 6 are located in the same grid cell and have therefore the same simulated vertical velocity profile with a surface velocity of 1.1 m/s, the predicted velocities by LSPIV where 1.14 and 1.08 for point 5 and 6. All other velocity profiles can be found in Appendix C.

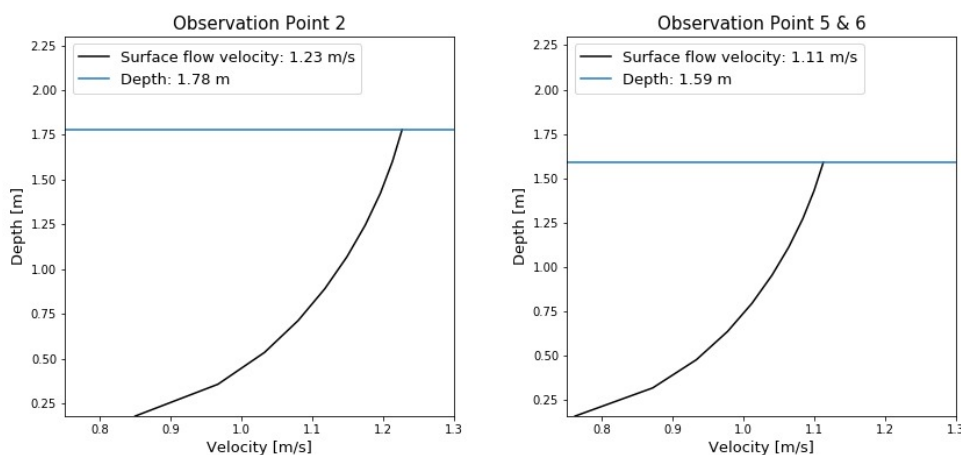


Figure 4.16: Vertical velocity profiles for a discharge of 191 m³/s with $n = 0.014$ s/m^{1/3}. Observation point 2 performs best. Observation points 5 & 6 are in the same grid cell and predict a different velocity but both are nearby the simulated velocity.

Figure 4.17 depicts the simulated water level for $Q = 191 \text{ m}^3/\text{s}$ with $n = 0.014 \text{ s}/\text{m}^{1/3}$. The waterline measured with the RTK GPS on the cart is represented by the red line (see section 3.3.2, Figure B.2 and B.3).

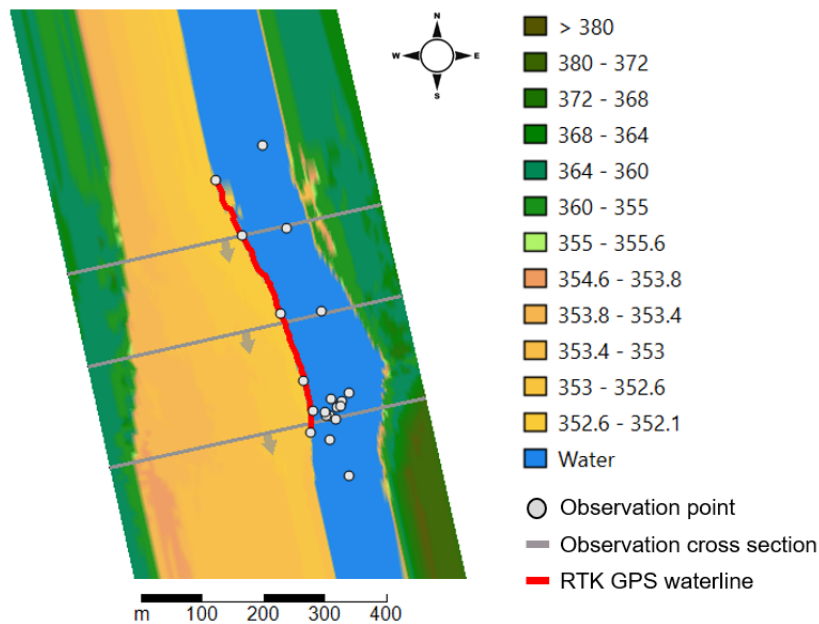


Figure 4.17: Visual representation of the discharge model at a discharge of $191 \text{ m}^3/\text{s}$ with $n = 0.014 \text{ s}/\text{m}^{1/3}$.

4.3.2. Model Results

Now that the model is constructed and calibrated, it is time to accurately predict discharges other than $191 \text{ m}^3/\text{s}$. Ideally this predictive power is assessed by a comparative study between simulated and measured water levels and surface flow velocities for different discharges. Unfortunately this kind of data is not available and therefore the assessment should be performed otherwise. Fortunately, there are two stage-discharge relationships available for locations at the Luangwa river close to the fieldwork area. The first stage-discharge relationship is established by WARMA, based on measurements taken from 1948 until 2002 at a gauging station approximately eight kilometres upstream of the observation area. The second relationship is established just four kilometres upstream by I. Abas in his master thesis research about physically based rating curves [31]. Abas based his rating curve on several measured parameters implemented in the hydraulic modelling program HEC-RAS [31]. Please note that the one dimensional approach of Abas is limited in conveyance estimation and therewith ignoring the secondary flow energy loss mechanisms (see section 4.4). Both available relationships are compared to a stage-discharge relationship constructed with the discharge model. Although this assessment gives an insight in the performance of the model it does not provide the possibility to assess the correctness of the corresponding flow velocities or simulated width of the river.

Establishing a stage-discharge relationship requires rating points (a discharge with corresponding stage) produced by the model. Hence, the model is ran 66 times with changing boundary conditions. The upstream boundary condition is given by a discharge ranging from 5 to $3000 \text{ m}^3/\text{s}$ and the downstream boundary condition is determined by the corresponding water level (see section 3.4.3 for the determination of the downstream boundary condition). Figure 4.18 visualizes six discharges simulated by the model, developing an empty river into a completely filled river discharging $1000 \text{ m}^3/\text{s}$. The river expands towards the west with increasing discharge until the steeper outer banks (see Figure C.4) are reached at approximately $660 \text{ m}^3/\text{s}$.

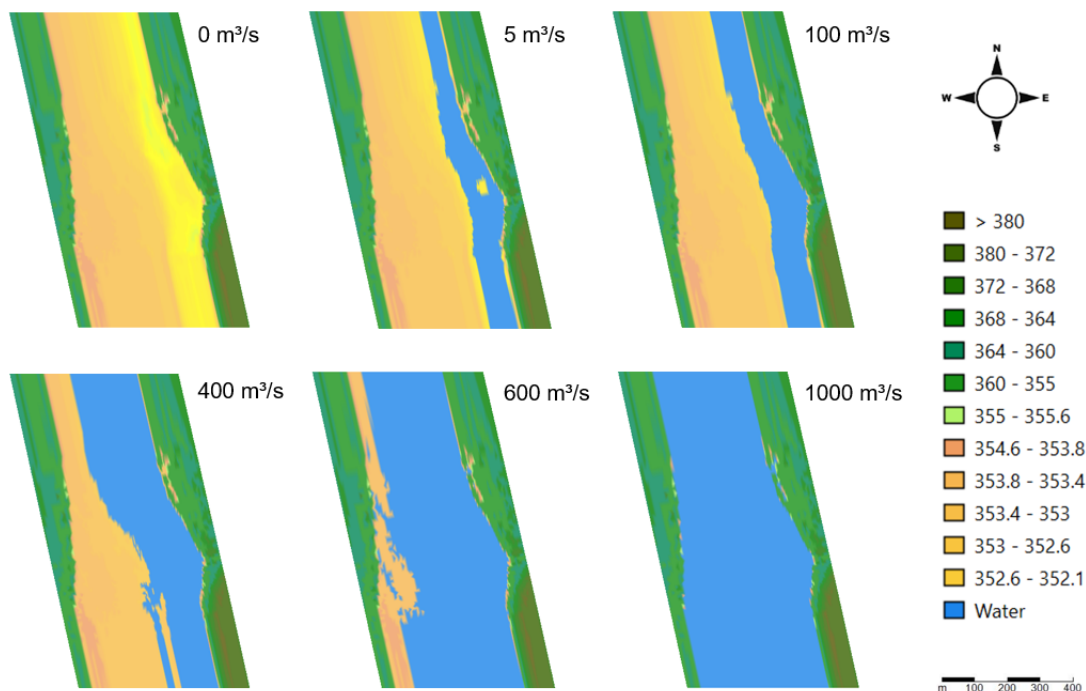


Figure 4.18: Visual representation of six discharges simulated by the model.

Based on the 66 rating points a stage-discharge relation, or rating curve, can be established. The amount of 66 is chosen in order to create a comprehensive image of the river discharges for both establishing a rating curve and visualization of the river width (Figure 4.18). When considering Figure C.3, this amount of 66 runs can be brought down to only six discharges with corresponding stages. The relation may be expressed by an equation of the following form [66] (as described in section 3.4.3):

$$Q = a(h - h_0)^b \quad (4.1)$$

Where Q represents the discharge, h the stage and h_0 the stage of zero flow. Both a and b are constants dependent on the channel characteristics [66]. In order to determine the coefficients a and b the equation may be changed to its logarithmic form:

$$\log(Q) = \log(a) + b \log(h - h_0) \quad (4.2)$$

The equation has the form of a straight line and therefore the constants a and b can be determined by fitting a simple linear regression through the discharge and stages when plotted on logarithmic scales. Then $\log(a)$ represents the intersection of the regression line with $\log(Q) = 1$ and b the gradient. However, before plotting $\log(Q)$ against $\log(h - h_0)$ the stage of zero flow (h_0) needs to be determined.

The stage of zero flow, also referred to as the datum correction [66], is the stage at which discharge Q is zero. The datum correction h_0 can be simply assumed as the lowest point of the cross section or be determined by iterating over different h_0 values until the best fit for the linear regression is found (the highest R-squared) [66]. The lowest point in the cross section is 348.92 m whereas $h_0 = 350.02$ m results in the best regression fit. This implies 1.1 metres of standing water in the cross section without any flow in the river, which is only possible if the cross section is placed in a local depression of the bed level, i.e. the river bed has to rise in downstream direction of the cross section. The third option used to find h_0 was running the model for almost zero flow ($Q = 0.2$ m³/s), this resulted in a h_0 close to 349.35 m. Figure 4.19 visualizes the three possible datum corrections of the northern cross section.

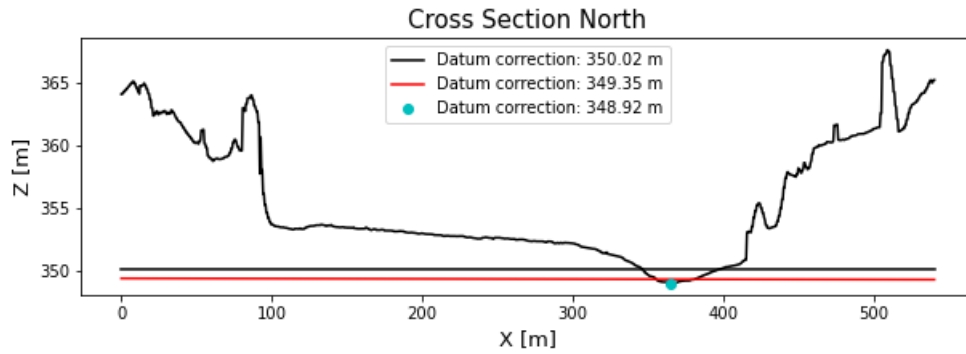


Figure 4.19: Three possible datum corrections for the northern cross section.

In order to determine the constants a and b the discharges can be plotted against the corresponding stages on logarithmic scales by using the three datum correction values (Figure 4.20). However, changing h_0 does of course change the parabola shape of the stage-relationship and therewith the constants. Figure 4.20 and Table 4.8 show the different values for a and b given a certain h_0 and indicate the sensitivity of the constants to a change in the datum correction.

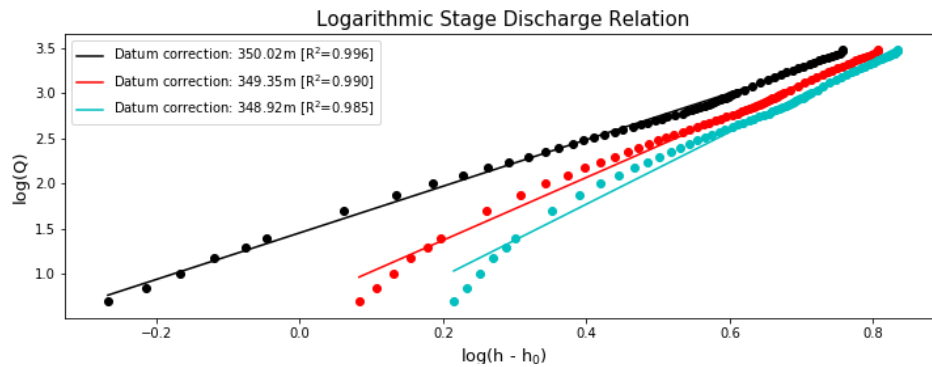


Figure 4.20: Three linear regression lines based on the same stage-discharge dataset while using different datum corrections.

Datum correction [m]	R-squared	a	b
350.02	0.996	28.58	2.58
349.35	0.990	4.77	3.47
348.92	0.985	1.50	3.99

Table 4.8: The stage-discharge relationship constants a and b are strongly dependent on the chosen datum correction.

Constant b is defined by the geometry of the cross section [66] with $b = 3/2$ for rectangular cross sections and approximately $b = 5/2$ for more triangular shaped rivers. Based on the R-squared values, the correction datum of 350.02 m seems to produce the best fit, however, the model predicts a discharge of $1.25 \text{ m}^3/\text{s}$ for $h = 350.02 \text{ m}$.

In order to determine the most plausible datum correction, all three relationships are plotted in Figure 4.21 together with the rating curves established by WARMA and Abas [31]. Striking in the (black) rating curve corresponding to the datum correction of 350.02 m since it stops at a discharge of $2600 \text{ m}^3/\text{s}$. This shows that the relatively high correction datum results in a lower stage ($h - h_0$) than predicted by the model. In other words, with a correction datum of 350.02 m the rating curve expects a discharge of $2600 \text{ m}^3/\text{s}$ where the model simulates $3000 \text{ m}^3/\text{s}$, therefore this stage-discharge relation is rejected. The other relationships are fairly similar to the stage-discharge relationship of WARMA, the

differences are most likely caused by a different river geometry and to lesser extent also measurement uncertainties.

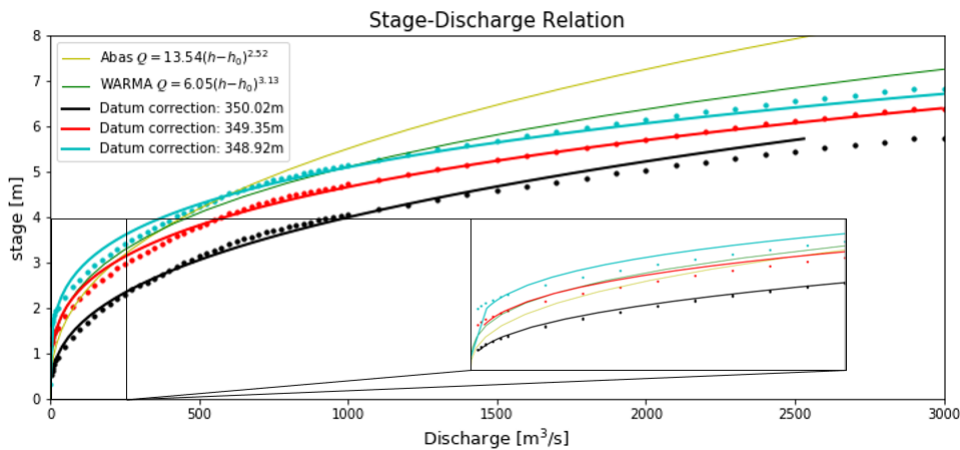


Figure 4.21: Stage-discharge relationships established with different datum correction values combined with the rating curves established by WARMA and Abas [31]

If the two remaining rating curves are compared in a similar way, the curve based on $h_0 = 349.35$ m performs better since it predicts almost exactly the modelled discharge. For example, a simulation of 3000 m³/s produces a stage of 355.75 m, implementing this stage in both relationships results in 2992 and 3202 m³/s for the higher and lower correction datum respectively. This could of course be expected since the higher correction datum is based on $Q = 0$ m³/s in the model.

The stage-discharge relationship contains, besides the correction datum, also an uncertainty in the model output. This uncertainty is due to the calibration largely captured in the roughness coefficient. The base values of Manning’s roughness coefficient for sandy uniform rivers ranges from 0.012 to 0.026 s/m^{1/3} according to the USGS guide for selecting Manning’s roughness coefficients [39] (see section 4.3.1). Therefore these values are regarded as the uncertainty boundaries for the stage-discharge relationship established in this research. The model is ran with six different discharges, based on Figure C.3, for both roughness boundary values. The stage-discharge relationship with $n = 0.014$ s/m^{1/3} is plotted with the uncertainty band in Figure 4.22. Besides uncertainty in the stage-discharge relationship, it is to keep in mind that the stage measurement itself is likely to encapsulate a certain uncertainty as well.

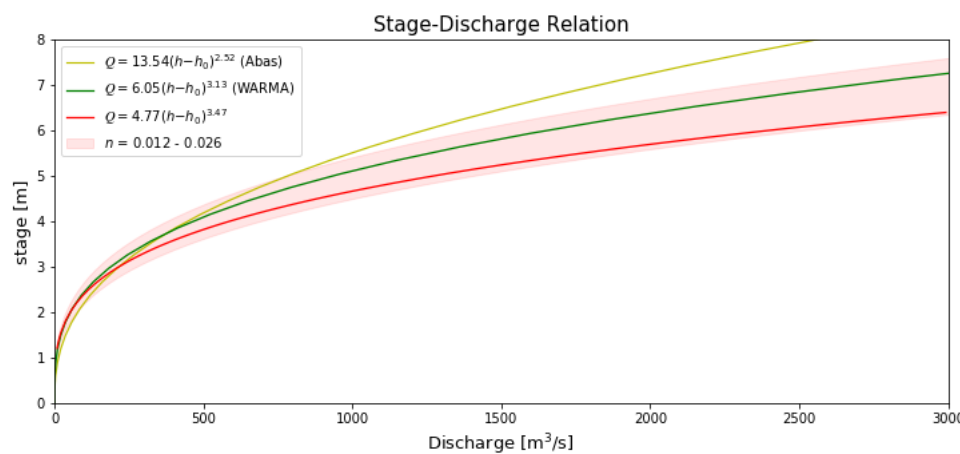


Figure 4.22: The final stage-discharge relationship plotted with an uncertainty band based on minimum and maximum roughness coefficients according to [39].

Since there is no stage data available for discharges other than $191 \text{ m}^3/\text{s}$ and since comparing the relationship with the relationships of WARMA and Abas is only insight full to a certain extent (due to differences in the river geometry), the final stage-discharge relationship is expressed by equation 4.3. This relationship should function as a basis on which adjustments can be made based on newly available stage-discharge data. Note that the river geometry will most likely change over time, due to the sandy bed-level, and therefore the constants a and b are not stable over time.

$$Q = 4.77(h - h_0)^{3.47} \quad (4.3)$$

In this research an attempt is made to establish a width-discharge relationship for the northern and centre cross sections (Figure 4.23). The advantage of width-discharge relationships over stage-discharge relationships lies in the possibility of determining river width based on remote sensed data as shown by Van der Vliet in his master thesis [79]. Van der Vliet was able to obtain sub-pixel accurate river-width estimations from satellite data by discriminating in satellite bands. Using remote sensed determination of river width in a discharge model as presented in this study seems to largely substitute the need for manual river discharge measurements. This is especially true for a river like the Luangwa with a large and relatively 'flat' floodplain because such rivers grow significantly in width with increasing discharge.

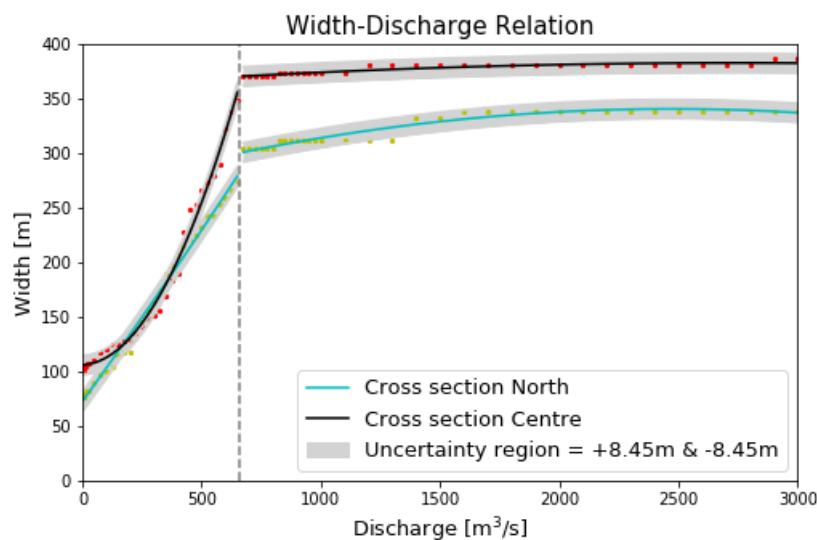


Figure 4.23: Width-discharge relationships for the northern and centre cross sections with an confidence band based on uncertainties in river width estimation and model grid size.

The attempt made in Figure 4.23 shows a clear division at an approximate discharge of $660 \text{ m}^3/\text{s}$ for both relationships. The lower discharges are showing a sharp increasing width, representing the river covering the floodplain, until the division which represents the river reaching the steeper banks as depicted in Figure 4.19 and C.4. The river does not increase much more in width from $Q = 660 \text{ m}^3/\text{s}$ and is therefore not suitable anymore for a width-discharge relationship. However, the first segments are highly suitable and by fitting a first, or second in case of Figure 4.23, polynomial through the data the width-discharge relationship can be expressed in an equation. The uncertainty bands around the polynomials in Figure 4.23 are based on the measurement uncertainty rather than on the possible roughness coefficient range. This is done since the uncertainty in width determination is specifically defined by Van der Vliet at approximately 5 metres [79]. Furthermore, the width determination within the model is mostly dependent on the cell size of the model grid which is, in this model, 3.45 metres. Therefore the uncertainty band covers plus and minus 8.45 metres around the polynomials. Please note that, although the roughness coefficient is not considered in the uncertainty band, it can still have a large influence on the river width.

4.4. Considerations, Prospects and Limitations

This section summarizes and elaborates on the considerations about the final results in this research and on the discharge measurement technique as a whole. Further, the main limitations and the prospects of the methods are discussed while bearing the purpose of applicability in low-resource settings in mind. In general, the results in this research regarding LSPIV, the bathymetric chart and the hydraulic model are considered satisfactory with respect to the initial expectations.

OpenPIV appeared to be relatively insensitive to several of the studied variables (i.e. the video editing and length) but highly influenced by the signal to noise ratio, its threshold and the window size. This facilitates the practical applications of LSPIV by water authorities like WARMA since a short video of the river surface (i.e. 5 seconds) is easily made (when having access to a drone) and processing only entails running the OpenPIV script while tweaking less variables than initially thought. However, the one major disadvantage of LSPIV is the dependency on sufficient tracers floating on the river surface which ought to be detected by the applied software (i.e. the tracers need to have the right size and color while there is minimal specular reflection during the recording). LSPIV is in general, and in this research, portrayed as a non-intrusive measurement technique, however, the LSPIV results are validated against the intrusive current meter measurements, if this proves to be necessary on a regular basis the method loses its non-intrusive character and therewith its corresponding benefits as mentioned in section 1.2. Furthermore, during high water, in low resource settings or at difficult accessible observation sites it is not always possible to measure with a current meter. This raises the question if it is possible to determine accurate surface flow velocities, suited for implementation in an hydraulic model, solely based on a short video. Although further research is required, this study shows that OpenPIV, and perhaps LSPIV in general, is not likely to systematically overestimate the flow velocities and therefore one can focus mainly on outliers and computed low surface flow velocity values which enhances the possibility of independent usage of LSPIV. The prospects for LSPIV as a component in discharge measuring seems mainly dependent on the method with which the discharge is computed after the surface flow velocities are obtained. The widely used velocity-area method is simple and only requires knowledge of the geometry of the river cross section, however, a major drawback is the dependency on equally distributed tracers over the width of the river or the software resorts to interpolation between windows with a computed velocity. From this research it appears that this method is perhaps suitable for small rivers but that it will generate problems for medium- and large-sized rivers as the Luangwa. Using a three dimensional model solves this issue since it does not require surface flow velocities in all windows (see section 3.2.2). However, creating a comprehensive three dimensional hydraulic model can be a challenging task which generates its own difficulties.

Perhaps the most challenging task on the road to a three dimensional hydraulic model is establishing an accurate bathymetric chart of the observation area. This research showed that, with decent preparation and the right equipment, it is possible to gather the needed data in less than one fieldwork day. This is a promising sign regarding the practical implementation of three dimensional hydraulic models for discharge measurements on a larger scale, especially since gathering the bathymetric data comprises the majority of the fieldwork operations. Furthermore, the use of relatively simple measurement equipment (i.e. a standard drone, a single beam ADCP and a low-cost RTK GPS) makes the establishment of an accurate bathymetric chart also possible in relatively low resource settings. The main challenge in the creation of an accurate bathymetric chart lies, however, predominantly in the data processing part. The toughest issue to overcome while creating a chart of a reasonable size is, at least in this research, mitigating the bowing effect originating from the shape of the camera lens and produced by WebODM. The solution provided in this research seems sufficient, however, it is heavily dependent on one track along the waterline made with the RTK GPS. This dependency makes the solution vulnerable and it does not solve the whole issue since it only 'straightens' the chart in the direction of flow. Although the provided solution is satisfactory in this case, a more solid solution is desirable. Creating the 'wet' river bathymetry does form less of an obstacle as it requires only a boat, ADCP and low-cost RTK GPS during the fieldwork day and the processing is relatively straight forward. Finally, merging the point clouds and adding the extensions should not form any difficulty when using CloudCompare and the extension script. Taken all of the above into account, this research showed that with limited and low-cost equipment an accurate bathymetric chart can be established which provides a promising outlook for discharge measurements in areas with limited resources.

When deciding on which hydraulic model would suit the task and is applicable in low resource settings and otherwise, the consideration is based on both performance and complexity of the available models. In general it can be assumed that the simplest model which provides just the amount of required complexity is the desired option [59]. The simplest model would, in this case, use a one dimensional approach for establishing a stage-discharge relationship, like done by Abas [31]. However a one dimensional hydraulic model is limited in several ways including the conveyance estimation and therewith ignoring the secondary (lateral) flow energy loss mechanisms when the river is expanding towards the outer banks [12]. Hence, a one dimensional model is disregarded as it does not provide the required amount of complexity. A two dimensional discharge model would be able to take these lateral energy losses into account but it will be impossible to calibrate with surface flow velocities obtained with LSPIV since a two dimensional model would only compute an average velocity over the vertical. Therefore a three dimensional model is required, like the Delft3D D-Flow FM model used in this research. Delft3D D-Flow FM is easy to use due to the intuitive ribbon interface (facilitating large-scale application) and the model takes the lateral energy losses into account while it computes surface flow velocities which can be compared to LSPIV outcomes. All in all Delft3D seems an appropriate choice, however, the model provides perhaps too much complexity as the majority of the parameters in Delft3D are unknown and therefore left at default settings. These default parameters add a certain degree of uncertainty to the model. Furthermore, Delft3D is the only software in this research which is not open source and even relatively expensive to acquire. Nevertheless, Delft3D did seem the right model for the task and in retrospect the model did perform as expected.

It is of importance to keep in mind that the uncertainty in the model, and therewith in the computed discharges, is not only encapsulated by the unknown (default) parameters but also largely in the Manning roughness coefficient (due to the calibration), in a possible change in bathymetry, in the field measurements of stage and, in case of a width-discharge relationship, in the remotely determined river width as defined by Van der Vliet [79]. Furthermore, the roughness coefficient is assumed constant over the whole river width although the more extended non-permanent channel (i.e. the floodplain at time of observation) did not only consist of a sandy bed but did contain increasing amounts of gravel when moving towards the steeper outer banks. These sources of uncertainty do limit the confidence with which the discharges can be determined but the uncertainty can partly be reduced by, e.g., estimating the roughness on forehand, implementing different roughness values in the model or measuring extra parameters and measuring more accurately. In this research the dominant limiting factor is without question the lack of validation data, however, the research shows that creating a three dimensional hydraulic model with low-cost equipment is possible while using the non-intrusive measurement technique LSPIV for calibration purposes. Therewith this research contributes to the goal of creating an accurate and easy to use discharge measurement method suitable for relatively low-resource settings like Zambia.

5

Conclusion

The aim of this research was developing a three dimensional river discharge model able to include surface flow velocities measured with Large-Scale Particle Image Velocimetry. With developing such a model a more physically based stage-discharge relationship can be determined based on non-intrusive measurements. The study is based on data collected at the Luangwa river in Zambia. The data is used to create a bathymetric chart and for the computation of the surface flow velocities, which both are used in the discharge model. This chapter presents the main conclusions drawn from the research based on the four research questions.

I How to utilize Large-Scale Particle Image Velocimetry to obtain surface flow velocity estimations intended for the use in a 3D discharge model?

Since the utilization of LSPIV depends partly on the input, this will be addressed before focusing on the usage of the technique itself.

The input of LSPIV generally consists of a set consecutive images extracted from a video. This video needs to meet with only two basic requirements in order to be applicable in LSPIV: the video has to contain sufficient visible tracers, i.e. a single tracer should have the size and color to be clearly outlined against the river surface, and specular reflection of sunlight on the river surface should be minimised. Naturally there are many other factors that need to be considered since they can influence the applicability of a video and hence the performance of LSPIV. These factors include tracer coverage over the complete width of the river in order to compute a homogeneous vector field and recording the video in nadir direction, i.e., orthogonal to the river surface. As stated, these factors can influence the performance but are not necessary requirements since they can be overcome by substitution of the velocity-area method and orthorectification respectively. Furthermore, a video of 10 seconds does generally suffice but recording somewhat longer provides the possibility to choose the most stable seconds in the video. In this research video editing did not show a clear improvement in the performance of LSPIV.

Although acquiring the input is similar for all applications of LSPIV, the utilization can be substantially different due to a shift in the demanded output. Since the output velocities will not be used to determine the discharge with the common velocity-area method but to calibrate a hydraulic model, intended to reconstruct discharges through assimilation of local proxy observations, LSPIV does not need to compute a velocity vector for each window. This means the interpolation function can and should be ignored, a relatively high signal to noise threshold can be set and other limitations can be applied. This will result in only a percentage of the windows with a computed velocity vector but these velocities contain much less uncertainty.

II How can a bathymetric chart of a river be established based on photogrammetry and sonar data?

The bathymetry of most rivers can generally be divided in a submerged (wet) area and a floodplain (dry area). Hence, mapping both areas requires two different measurement devices, that is sonar for the submerged part and photogrammetry for the floodplain. Both sonar and photogrammetry need to be combined with RTK GPS to link the measurements to a precise location. In order to answer the research question, the wet and dry bathymetry will be addressed separately.

The wet, or submerged, bathymetry can be mapped by manoeuvring an ADCP equipped with RTK GPS in a zig-zag pattern over the area of interest, while both devices measure automatically based on a short time interval. Thereafter, each locations can be linked to the corresponding depth measurement based on, e.g., a timestamp. The depth measurement can subsequently be extracted from the height measurement of the RTK GPS in order to obtain the exact height of the riverbed. However, the height component of the RTK GPS contains generally a higher uncertainty than the latitude and longitude measurements. Therefore it is preferable to determine the water level by fitting a linear equation through numerous RTK GPS points collected in a straight line along the waterline. Although these measurements contain the same uncertainty in the height component, this will be balanced out by the linear relationship representing the waterline with a certain hydraulic slope represented by the gradient. Now the bed level can be obtained by subtracting the ADCP depth measurements from a corresponding water level. Furthermore, the volumization of the wet river point cloud should only be performed using the transects only (i.e. not the waterline or riverbank measurements) since most river channels have a more or less steady shape in the direction of flow (e.g. rectangular, triangular or concave). If the waterline and riverbank measurements are included, the bed level will be slightly elevated at the banks due to the linear character of the interpolation function.

Using photogrammetry in combination with RTK GPS to map the dry river bathymetry is quick, simple and results in a very detailed elevation model. However, if the area is somewhat extensive it can be subject to deformations due to the curvature of the camera lens. WebODM does have built-in correction methods in order to mitigate these deformations but they tend to overcompensate. Fortunately, the linear equation representing the waterline (established for the wet bathymetry) can again provide a solution by indicating the offset of each coordinate along the waterline in the elevation model. This offset can be used to 'straighten' the model in the flow direction.

Both point clouds can eventually be merged with software like CloudCompare and subsequently be extended in both up- and downstream direction. The extensions will mitigate errors in the imposed boundary conditions in the discharge model, hence the preferable length of the extensions is equal to the adaptation length of the river. Furthermore, the bathymetric chart should be volumized in order to obtain a homogeneous point cloud containing less points in total, this is preferable since a 'lighter' bathymetric chart means faster processing in the discharge model.

III How can surface flow velocity estimations be implemented in a 3D discharge model?

In short, point velocity measurements can not be implemented as a condition in a Delft3D Flow Flexible Mesh Model. However, these point velocities can, conversely, be computed by the model (per grid cell) and obtained after each model simulation. Hence, the measured velocities can be used in the calibration process of the model. The model can be calibrated on the roughness coefficient since this parameter is yet unknown while other inputs, i.e., the bathymetric chart including the slope, the discharge upstream and a water level downstream are already established or known. The roughness coefficient, can be iterated until the simulated velocities correspond to the measured velocities. However, only iterating towards corresponding velocities does not suffice since discharge is dependent on both the average velocity and the cross sectional area of the river, therefore the iteration process should be based on both the water level and the velocities.

III How does the model perform compared to conventional measurements?

The discharge model is resembling the actual river in location, depth, width and surface flow velocity when using a Manning friction coefficient of $n = 0.014 \text{ s/m}^{1/3}$ for $Q = 191 \text{ m}^3/\text{s}$. The LSPIV velocities are approached to a mean average deviation of 0.07 m/s and the water level deviates 0.063 m at the research area. However, this is allowed for by the roughness coefficient. A Manning roughness coefficient of $0.014 \text{ s/m}^{1/3}$ falls within the range for straight uniform sandy channels but does appear to be somewhat low, possibly caused by the used river slope which is measured over only 439 metres.

Unfortunately, the river discharge did not change during the fieldwork period and therefore the model predictions could not be compared to conventional measurement techniques for different discharges. In other words, this implies the absence of validation data. However, the model is used to predict the water level at certain cross sections for 66 different discharges. These water levels are used to establish a stage-discharge relationship which is subsequently compared to two already existing relationships. The stage-discharge relationship proved to be fairly similar to the rating curve of WARMA although the geometry of the river at both sites is likely to be different. Since a stage-discharge relationship is heavily dependent on the geometry this comparison is only a rough indication of the accuracy of the relationship. Ideally, the discharge, water level, and surface flow velocity for different discharges should be measured over time and compared (using the model) to the established relationship. The stage-discharge relationship could, if needed, be adjusted based on the new measurements.

The answers to the four research questions above do together answer the main question. However, in order to give a very concise answer to the main question of this research, the four answers are combined and summarized below.

How can optical surface flow velocity estimations, sonar and photogrammetry be used to establish a discharge model of medium-sized rivers?

With sonar and photogrammetry a detailed bathymetric chart can be created which can serve as the bed level for a three dimensional discharge model. The model needs subsequently input like discharge, water levels and a roughness coefficient. The roughness coefficient can be determined by calibration if the water level and flow velocity are known for a certain discharge. The discharge can be measured with an ADCP, the water level with RTK GPS and the surface flow velocity with Large-Scale Particle Image Velocimetry. If the optimal roughness coefficient is determined the model may be used to simulate other discharges and therewith creating a more physically based stage-discharge relationship.

6

Recommendations

This chapter presents recommendations for future research with a (partially) similar objective. The recommendations are mainly gathered in retrospect, meaning that they are based on experience gained during the course of this study. Most recommendations regard measurement techniques or processing methods and some consider further research focused on a specific topic in order to gain more information and a better overview on the matter. The chapter is divided in recommendations on Large-Scale Particle Image Velocimetry, establishing a bathymetric chart and discharge modelling.

6.1. Large-Scale Particle Image Velocimetry

For all rivers with a minimum width of several tens of meters, it is recommended to do reconnaissance before recording any videos. This is because it is likely necessary to seed artificial tracers in a river of this size under normal flow conditions. These tracers need to be selected with care since it depends on the size and color of the tracers if they will be outlined against the river surface and therewith visible for LSPIV. Furthermore, during reconnaissance one should take the geometry of the river and structures that create backwater curves into account.

In section 4.1 the final output does not compute any velocities at the left bank that overcome the set thresholds or other limiting conditions. This is remarkable since many tracers are visible and other configurations, i.e. Peak to Mean signal to noise method and Threshold = 1.0, do compute likely velocities in this area. From Figure 4.7 it seems that aggregation of both outcomes (TH = 1.0 and TH = 1.8) would result in an almost completely homogeneous vector field with likely velocity predictions at both banks. However, the windows in the centre of the river will still contain very low velocity values but this can be overcome by a minimum velocity threshold. Although manoeuvring LSPIV in this configuration contains some arbitrary decisions it will likely result in a better outcome.

6.2. Bathymetric Chart

In this research an ADCP with a single-beam sonar is tied to a wooden canoe and moved over the river in order to establish a point cloud representing the river bathymetry. In future research it is recommended to use perhaps other methods to manoeuvre a floating sonar because this method required entering the, somewhat unstable, canoe with valuable equipment like a laptop, smartphone and RTK GPS in a with crocodiles and hippos infested river. One can think of a different boat or a floating sonar dragged over the river surface by a drone. Please note that much battery power will be required for this procedure while taking some flight time into account for photogrammetry if necessary.

Furthermore, using a more sophisticated multi-beam sonar instead of a single-beam device could possibly generate a more homogeneous and detailed bathymetric chart of the river. However, multi-beam devices are generally costly compared to the single beam variant and therefore less suited for low-resource settings.

Another option is to disregard the sonar and focus on LiDAR data to acquire river depth data. However, as stated in section 2.3 this requires a relatively shallow river with clear water.

6.3. Discharge Model

In this research the roughness coefficient is used to calibrate the discharge model, which is common practice as stated in section 2.4. However, while fitting the model to the test data most of the uncertainty will be encapsulated in the roughness coefficient. Therefore, it is recommended to estimate a range of bed roughness values, based on grain or pebble size, ground surface irregularities and vegetation elements. This restricts the model to get an accurate fit at the expense of the roughness coefficients accuracy.

The surface flow velocities computed with the discharge model are extracted as the average velocity in the upper vertical layer. In this research an equal layer distribution is used of ten layers, resulting in an upper layer that represents ten percent of the river depth. It could be worthwhile to change this layer distribution towards a smaller upper layer and assess the differences in produced surface flow velocity and therewith possibly obtain a different value for the roughness coefficient.

Bibliography

- [1] Casas A., Lane S. N., Yu D., and Benito G. A method for parameterising roughness and topographic sub-grid scale effects in hydraulic modelling from lidar data. *Hydrology and Earth System Sciences*, 14(8):1567, 2010.
- [2] Forsyth D. A. and Ponce J. *Computer vision: A modern approach*. Upper Saddle River, NJ: Prentice Hall, 2011.
- [3] Hauet A., Kruger A., Krajewski W. F., Bradley A., Muste M., Creutin J. D., and Wilson M. Experimental system for real-time discharge estimation using an image-based method. *Journal of hydrologic engineering*, pages 105 – 110, 2008.
- [4] Hauet A., Kruger A., Krajewski W., M. Bradley A. and Muste, Creutin J.D, and M. Wilson. Experimental system for real-time discharge estimation using an image-based method. *Journal of Hydrology*, 13(2):105 – 110, 2008. doi: doi:10.1061/(ASCE)1084-0699[2008]13:2(105).
- [5] Kumar A. and Choudhury R. *Principles of Colour and Appearance Measurement. Object Appearance, Colour Perception and Instrumental Measurement*. Elsevier, 2014.
- [6] Leese J. A., Novak C. S., and Clark B. B. An automated technique for obtaining cloud motion from geosynchronous satellite data using cross correlation. *Journal of Applied Meteorology*, 10:118 – 132, 1971. doi: 10.1175/1520-0450(1971)010<0118:AATFOC>2.0.CO;2.
- [7] Marcus W. A. and Fonstad M. A. Optical remote mapping of rivers at sub-meter resolutions and watershed extents. *Earth Surface Processes and Landforms: The Journal of the British Geomorphological Research Group*, 33(1):4–24, 2008.
- [8] Tazioli A. Experimental methods for river discharge measurements: Comparison among tracers and current meter. *Hydrological Sciences Journal*, 56(7):1314–1324, 2011. doi: DOI:10.1080/02626667.2011.607822.
- [9] ArduSimple, 2020. URL <https://www.ardusimple.com/simplertk2b/>. Last accessed 21 April 2020.
- [10] ArduSimple, 2020. URL <https://www.ardusimple.com/product/radio-module-long-range/>. Last accessed 21 April 2020.
- [11] Guenther G. C. Airborne lidar bathymetry. *Digital elevation model technologies and applications: the DEM users manual*, 2:253–320, 2007.
- [12] McGahey C. and Samuels P. G. Methodology for conveyance estimation in two-stage straight, skewed and meandering channels. In *Proceedings of the congress of the international association for hydraulic research*, volume 1, pages 33–40, 2003.
- [13] CloudCompare, 2020. URL <https://www.cloudcompare.org/>. Last accessed 08 April 2020.
- [14] Creutin J. D., Muste M., Bradley A. A., Kim S. C., and Kruger A. River gauging using piv techniques: a proof of concept experiment on the iowa river. *Journal of hydrology*, 277:182 – 194, 2003.
- [15] Stern R. D. and Cooper P. J. M. Assessing climate risk and climate change using rainfall data - a case study from zambia. *Experimental agriculture*, 47, Special Issue 2:241 – 266, 2011. doi: doi:10.1017/S0014479711000081.
- [16] Deltares. *D-Flow Flexible Mesh, User Manual*, .
- [17] Deltares. *RGFGRID, User Manual*, .

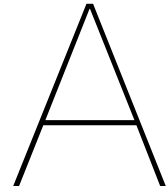
- [18] DIGI, 2020. URL <https://www.digi.com/products/embedded-systems/digi-bee/digi-xbee-tools/xctu>. Last accessed 21 April 2020.
- [19] DJI, 2020. URL <https://www.dji.com/nl/phantom-4/info/>. Last accessed 03 April 2020.
- [20] Alsdorf D. E., Rodriguez E., and Lettenmaier D. P. Measuring surface water from space. *Reviews of Geophysics*, 45(2), 2007.
- [21] Bandini F., Olesen D. H., Jakobsen J., Kittel C. M. M., Wang S., Garcia M., and Bauer-Gottwein P. Bathymetry observations of inland water bodies using a tethered single-beam sonar controlled by an unmanned aerial vehicle. *Hydrology and Earth System Sciences*, 22(8):4165–4181, 2018.
- [22] Tauro F., Porfiri M., and Grimaldi S. Orienting the camera and firing lasers to enhance large scale particle image velocimetry for streamflow monitoring. *Water Resources Research*, 50(9):7470–7483, 2014.
- [23] Tauro F., Piscopia R., and Grimaldi S. Streamflow observations from cameras: Large-scale particle image velocimetry or particle tracking velocimetry. *Water resources research*, 53, 10:374 – 394, 2017. doi: doi.org/10.1002/2017WR020848.
- [24] Bodart G., Hauet A., Le Coz J., Jodeau M., Faure J., and Marchand B. Improvements of Ispiv method and implementation in fudaa-Ispiv software. *21st EGU General Assembly, EGU2019*, 2019.
- [25] Dramais G., Le Coz J., Camenen B., and Hauet A. Advantages of a mobile Ispiv method for measuring flood discharges and improving stage-discharge curves. *Journal of Hydro-environment research*, 5:301 – 312, 2010.
- [26] Dramais G., Le Coz J., Camenena B., and Hauet A. Advantages of a mobile Ispiv method for measuring flood discharges and improving stage–discharge curves. *Journal of Hydro-environment Research*, 5:301–312, 2011. doi: <https://doi.org/10.1016/j.jher.2010.12.005>.
- [27] Samuels P. G. Cross section location in one-dimensional models. In *International Conference on river flood hydraulics*, pages 339–350. Wiley Chichester, 1990.
- [28] Omroep Gelderland, 2019. URL <https://www.omroep gelderland.nl/nieuws/2428062/Evacuatie-Rivierengebied-1995-Omroep-Gelderland-verzamelt-herinneringen>. Last accessed 23 April 2020.
- [29] OpenPIV group. *OpenPIV Documentation*.
- [30] Landau H., Chen X., Klose S., Leandro R., and Vollath U. Trimble’s rtk and dgps solutions in comparison with precise point positioning. *Sideris M.G. (eds) Observing our Changing Earth*, 133:709 – 718, 2009. doi: DOI:/10.1007/978-3-540-85426-5_81.
- [31] Abas I. Remote river rating in zambia. a case study in the luangwa river basin. Master’s thesis, TU Delft, 2018.
- [32] Fujita I. and Komura S. Application of video image analysis for measurements of river-surface flows. *Proc. of Hydraulic Engineering*, 38:733–738 (in Japanese), 1994.
- [33] Fujita I. and Komura S. Application of video image analysis for measurement of river-surface flows. *Hydraulic Enigneering*, 38:733 – 738, 1994.
- [34] Fujita I. and Kunita Y. Application of aerial Ispiv to the 2002 flood of the yodo river using a helicopter mounted high density video camera. *Journal of Hydro-environment Research*, 5(4):323–331, 2011. doi: DOI:10.1016/j.jher.2011.05.003.
- [35] Fujita I., Muste M., , and Kruger A. Large-scale particle image velocimetry for flow analysis in hydraulic engineering applications. *Journal of Hydraulic Research*, 36:3:397–414, 1998. doi: [doi:10.1080/00221689809498626](https://doi.org/10.1080/00221689809498626).

- [36] Teledyne RD Instruments. *RiverRay ADCP Intelligent River Discharge System*.
- [37] Adrian R. J. Multi-point optical measurements of simultaneous vectors in unsteady flow—a review. *International Journal of Heat and Fluid Flow*, 7:127 – 145, 1984. doi: [https://doi.org/10.1016/0142-727X\(86\)90062-7](https://doi.org/10.1016/0142-727X(86)90062-7).
- [38] Adrian R. J. Techniques for experimental fluid mechanics. *Journal of Geophysical Research Atmospheres*, 23:261–304, 1991. doi: <https://doi.org/10.1146/annurev.fl.23.010191.001401>.
- [39] Arcement G. J. and Schneider V. R. *Guide for Selecting Manning's Roughness Coefficients for Natural Channels and Flood Plains*.
- [40] Huizinga R. J. Bathymetric and velocimetric surveys at highway bridges crossing the missouri river near kansas city. *U.S. Geological Survey Scientific Investigations Report*, 3016–5061:93, 2016. doi: <http://dx.doi.org/10.3133/sir20165061>.
- [41] Le Coz J., Hauet A., Pierrefeu G., Dramais G., and Camenena B. Performance of image-based velocimetry (Ispiv) applied to flash-flood discharge measurements in mediterranean rivers. *Journal of Hydrology*, 394:42–52, 2010. doi: <https://doi.org/10.1016/j.jhydrol.2010.05.049>.
- [42] Legleiter C. J. Remote measurement of river morphology via fusion of lidar topography and spectrally based bathymetry. *Earth Surface Processes and Landforms*, 37(5):499–518, 2012.
- [43] Legleiter C. J., Kinzel P. J., and Overstreet B. T. Evaluating the potential for remote bathymetric mapping of a turbid, sand-bed river: 1. field spectroscopy and radiative transfer modeling. *Water Resources Research*, 47(9), 2011.
- [44] Legleiter C. J., Kinzel P. J., and Nelson J. M. Remote measurement of river discharge using thermal particle image velocimetry (piv) and various sources of bathymetric information. *Journal of Hydrology*, 554:490–506, 2017.
- [45] Taylor Z. J., Gurka R., Kopp G. A., and Liberzon A. Long-duration time-resolved piv to study unsteady aerodynamics. *IEEE Transactions on Instrumentation and Measurement*, 59(12):3262–3269, 2010.
- [46] Kastner K., Hoitink A. J. F., P. J. J. F. Torfs, Vermeulen B., Ningsih N. S., and Pramulya M. Prerequisites for accurate monitoring of river discharge based on fixed-location velocity measurements. *WaterResources Research*, 54:1058–1076., 2018. doi: 10.1002/2017WR020990.
- [47] Kawanisi K., Kaneko A., Nigo S., Soltanias M., and Maghrebi M. F. New acoustic system for continuous measurement of river discharge and water temperature. *Water Science and Engineering*, 3:47–55, 2010. doi: 10.3882/j.issn.1674-2370.2010.01.005.
- [48] Marks K. and Bates P. Integration of high-resolution topographic data with floodplain flow models. *Hydrological Processes*, 14(11-12):2109–2122, 2000.
- [49] Softwel ltd. *SW Maps user's manual*.
- [50] Abu-Zeid M. and Shiklomanov I. A. Water resources as a challenge of the twenty-first century. *World Meteorological Organization*, No.959:1314–1324, 2003. doi: ISBN:92-63-10969-9.
- [51] Jodeau M., Hauet A., Le Coz J., Bercovitz Y., and Lebert F. Laboratory and field Ispiv measurements of flow velocities using fudaa-Ispiv, a free user-friendly software. *HydroSenSoft Conference Paper*, 2017.
- [52] Muste M., Fujita I., and Hauet A. Large-scale particle image velocimetry for measurements in riverine environments. *Water resources research*, 44, 2008.
- [53] Muste M., Fujita I., and Hauet A. Large-scale particle image velocimetry for measurements in riverine environments. *Water resources research*, VOL. 44, 2008. doi: doi:10.1029/2008WR006950,2008.

- [54] Ninnis R. M., Emery W., Emery M., and Collins M. Automated extraction of pack ice motion from advanced very high resolution radiometer imagery. *Journal of Geophysical Research Atmospheres*, C9:10725–10734, 1986. doi: 10.1029/JC091iC09p10725.
- [55] Raffel M., Willert C. E., Scarano F., Kähler C. J., Wereley S. T., and Kompenhans J. *Particle Image Velocimetry*. Springer, Berlin, Heidelberg, 1998. ISBN 978-3-662-03637-2(online).
- [56] Van Dyke M. *An Album of Fluid Motion*. The Parabolic Press, 1982. ISBN 0-915760-02-9.
- [57] Open Drone Map, 2020. URL <https://www.opendronemap.org/>. Last accessed 08 April 2020.
- [58] Collins M.J. and Emery W. A computational method for estimating sea ice motion in sequential seosat synthetic aperture radar imagery by matched filtering. *Journal of Geophysical Research Atmospheres*, C8:9241–9251, 1988. doi: 10.1029/JC093iC08p09241.
- [59] Lane S. N. Hydraulic modelling in hydrology and geomorphology: a review of high resolution approaches. *Hydrological Processes*, 12(8):1131–1150, 1998.
- [60] Lane S. N., James T. D., and Crowell M. D. Application of digital photogrammetry to complex topography for geomorphological research. *The Photogrammetric Record*, 16(95):793–821, 2000.
- [61] High Level Panel on Water. An agenda for water action, an open letter from the high level panel on water. March 14, 2018.
- [62] Stephen Mather Open Drone Map, 2020. URL <https://www.opendronemap.org/tag/camera-calibration/>. Last accessed 19 April 2020.
- [63] Buchhave P. Experimental thermal and fluid science particle image velocimetry—status and trends. *Experimental Thermal and Fluid Science*, 5:586–604, 1992. doi: [https://doi.org/10.1016/0894-1777\(92\)90016-X](https://doi.org/10.1016/0894-1777(92)90016-X).
- [64] Dobriyal P., Badola R., and Tuboi C. A review of methods for monitoring streamflow for sustainable water resource management. *Applied Water Science*, 7:2617–2628, 2017. doi: <https://doi.org/10.1007/s13201-016-0488-y>.
- [65] Ran Q., Li W., Liao Q., Tang H., and Wang M. Application of an automated Ispiv system in a mountainous stream for continuous flood flow measurements. *Hydrological processes*, 30:3014–3029, 2019. doi: 10.1002/hyp.10836.
- [66] Herschy R. The stage-discharge relation. *Flow Measurement and Instrumentation*, 4(1):11–15, 1993.
- [67] Herschy R. The stage-discharge relation. *Flow Measurement and Instrumentation*, 4:11 – 15, 1993.
- [68] James M. R. and Robson S. Mitigating systematic error in topographic models derived from uav and ground-based image networks. *Earth Surface Processes and Landforms*, 39:1413–1420, 2014. doi: DOI:10.1002/esp.3609.
- [69] Le Boursicaud R., Pénard L., Hauet A., Thollet F., and Le Coz J. Gauging extreme floods on youtube: application of Ispiv to home movies for the post-event determination of stream discharges. *Hydrological processes*, 30:90–105, 2016. doi: 10.1002/hyp.10532.
- [70] Cosentino R.J., Diggle D.W., Haag M.U., Hegarty C.J., Milbert D., and Nagle J. Differential gps. *Understanding GPS, Principles and Application*, 2nd ed:379 – 454, 2005.
- [71] Fortunato S., Sasso D., Pizarro A., Vuono P., and Manfreda S. Accuracy of large-scale particle image velocimetry (Ispiv) techniques applied on low seeding density flows. *Geophysical Research Abstracts*, 21, 2019.

- [72] Jimenez-Gonzalez S., Mayerle R., and Egozcue J. J. On the accuracy of acoustic doppler current profilers for in-situ measurements. a proposed approach and estimations for measurements in tidal channels. *Proceedings of the IEEE/OES Seventh Working Conference on Current Measurement Technology*, pages 197 – 201, 2003. doi: DOI:10.1109/CCM.2003.1194311.
- [73] Mueller D. S. and Wagner C. R. Measuring discharge with acoustic doppler current profilers from a moving boat. In U.S. Geological Survey, editor, *Techniques and Methods 3A–22*, chapter 22 of book 3, page 72. USGS, 2009.
- [74] Pearce S., Maddock I., Corbett M., and Everard N. A comparison of using unmanned aerial vehicles (uav) and mobile video for establishing surface flow velocity measurements using the lspiv method on the river arrow, warwickshire. *Geophysical Research Abstracts*, 20, 2018.
- [75] Schurer S. Thesis sschurer. <https://github.com/StenSchurer/ThesisSSchurer>, 2020.
- [76] Song S., Schmalz B., and Fohrer N. Improved structure of vertical flow velocity distribution in natural rivers based on mean vertical profile velocity and relative water depth. *Hydrology research*, 49:872 – 892, 2018.
- [77] Jin T. and Liao Q. Flow measurement and instrumentation application of large scale piv in river surface turbulence measurements and water depth estimation. *Flow Measurement and Instrumentation*, 67:142–152, 2019. doi: <https://doi.org/10.1016/j.flowmeasinst.2019.03.001>.
- [78] Von Kármán T. *Mechanical Similitude and Turbulence*. National Advisory Committee for Aeronautics, Washington, DC., 1931.
- [79] Vliet van der N. River-width determination by the use of optical remote sensing missions. Master's thesis, TU Delft, 2019.
- [80] Diggelen van F. and Enge P. The world's first gps mooc and worldwide laboratory using smart-phones. *Proceedings of the 28th International Technical Meeting of the Satellite Division of The Institute of Navigation (ION GNSS+ 2015)*, pages 361 – 369, 2015.
- [81] Emery W., Thomas A. C., Collins M., and Mackas L. An objective method for computing advective surface velocities from sequential infrared satellite images. *Journal of Geophysical Research Atmospheres*, C11:12865–12878, 1986. doi: DOI:10.1029/JC091iC11p12865.
- [82] Goodman J. W. *Introduction to Fourier Optics*. McGraw-Hill, 1968.
- [83] Herschy R. W. *Streamflow measurement*. CRC Press, 2002.
- [84] Lauterborn W. and Vogel A. Modern optical techniques in fluid mechanics. *Annual Review of Fluid Mechanics*, 16:223 – 44, 1984. doi: <https://doi.org/10.1146/annurev.fl.16.010184.001255>.
- [85] Lewis Q. W., Lindroth E. M., and Rhoads B. L. Integrating unmanned aerial systems and lspiv for rapid, cost-effective stream gauging. *Journal of Hydrology*, 560:230–246, 2018. doi: <https://doi.org/10.1016/j.jhydrol.2018.03.008>.
- [86] Li W., Liao Q., and Ran Q. Stereo-imaging lspiv (si-lspiv) for 3d water surface reconstruction and discharge measurement in mountain river flows. *Journal of Hydrology*, 578, 2019. doi: <https://doi.org/10.1016/j.jhydrol.2019.124099>.
- [87] Straatsma M. W. and Baptist M. J. Floodplain roughness parameterization using airborne laser scanning and spectral remote sensing. *Remote Sensing of Environment*, 112(3):1062–1080, 2008.
- [88] Thielicke W. and Stamhuis E. J. Pivlab – towards user-friendly, affordable and accurate digital particle image velocimetry in matlab. *Journal of Open Research Software*, 2, 2014. doi: DOI: <http://dx.doi.org/10.5334/jors.bl>.
- [89] Water Recourse Management Authority (WARMA), 2020. URL <http://www.warma.org.zm/catchments-zambia/luangwa-catchment-2/>. Last accessed 02 April 2020.

-
- [90] Xue Z., Charonko J.J., and Vlachos P.P. Signal-to-noise ratio, error and uncertainty of piv measurement. *Part of: PIV13; 10th International Symposium on Particle Image Velocimetry*, 2013.
- [91] Zhang Z., Wang X., Fan T., and Xu L. River surface target enhancement and background suppression for unseeded lspiv. *Flow Measurement and Instrumentation*, 30:99–111, 2013. doi: <https://doi.org/10.1016/j.flowmeasinst.2012.12.002>.



Surface Flow Velocity

This appendix contains photos, tables and figures complementary to the data provided in the chapters regarding Large-Scale Particle Image Velocimetry.

Figure A.1 and A.2 show the components and setup of the constructed Real Time Kinematic GPS. The container on the right-hand side in Figure A.1 contains the base, the other container contains the rover. Both containers include two SimpleRTK2B boards with a u-blox-ZED9P module, a Raspberry Pi Zero W, two GNSS antennas, an XBEE shield and a long range radio antenna. With this hardware, two complete RTK GPS sets can be constructed, one based on long range radio communication and one based on a 4G internet connection. The SimpleRTK2B board with the XBEE shield works with the radio module and is used during the fieldwork.

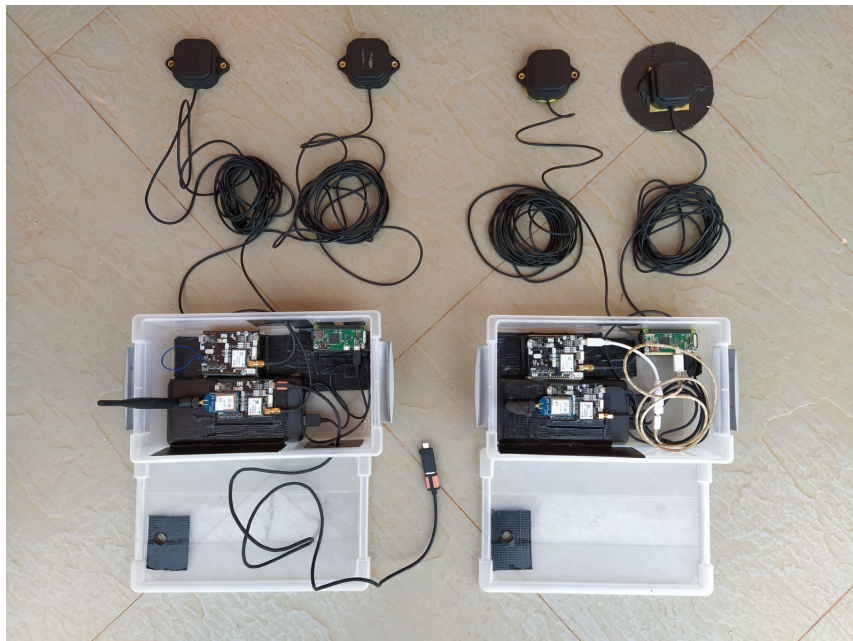


Figure A.1: Real Time Kinematic GPS set. Right: the Base, left: the rover..

Figure A.2 depicts the RTK GPS setup at the fieldwork site. The SimpleRTK2B board together with the radio module and a power-bank are connected to the tripod in order to create a clear line of sight with the rover. The GNSS antenna is mounted on top of a small pole and kept at the exact same location after activation of the base.



Figure A.2: Setup of the RTK base. Left the GNSS receiver and on the tripod the SimpleRTK2B board with radio module.

Figure A.3 shows the seeding of artificial tracers upstream of the research area just before the drone started recording the videos meant for LSPIV analysis. The three wooden canoes are used to distribute the tracers over the whole width of the river.



Figure A.3: Seeding coarse sawdust as artificial tracers in the Luangwa river.

Figure A.4 shows a current meter measurement done from a wooden canoe. The canoe is kept as steady as possible in the current while the flow velocity is measured and the location is mapped with RTK GPS. The current meter is placed just under the water surface in order to measure the surface flow velocity.



Figure A.4: Measuring the surface flow velocity with a current meter from a canoe.

The following pages contain all surface flow velocity vector fields produced by OpenPIV with different configurations. The exact description of the configurations is given at section 4.1.

Figure A.5 shows the surface flow velocity vector fields for different editing methods. In order of appearance: Original Stabilized (OS), Original Stabilized Grayscale (OSG), Original Stabilized Grayscale Gamma (OSGG) and Original Stabilized Grayscale Gamma Contrast (OSGGC).

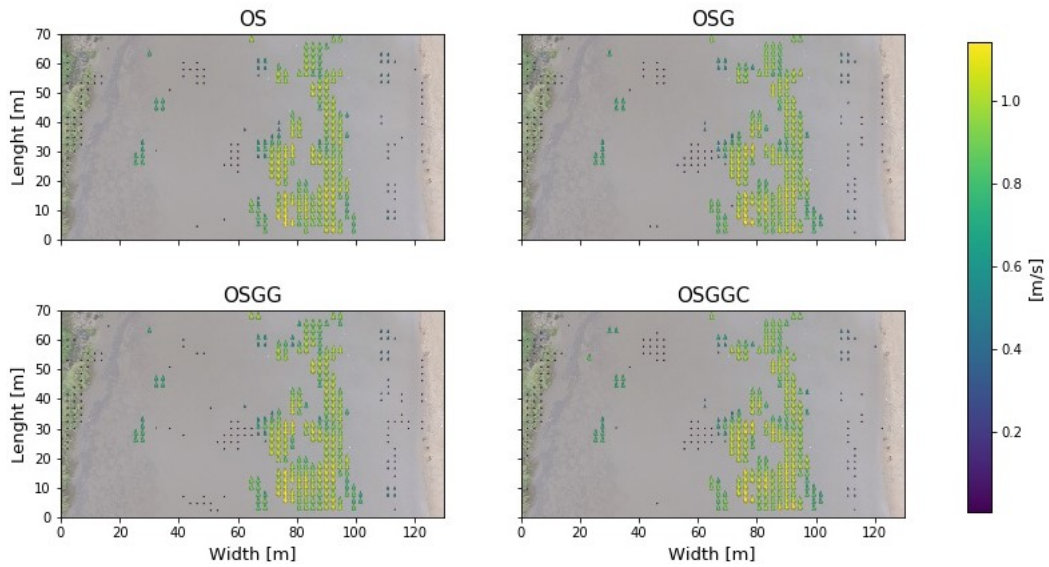


Figure A.5: Velocity vector fields for videos with a different editing method.

Figure A.6 shows all surface velocity vector fields for different video lengths, i.e. 5, 10, 15 and 20 seconds.

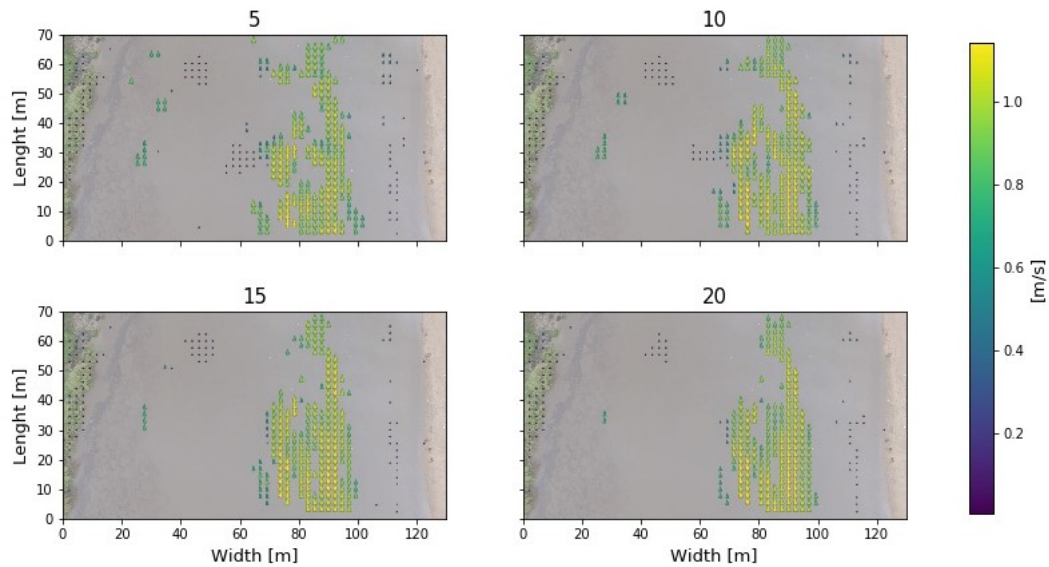


Figure A.6: Velocity vector fields for videos with a different Length.

Figure A.7 shows the surface flow velocity vector field for different signal to noise determination methods. Peak to Peak and Peak to Mean respectively.

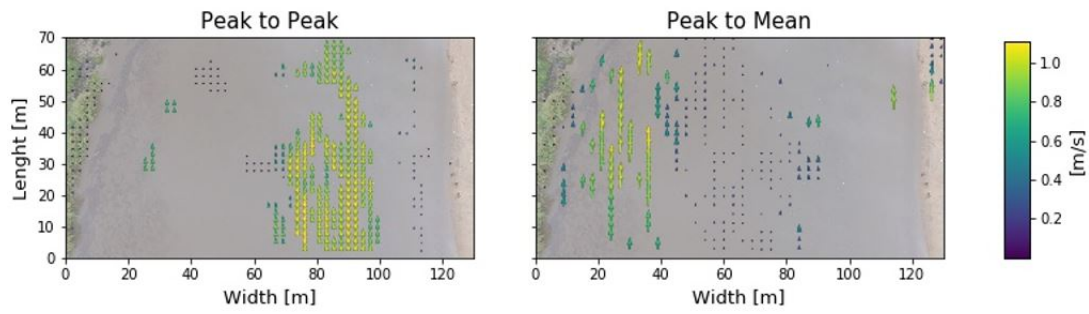


Figure A.7: Velocity vector fields based on different signal to noise ratio determination methods.

Figure A.8 shows surface flow velocity vector fields produced with OpenPIV that used a different the signal to noise threshold. A threshold of 1 means all displacements are accepted and converted to velocities. The different threshold values are: 1.0, 1.3, 1.5, 1.8, and 2.0.

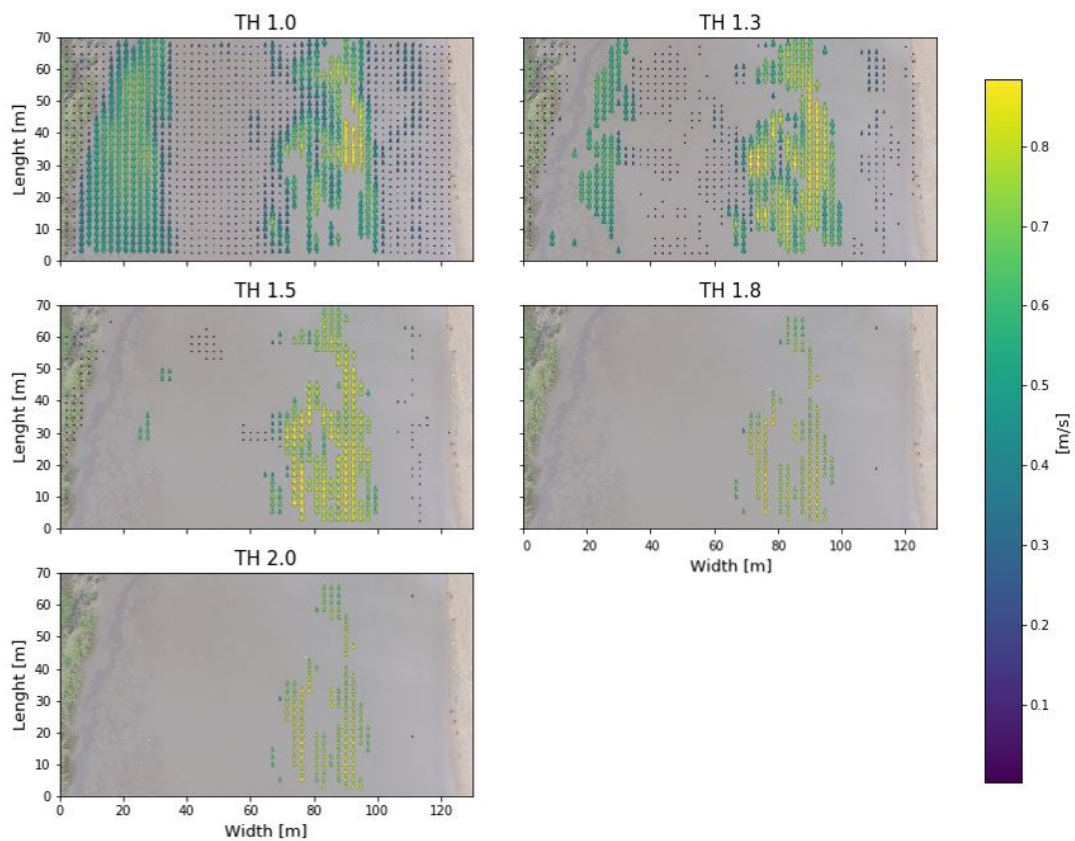


Figure A.8: Velocity vector fields based on different signal to noise thresholds.

Figure A.9 shows surface flow velocity vector fields produced by OpenPIV for different window sizes and overlap values. In order of appearance: window size of 50 x 50 pixels with 25 pixels overlap, window size of 100 x 100 pixels with 50 pixels overlap, window size of 100 x 100 pixels with 75 pixels overlap and finally a window size of 200 x 200 pixels with 100 pixels overlap.

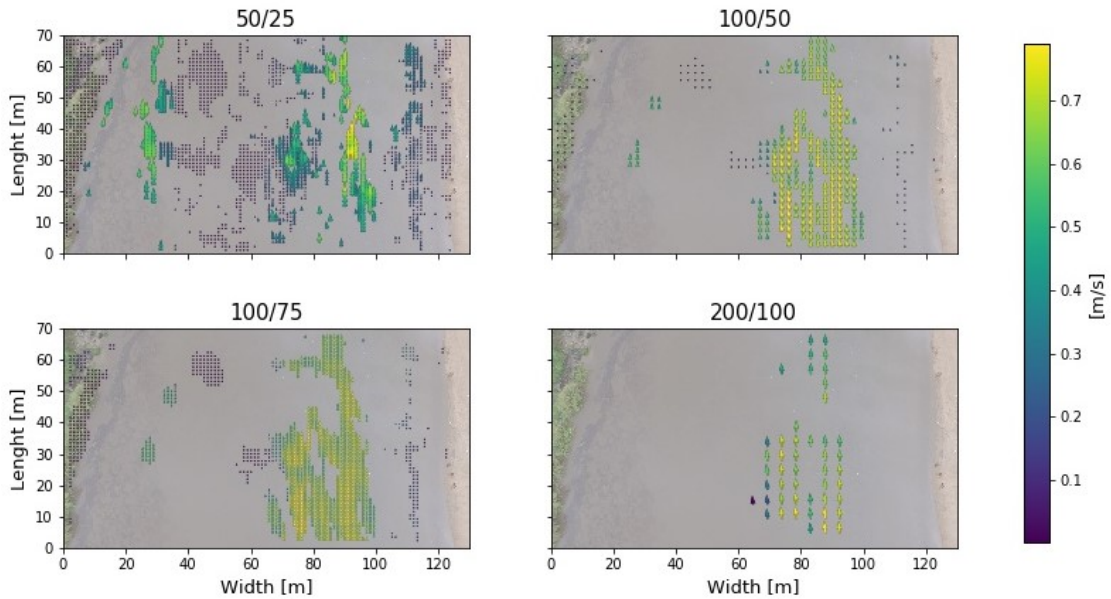


Figure A.9: Velocity vector fields for different window sizes and overlap values specified in OpenPIV.

Figure A.10 shows the surface flow velocity vector fields for three videos recorded under different circumstances. That are: just after a precipitation event, before the precipitation event (normal flow conditions) and while artificial tracers are seeded.

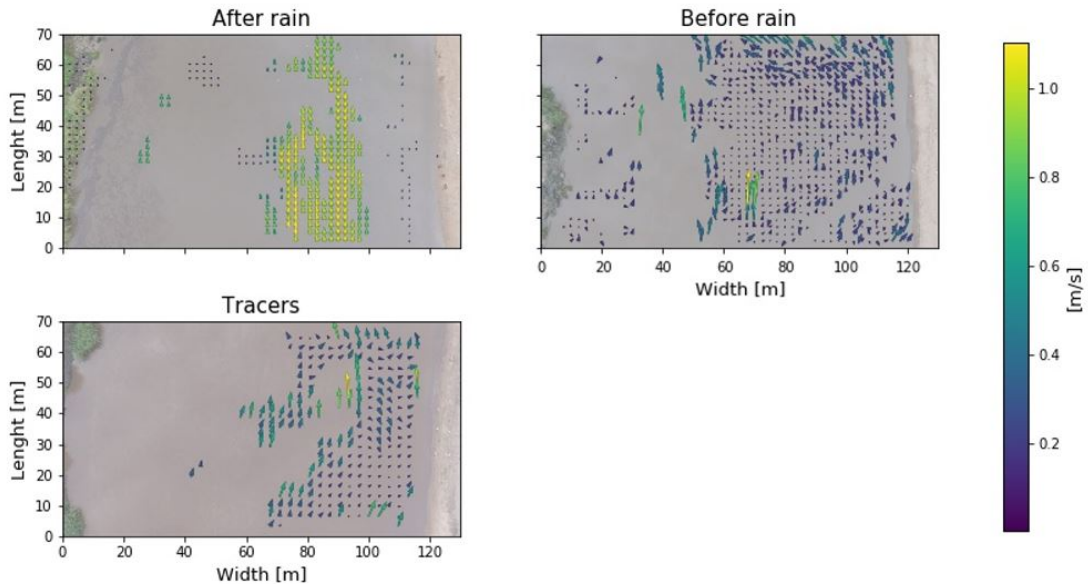


Figure A.10: Velocity vector fields for videos recorded under different circumstances.

The following series of figures show the performance of the different LSPIV configurations compared to the current meter measurements. The plots visualize the Mean Average Deviation between LSPIV and the current meter by plotten them on the Y and X axis respectively. All velocities include an error bar representing one standard deviation and a number defining the amount of computed velocities the average is based on. Through the velocities a regression line is plotted represented by the red line. For a perfect accordance between both measurement techniques the regression line should follow the 1:1 (grey dotted) line. The configurations are identical to the configurations of the vector fields shown above.

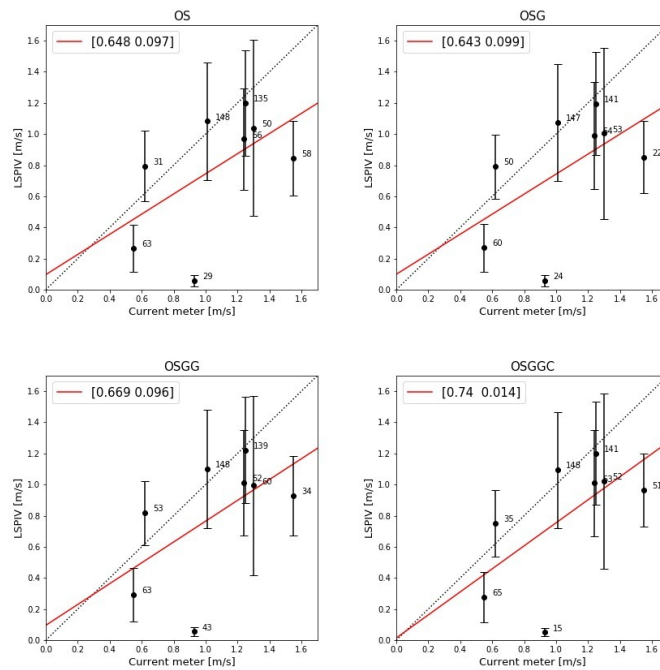


Figure A.11: LSPIV plotted against current meter measurements with error bars of one standard deviation. The results originate from videos edited with different methods.

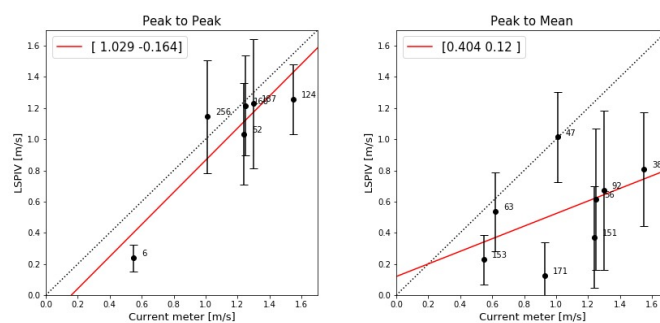


Figure A.12: LSPIV plotted against current meter measurements with error bars of one standard deviation. The results are based on an OpenPIV configuration with different signal to noise determination methods.

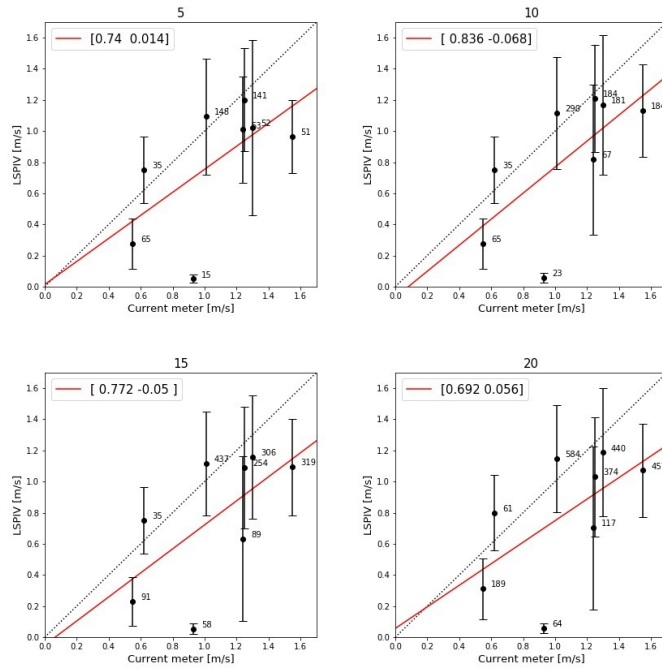


Figure A.13: LSPIV plotted against current meter measurements with error bars of one standard deviation. The results are based on videos with different length.

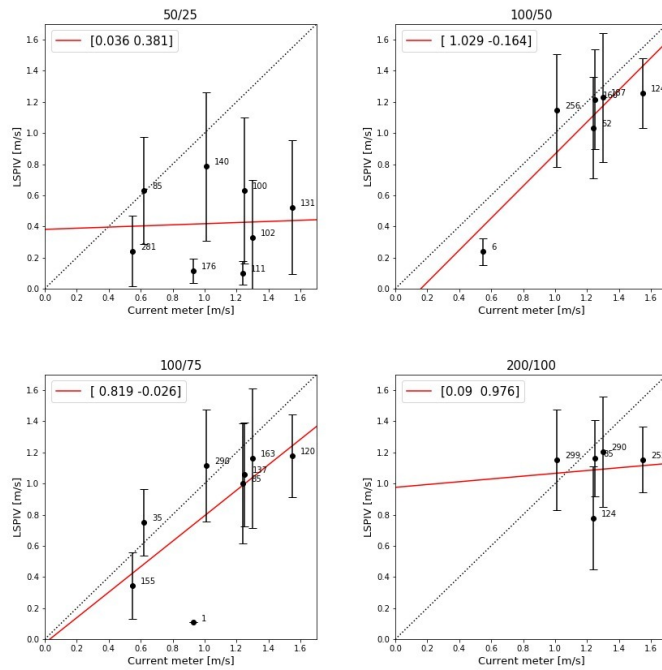


Figure A.14: LSPIV plotted against current meter measurements with error bars of one standard deviation. The results are based on an OpenPIV configuration with different window sizes and overlap values.

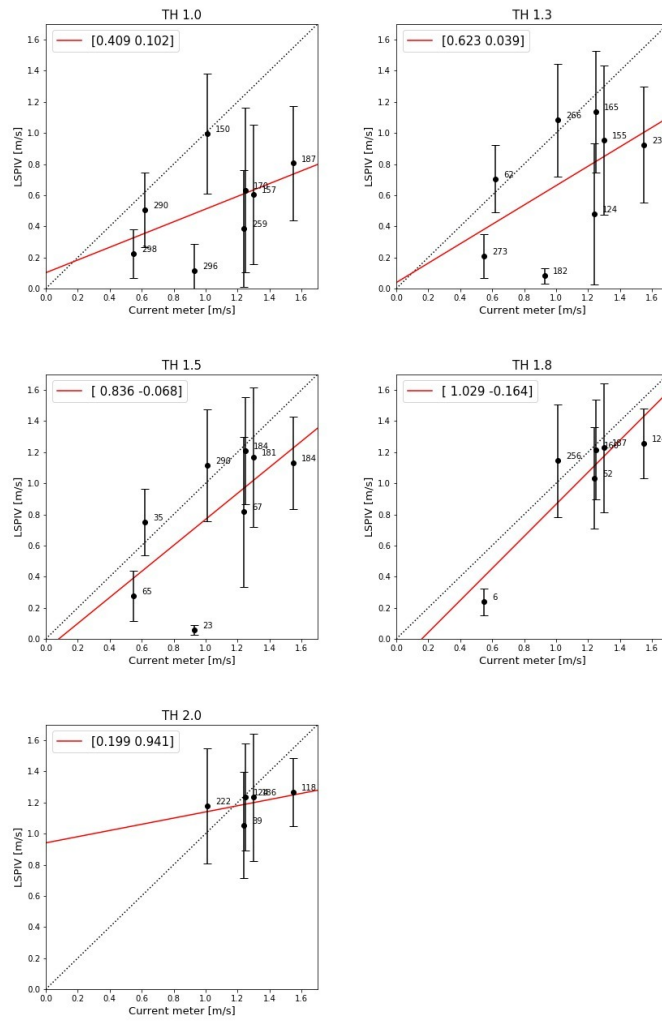


Figure A.15: LSPIV plotted against current meter measurements with error bars of one standard deviation. The results are based on an OpenPIV configuration with different thresholds set for the signal to noise ratio.

The following series of figures visualize the horizontal velocity vector (V_x) and vertical velocity vector (V_y) displacement values that together determine the direction and velocity (the velocity vector) within each window. Where V_y is the downstream direction and V_x the width of the river. The configurations are identical to the configurations of the vector fields and MAD plots shown above.

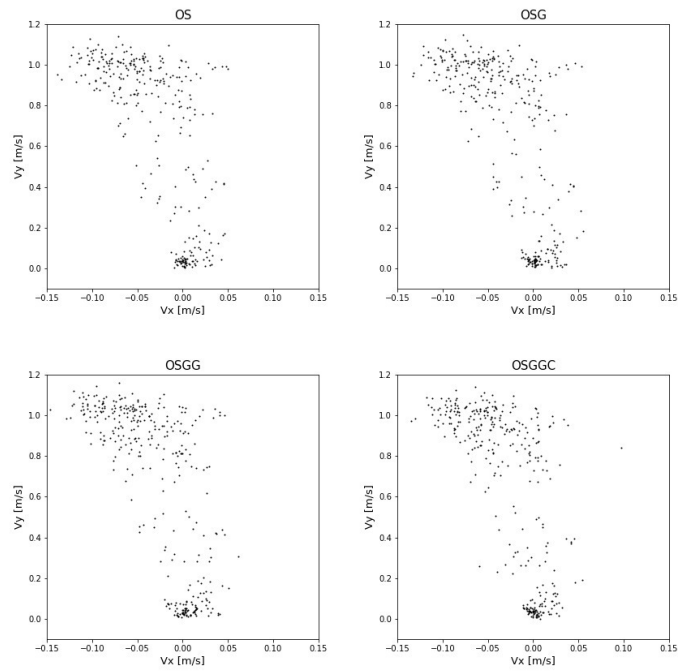


Figure A.16: Velocity vector components V_x (horizontal) and V_y (vertical) compose together the velocity vector computed by OpenPIV. The results originate from videos edited with different methods.

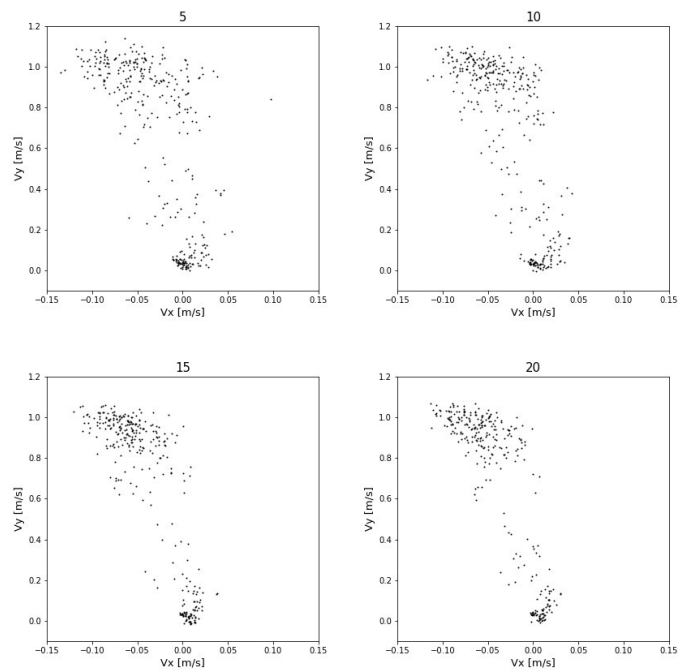


Figure A.17: Velocity vector components V_x (horizontal) and V_y (vertical) compose together the velocity vector computed by OpenPIV. The results are based on videos with different length.

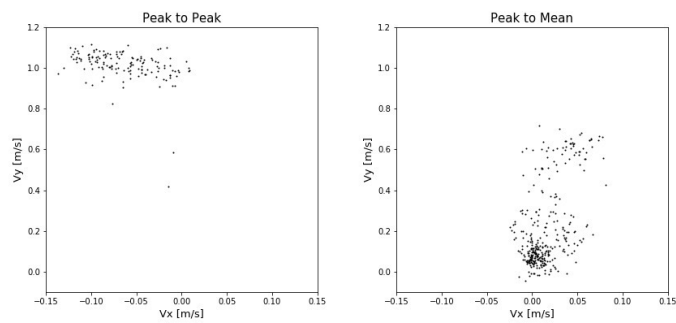


Figure A.18: Velocity vector components V_x (horizontal) and V_y (vertical) compose together the velocity vector computed by OpenPIV. The results are based on an OpenPIV configuration with different signal to noise determination methods

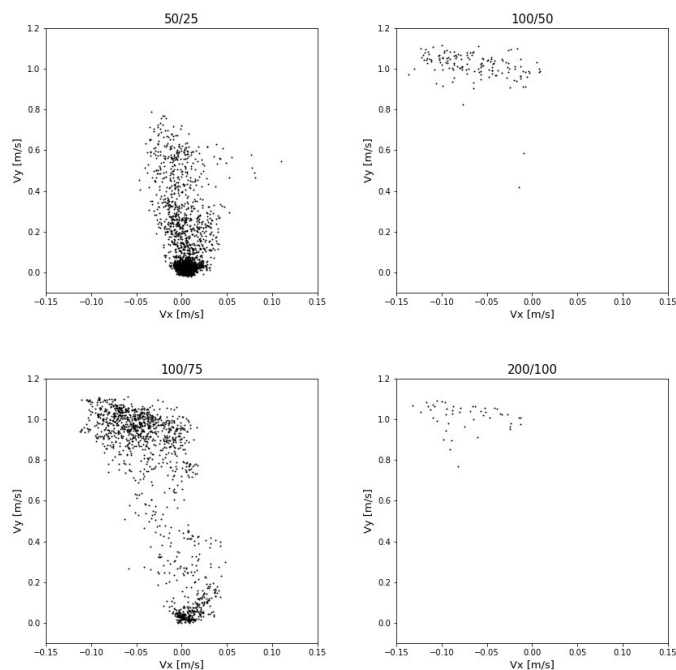


Figure A.19: Velocity vector components V_x (horizontal) and V_y (vertical) compose together the velocity vector computed by OpenPIV. The results are based on an OpenPIV configuration with different window sizes and overlap values.

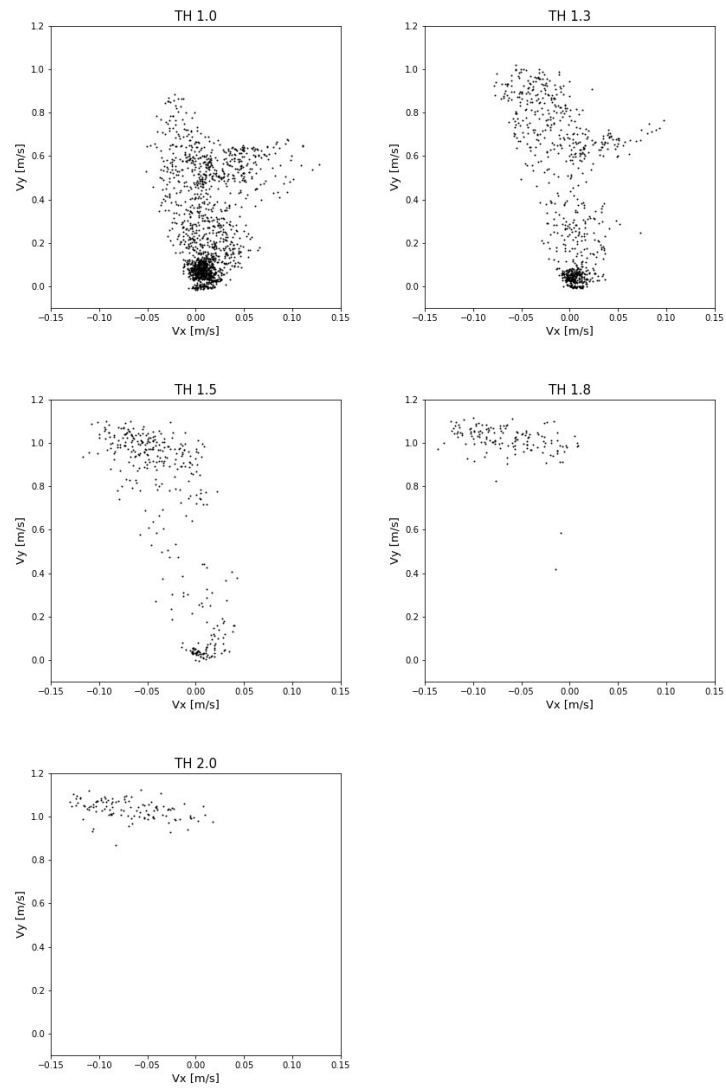


Figure A.20: Velocity vector components V_x (horizontal) and V_y (vertical) compose together the velocity vector computed by OpenPIV. The results are based on an OpenPIV configuration with different thresholds set for the signal to noise ratio.

B

Bathymetric chart

This appendix contains photos, tables and figures complementary to the data provided in the chapters regarding the bathymetric chart.

Figure B.1 shows the bathymetric data collection setup with the ADCP tied to the wooden canoe of a local boatman. On top of the sonar an RTK GNSS receiver is mounted which is, via a SimpleRTK2B board, connected to a smartphone logging the location measurements with a one second time interval. The ADCP is connected to a laptop running WinriverII which stores the depth measurements.

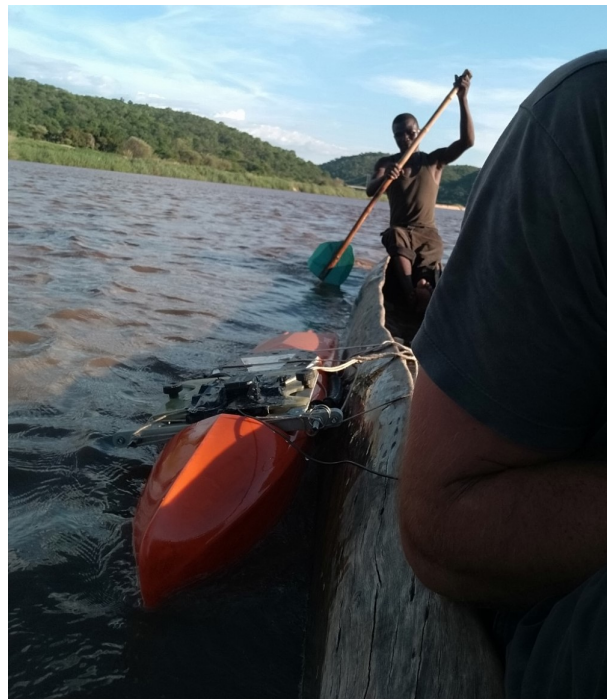


Figure B.1: The ADCP connected to the canoe with the GNSS receiver mounted on top of the sonar.

Figure B.2 shows the cart made to pull the RTK GPS rover over the floodplain while measuring continuously. This cart is also towed along the waterline in order to determine the hydraulic slope (Figure B.3). Obviously, the height of the cart and the container are subtracted from the height measurements.



Figure B.2: Cart with the RTK GPS rover on top in order to measure the floodplain and exact waterline.

Figure B.3 shows the waterline over 439 metres mapped with the cart depicted in Figure B.2. The plot consists of 898 measurement points with a standard deviation of 0.018 metres. The linear fit through the data represents the waterline with a slope of 0.0002298.

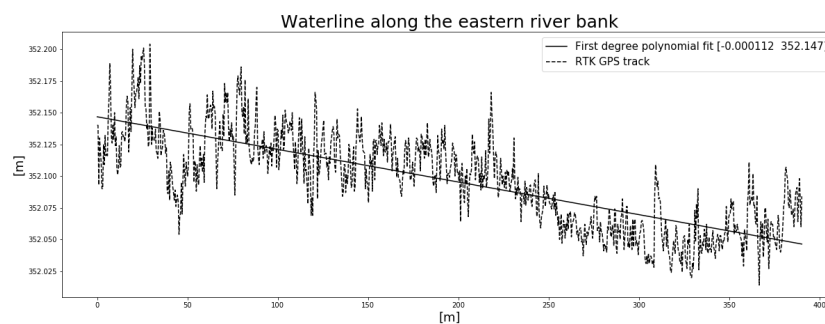


Figure B.3: The slope of the river is 0.0002298, measured over 439 metres with 898 measurements.

Figure B.4 provides the height coordinates of the WebODM floodplain point clouds for different calibration models sampled on the closest distance to the coordinates of the waterline track (sampled with the Rasterio package in python). The Figure clearly shows a bowling effect in the perspective point cloud and overcompensation of the effect by the Brown-Conrady calibration models.

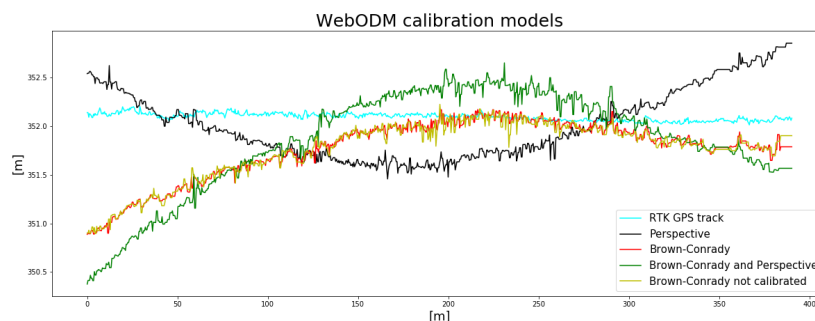


Figure B.4: The WebODM default model (Perspective) creates a concave shape instead of the desired slope of the RTK GPS track. The Brown Conrady model overcompensates for this deformation and creates a convex shape. Combinations between Perspective and Brown Conrady also do not yield a satisfactory result.

Figure B.5 shows the polynomials fitted through the height coordinates depicted in Figure B.4. The polynomials are fit in order to assess the best performing model compared to the RTK GPS track, the results are shown in Table B.1.

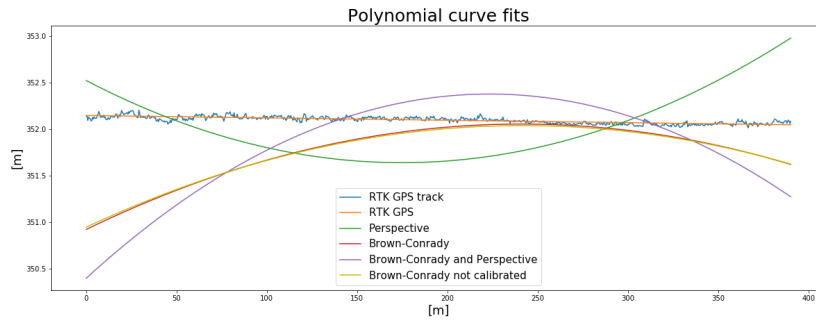


Figure B.5: Polynomial curves fit through the point cloud waterlines of different camera calibration models. The polynomials are used to determine the error for each section along the latitudinal axis.

Table B.1 displays the absolute average deviation of the polynomials depicted in Figure B.5 from the RTK GPS track polynomial also shown in the figure.

Method	Absolute error
RTK GPS track	0.01832
Perspective	0.32580
Brown Conrady	0.33122
Brown Conrady and Perspective	0.42321
Brown Conrady non calibrated	0.33687

Table B.1: Absolute errors of the polynominal fitted through the RTK GPS track and the polynominals fitted through the different WebODM calibration models. Please note that the absolute error of the RTK GPS track is the error between the measured line and the polynominal.

The adaptation length of the river at a discharge of 191 m³/s is calculated as follows:

$$L = \frac{h_e^3 - h_c^3}{h_e^2 i_b} \quad (\text{B.1})$$

With equilibrium depth:

$$h_e = \left(\frac{Q|Q|}{C^2 B^2 i_b} \right)^{1/3} \quad (\text{B.2})$$

And critical depth:

$$h_c = \left(\frac{Q^2}{g B_c^3} \right)^{1/3} \quad (\text{B.3})$$

The half length is calculated using the following equation:

$$L_{1/2} = \frac{0.24 h_e}{i_b} \left(\frac{h_0}{h_e} \right)^{4/3} \quad (\text{B.4})$$

With:

$$Q = 191 \text{ m}^3/\text{s}$$

$$C = 40 \text{ m}^{1/2}/\text{s}$$

$$B = 120 \text{ m}$$

$$i_b = 0.000229809$$

$$h_0 = 2 \text{ m}$$

Figure B.6, B.7 and B.8 show the complete creation process of the bathymetric chart.

In Figure B.6 the river cross sections made with the ADCP and RTK GPS combination (see Figure B.1) are volumized with a linear interpolation technique. Subsequently the waterline track (see Figure B.3) and the bank measurements are added and the whole point cloud is volumized again.

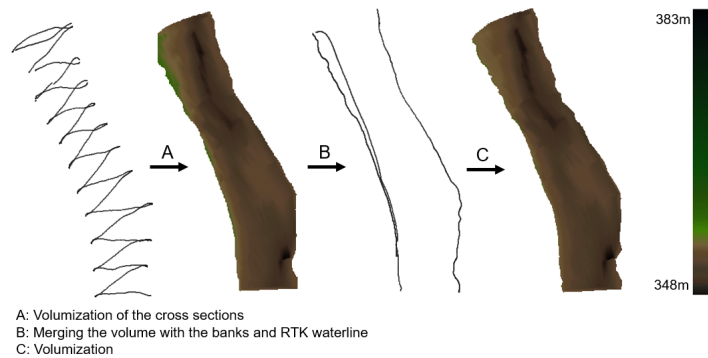


Figure B.6: The point cloud made with the ADCP and RTK GPS is transformed to a volumized point cloud in CloudCompare.

Figure B.7 shows the 'straightened' floodplain which is combined with the wet river point cloud and volumized in order to create a seamless bathymetric chart. The small tributary in the north-east corner is cut out in order prevent outflow of water while running the discharge model.

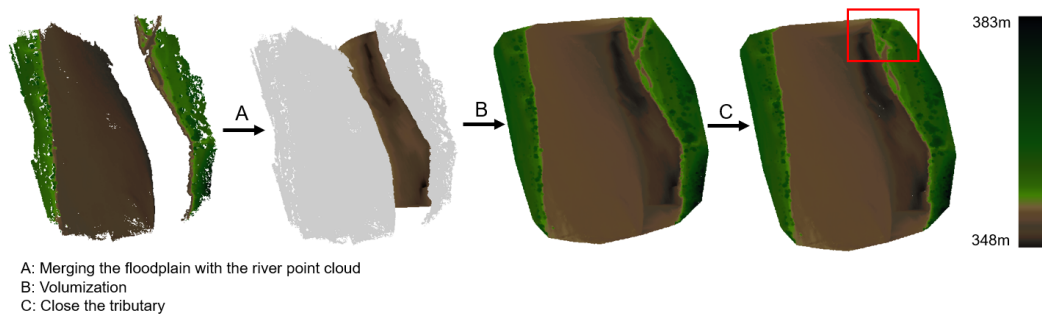


Figure B.7: The floodplain point cloud is merged with the river point cloud.

Figure B.8 depicts the last processing steps of the bathymetric chart. The chart is cut perpendicular to the flow direction at both the up- and downstream boundaries. With a python script there are extension point clouds made (see Github repository [75]) that are merged with the centre bathymetric chart and finally volumized to create the final bed level consisting of 4.7×10^6 points.

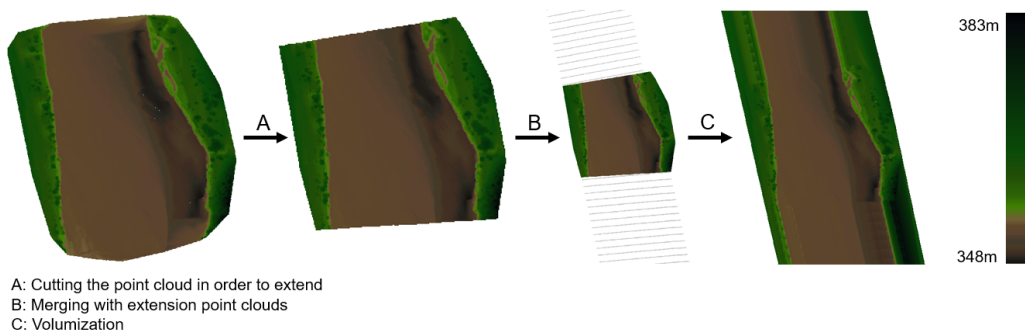


Figure B.8: A: The point cloud is cut at the up- and downstream boundaries, perpendicular to the direction of flow. B: the extension point clouds stretch approximately 4km to the north and south and are merged with the centre part point cloud. C: the point cloud is volumized.

C

Discharge model

This appendix contains photos, tables and figures complementary to the data provided in the chapters regarding the discharge model.

Figure C.1 shows a typical output of the Winriver software based on ADCP measurements over a cross section. The black line represents the river bottom and the colors represent flow velocity.

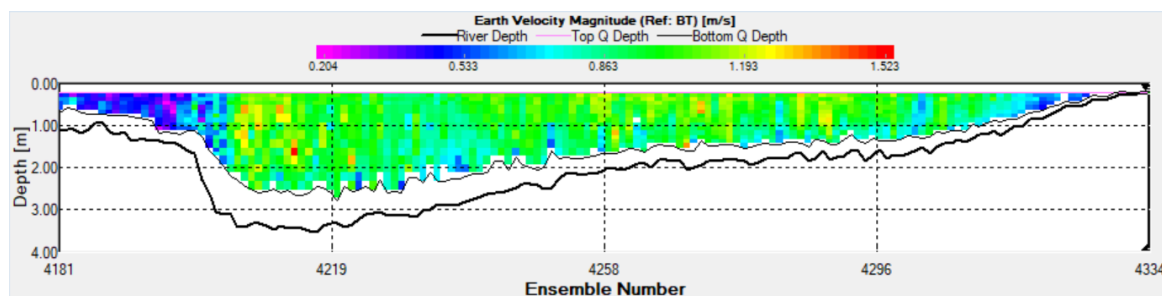


Figure C.1: Cross section as depicted by the Winriver II software.

Figure C.2 shows the different grids used in the discharge model for the simulation of 66 different discharges ranging from $5 \text{ m}^3/\text{s}$ to $3000 \text{ m}^3/\text{s}$. Different grid sizes are used to speed up the processing, i.e. the river is kept within the fine grid cell boundaries while the grids representing the dry floodplain and river banks are kept as coarse as possible. When the river hits the outer banks at approximately $660 \text{ m}^3/\text{s}$, grid E is used since the fine grid cells are introduced in order to create a width-discharge relationship.

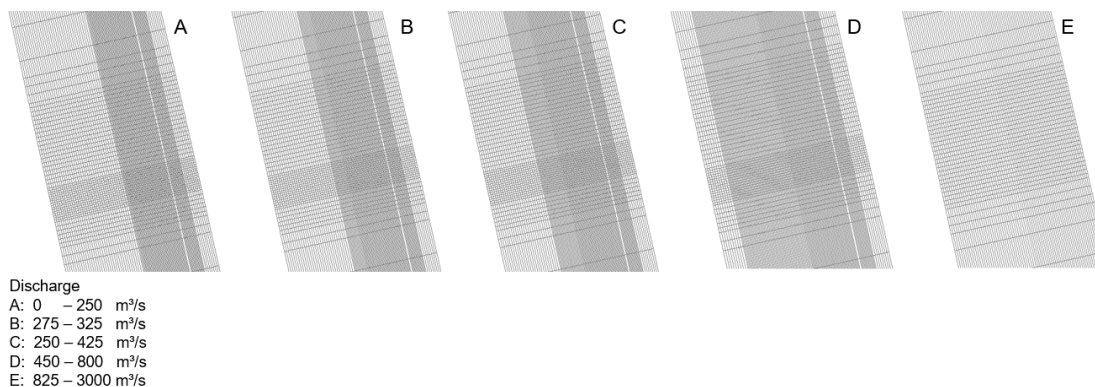


Figure C.2: Delft3D curvilinear grids for different discharges.

Figure C.3 shows stage-discharge relationships determined with the same set of rating points but based on different amounts of data. The cyan line represents the stage-discharge relationship based on 66 rating points as established in this research. The three other relationships are based on only 16, 11 and 6 of these 66 rating points respectively. Striking is the little difference between the relationships.

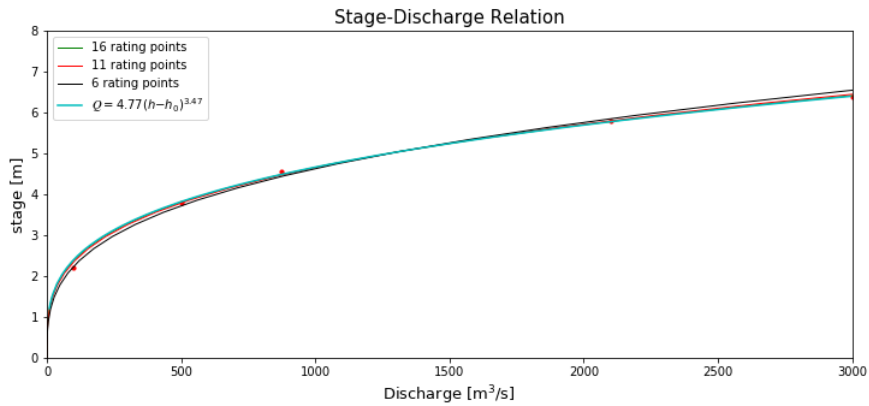


Figure C.3: The cyan line shows the stage-discharge relationships established over 66 rating points as determined in this research. The three other relationships are established over 16, 11 and 6 of these 66 rating points respectively.

Figure C.4 shows the three observation cross sections of the bathymetric chart used in the discharge model.

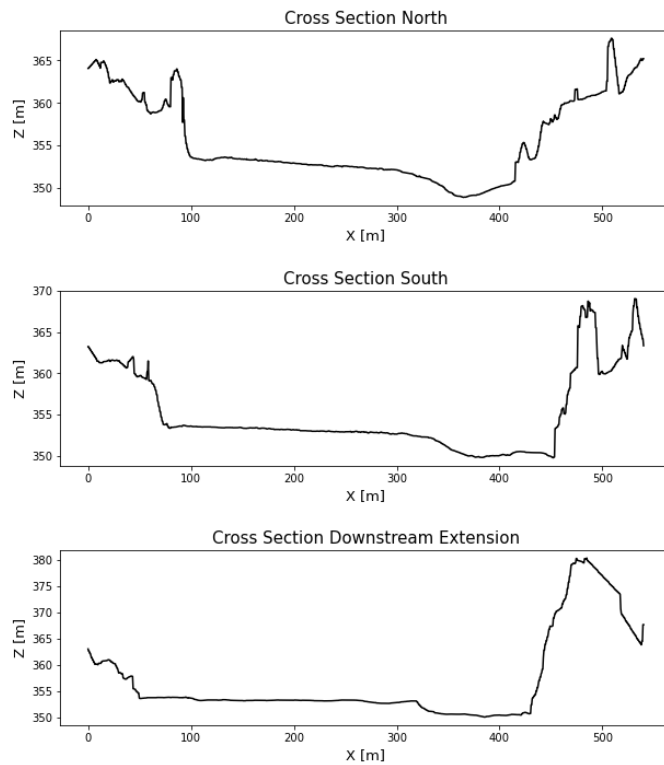


Figure C.4: Observation cross sections of the bathymetric chart.

Figure C.5 shows the vertical velocity profiles for the ten (measurement 5 and 6 are in the same grid cell) surface flow velocity observation points in the discharge model at the calibration discharge of $191 \text{ m}^3/\text{s}$ with a Manning coefficient of $0.014 \text{ s/m}^{1/3}$. The plots also show the surface flow velocity on which the MAD scores are based in Table 4.7

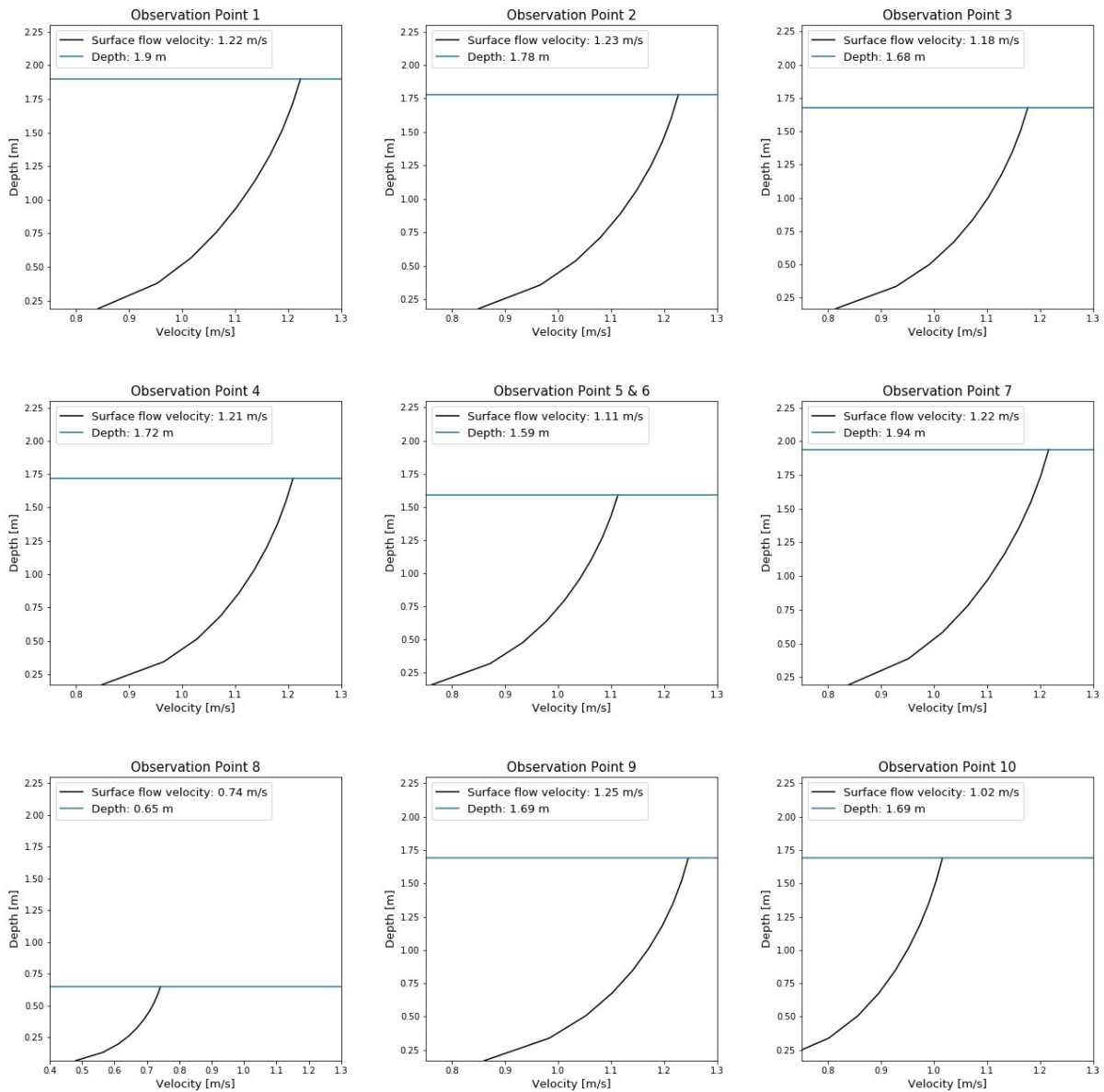


Figure C.5: Vertical velocity profiles at all ten velocity observation points in the Delft3D discharge model for a discharge of $191 \text{ m}^3/\text{s}$ with $n = 0.014 \text{ s/m}^{1/3}$. The plots also indicate the surface flow velocity and the depth.